Title

Controlling Static and Dynamic Multiferroic Effects with Nanoscale Structure

Permalink

Author

Karaba, Christopher Ty

Publication Date

2024

UNIVERSITY OF CALIFORNIA

Los Angeles

Controlling Static and Dynamic Multiferroic Effects with Nanoscale Structure

A dissertation submitted in partial satisfaction of the requirements for the degree Doctor of

Philosophy in Chemistry

by

Christopher Ty Karaba

ABSTRACT OF THE DISSERTATION

Controlling Static and Dynamic Multiferroic Effects with Nanoscale Structure

by

Christopher Ty Karaba

Doctor of Philosophy in Chemistry

University of California, Los Angeles, 2024

Professor Sarah H. Tolbert, Chair

This thesis explores magnetization dynamics in materials to help design future low-power electromagnetic devices. In this thesis, we explore materials for multiferroic composites that can couple electricity and magnetism through voltage, rather than current, allowing for the possibility of low power control of magnetism. We study both thin film systems and explore the effect of nanostructure on strain-mediated composites, which utilize a ferroelectric material that exhibits a strain response to an applied voltage, coupled to a magnetostrictive material, which changes magnetization in response to the strain produced by the ferroelectric.

In the first part of the thesis, yttrium iron garnet (YIG) is studied as a model system for low loss magnetic materials – a necessary requirement for high-frequency multiferroic devices. YIG is an ideal magnetic material for high-frequency devices, as it exhibits narrow magnetic resonances, but pure YIG has low magnetostriction. Using sol-gel chemistry, we were able to survey a range of cerium- and ruthenium-doped YIG compositions, which have both been shown to increase YIG's magnetostriction to useful levels in bulk crystals. Homogeneously doped

materials were synthesized and characterized, but the polycrystalline nature of the films led to significant magnetic losses at high frequency.

In the second part of the thesis, we explore three-dimensionally coupled porous multiferroic composites. These composites were synthesized by first using block-copolymer templating to create a nanoporous magnetostrictive framework. Atomic layer deposition (ALD) was then used to partially coat the inner surface of the pores with a thin layer of ferroelectric material, the thickness of which could be varied to change the extent of residual porosity. We found that composites with larger residual porosities exhibited a larger magnetoelectric coupling, due to the mechanical flexibility of the pores, which enabled larger strains. We first studied ferroelectric lead zirconate titanate (PZT) in magnetostrictive cobalt ferrite (CFO), and observed modest increases in magnetoelectric coupling with increasing porosity. We hypothesized that this was due to the weaker ferroelectricity observed in extremely thin PZT films. Upon switching the ferroelectric to bismuth ferrite (BFO), we find that large (<50%) changes in magnetization were possible in samples with the most residual porosity.

The dissertation of Christopher Ty Karaba is approved.

Alexander M. Spokoyny

Christopher S. Lynch

Richard B. Kaner

Sarah H. Tolbert, Committee Chair

University of California, Los Angeles

2024

TABLE OF CONTENTS

LIST OF FIGURES

LIST OF TABLES

ACKNOWLEDGMENTS

I would not have been able to do any of the work in this dissertation without the help of a multitude of people. First, I want to thank my family for their continued love and support. My parents have always supported whatever dreams and goals I wanted to pursue, and provided examples of how to pursue a career of meaning. My brother has been a constant source of joy for me and living near him while in graduate school was wonderful. Lastly, I need to thank my wife Jessica. While she was not there for much of the work, she put up with me through many struggles and pushed me to complete this work. This work never would have been finished if it were not for her help.

I also want to thank the many professors who have helped me in my academic journey. My first mentor in undergrad, Prof. Joel Bernstein, as well as my other chemistry professors throughout undergrad, Prof. Ali Trabolsi, Prof. Bart Kahr, and Prof. Pance Naumov, helped spur my interest in chemistry and each taught me about what it means to be a passionate chemist in and out of the lab.

I would also like to thank my graduate school professors, both of my academic classes as well as research collaborators. Prof. Ben Schwarz taught me everything I know about quantum mechanics, and Prof. Jane Chang helped with many collaborations. Thank you to my committee members, Prof. Alex Spokoyny, Prof. Richard Kaner, and Prof. Chris Lynch, for providing valuable insight and support. A huge thank you has to go to Dr. Sarah Tolbert, my graduate mentor. She is one of the smartest and most capable scientists I have ever met. I envy her ability to juggle a thousand tasks and still be able to dive to the heart of any problem immediately after hearing it. She truly cares about each of her students and constantly fights for them to have a healthy work life balance, something not many PIs can say. Sarah has also been extremely

PREVIOUS PUBLICATION AND CONTRIBUTIONS OF CO-AUTHORS

Chapter 2 is the published version of Abraham N. Buditama, Kevin Fitzell, Diana Chien, C. Ty Karaba, Shreya K. Patel, Hye Yeon Kang, Jane P. Chang, and Sarah H. Tolbert's manuscript titled "Strain Transfer in porous multiferroic composites of $CoFe_2O_4$ and $PbZr_xTi_{1-x}O_3$". Professor Tolbert and Professor Chang supervised the research. Abraham, Kevin, Diana, and I synthesized the multiferroic nanocomposites. Abraham, Kevin, Diana, Hye Yeon, Shreya and I performed the experiments. Professor Tolbert, Abraham, Shreya, and I wrote the manuscript. All remaining authors gave approval for the final version of the manuscript.

Chapter 3 is the published version of Shreya K. Patel, C. Ty Karaba, Daniel D. Robertson, Jeffrey Chang, Kevin Fitzell, Charlene Z. Salamat, Jane P. Chang and Sarah H. Tolbert's manuscript titled "Increased Magnetoelectric Coupling in Porous Nanocomposites of $CoFe_2O_4$ and $BiFeO_3$ with Residual Porosity for Switchable Magnetic Devices". Shreya and I contributed equally to the manuscript. Professor Tolbert and Professor Chang supervised the research. Jeffrey, Kevin, Shreya and I synthesized the multiferroic nanocomposite – Shreyaand I made the porous CFO framework, then Jeffrey and Kevin filled the inside of the pores with ferroelectric BFO using atomic layer deposition. Shreya, Daniel, Charlene, Jeffrey, and I performed the experiments. Professor Tolbert, Shreya and I wrote the manuscript. All remaining authors gave approval for the final version of the manuscript.

Chapter 4 is the published version of Shreya K. Patel, C. Ty Karaba, and Sarah H. Tolbert's manuscript titled "Delineating magnetization dynamics in solution-processed doped yttrium iron garnet thin films". Shreya and I contributed equally to this paper. Professor Tolbert supervised the research. Shreya and I synthesized the doped YIG films – I synthesized the Ru-doped series, and Shreya synthesized the Ce-doped series. Shreya and I performed all the

experiments. Professor Tolbert, Shreya and I wrote the manuscript. All remaining authors gave approval for the final version of the manuscript.

Education

University of California, Los Angeles *Expected* **September 2024**

- Ph.D. in Materials Chemistry
- Thesis title: Solution-Processed Magnetostrictive and Magnetoelectric Composite Materials for Multiferroic Applications
- Thesis advisor: Dr. Sarah H. Tolbert

New York University Abu Dhabi, United Arab Emirates **May 2014**

- B.S. in Chemistry, *cum laude*
- Minor: Applied Mathematics, Physics

Awards and Honors

Hanson-Dow Teaching Assistant Award **November 2015**

Presentations

Karaba, C. T., Chang, J., Fitzell, K., Patel, S. K., Chang, J. P., Tolbert, S. H. Large Porosity-Dependent Magnetoelectric Coupling in Mesoporous Nanocomposites of $BiFeO_3$ in $CoFe_2O_4$. Magnetism and Magnetic Materials, Las Vegas NV, November 14, **2019**. (Poster presentation)

Karaba, C. T., Patel, S. K., Tolbert, S. H. Solution-Processed Yttrium Iron Garnet Thin Films as Novel Magnetostrictive Materials for Multiferroic Antenna Applications. Advanced Research Strategy Meeting, Translational Applications of Nanoscale Multiferroic Systems, Los Angeles, CA, January 30, **2019**. (Oral presentation)

Karaba, C. T. and Tolbert, S. H.. Solution-Processed Yttrium Iron Garnet Thin Films on Platinum for Multiferroic Antenna Applications. Advanced Research Strategy Meeting, Translational Applications of Nanoscale Multiferroic Systems, Los Angeles, CA, January 30, **2018**. (Poster presentation)

Karaba, C. T. and Tolbert, S. H. Ruthenium Doping of Solution-Processed Yttrium Iron Garnet Thin Films for Increased Magnetostriction. Magnetism and Magnetic Materials, Ferrites and Garnets, Pittsburgh PA, November 7, **2017**. (Poster presentation)

Publications

Patel, S. K.; **Karaba, C. T.;** Tolbert, S. H. Delineating magnetization dynamics in solution-processed doped yttrium iron garnet thin films. *J. Appl. Phys.* **133**, 014102 (**2023**).

Patel, S. K.; **Karaba, C. T.;** Robertson, D. D.; Chang, J.; Fitzell, K.; Salamat, C. Z.; Chang, J. P.; Tolbert, S. H. Increased magnetoelectric coupling in porous nanocomposites of $CoFe_2O_4$ and $BiFeO_3$ with residual porosity for switchable magnetic devices. *ACS Appl. Nano Mater.* **6**, 4141-4150 (**2023**).

Buditama, A. N.; Fitzell, K.; Chien, D.; **Karaba, C. T.;** Patel, S. K.; Kang, H. Y.; Chang, J. P.; Tolbert, S. H. Strain transfer in porous multiferroic composites of $CoFe_2O_4$ and Pb $Zr_xTi_{1-x}O_3$. *Appl. Phys. Lett.* **120**, 192902 (**2022**).

Huang, S; **Karaba, C. T.**; Patel, S. K.; Neal, A.; Tolbert, S. H.; Marian, J. Simulating the non-monotonic strain response of nanoporous multiferroic composites under electric field control. *Appl. Phys. Lett.* **120**, 213501 (**2022**).

Xiao, Z.; Mohanchandra, K. P.; Lo Conte, R.; **Karaba, C. T**.; Schneider, J. D.; Chavez, A.; Tiwari, S.; Sohn, H.; Nowakowski, M. E.; Scholl, A.; Tolbert, S. H.; Bokor, J.; Carman, G. P.; Candler, R. N. Enhanced magnetoelectric coupling in a composite multiferroic system via interposing a thin film polymer. *AIP Advances* **8**, 055907 (**2018**).

Li, X.; Fitzell, K.; Wu, D.; **Karaba, C. T.;** Buditama, A.; Yu, G.; Wong, K. L.; Altieri, N.; Grezes, C.; Kioussis, N.; Tolbert, S.; Zhang, Z.; Chang, J. P.; Amiri, P. K.; Wang, K. L. Enhancement of voltage-controlled magnetic anisotropy through precise control of Mg insertion thickness at CoFeB|MgO interface. *Appl. Phys. Lett.* **110**, 052401 (**2017**).

CHAPTER 1.

Introduction

The control of magnetism is vital in the operation of many electronic devices. As electronic devices scale down to smaller sizes, this control becomes harder and harder to maintain. Traditionally, electromagnets are used to control magnetization via electric current inducing a magnetic field fluctuation. However, electromagnets become difficult to use at smaller scales, because resistive losses increase drastically as the cross-sectional area of the current carrying wire decreases. Thus, for nanoscale magnetic devices, a new method of control is needed that does not rely on current-based electromagnets.

Multiferroic materials look like a potential solution to this problem. Multiferroics are materials that show multiple types of hysteretic order – most useful in this context are materials that exhibit both ferromagnetism and ferroelectricity. However, intrinsically multiferroic materials are rare, and typically do not have particularly large degree of coupling between the electric and magnetic components. Multiferroic composites offer a way of solving this problem. By compositing a piezoelectric material with a magnetostrictive material, we can obtain a coupling between electric fields and magnetic fields not found in pure materials. Multiferroic composites allow for control of magnetism at the small scale, by coupling magnetization to voltage through strain. For example, the piezoelectric material can be strained by applying an electric field, the strain is then transferred to the magnetostrictive component at the composite interface, wherein the strain then changes the magnetization of the magnetostrictive material. In this thesis, we aim to analyze the component materials of the composite, as well as the structure of the composite itself, to enhance magnetoelectric coupling for a variety of small-scale electromagnetic devices.

In the first part of this thesis (Chapter 2), we focus on better understanding magnetostrictive materials for the magnetic component of these multiferroic composites. In general, for the largest magnetoelectric coupling, the magnetostrictive component needs to have large magnetostriction – the magnetization can be easily changed by a relatively small amount of strain. Many of the most common materials with large magnetostriction are metallic, conductive materials. Conductive materials can work in some magnetoelectric applications, but present problems at high frequencies. High-frequency magnetic electromagnetic waves can induce current in conductive materials, leading to large magnetic losses which severely limit performance. For high-frequency applications, an insulating, low-loss magnetostrictive material is thus desirable. In this work, we take one of the lowest magnetic loss materials known, yttrium iron garnet ($Y_3Fe_5O_{12}$, or YIG), and attempt to increase its magnetostriction to make it a useful magnetic material in these high-frequency magnetoelectric contexts. We use sol-gel chemistry to synthesize doped YIG thin films known to have increased magnetostriction. We then characterize the dynamic magnetic behavior of these thin films to show that some doped YIG materials, especially those doped with ruthenium, can be synthesized without increasing magnetic losses at high frequencies. However, these losses are shown to be strongly dependent on crystal nanostructure, with polycrystalline films showing much larger magnetic losses than expected.

In the second part of the thesis (Chapters 3 and 4), we focus on the nanostructure of the magnetoelectric composite materials, and in particular we investigate how this nanostructure affects the magnetoelectric coupling between materials. Most commonly, magnetoelectric composites are composed of dense, layered materials, that are able to couple via strain at the

interface between the layers. However, this approach limits the amount of interfacial surface area, and thus does not generally lead to large strain transfers between materials. Instead, here we investigate nanostructured composite materials that have a three-dimensional interface and thus vastly increased interfacial area. In addition, these nanostructured composites contain open residual porosity, which further enhances the amount of strain the system is capable of. These composites are synthesized one material at a time – first, a nanoporous magnetostrictive framework is synthesized via block copolymer templating. Then, atomic layer deposition is used to coat the inside of the pores of the magnetostrictive framework with a ferroelectric material.

In chapter three, we investigate a composite composed of lead zirconate titanate ($PbZr_xTi_{1-x}O_3$, or PZT) as the ferroelectric material, and cobalt ferrite ($CoFe_2O_4$, or CFO) as the magnetostrictive material. Here, we vary the thickness of the PZT layer to induce different amounts of residual porosity in the resulting PZT-CFO composite. We utilize high-resolution X-ray diffraction to show that the amount of residual porosity affects magnetoelectric coupling greatly, most likely due to the pores having more room to flex. In chapter four, we introduce a different ferroelectric material into the same nanoporous cobalt ferrite framework used in chapter three in order to increase magnetoelectric coupling. Bismuth ferrite ($BiFeO_3$, BFO) has the potential to have a more stable ferroelectric response than PZT at the very small sizes used in these nanocomposites. We find that these BFO-CFO nanocomposites show a remarkable magnetoelectric coupling of more than a 50% decrease in magnetization upon application of an electric field.

CHAPTER 2.

Delineating Magnetization Dynamics in Solution-Processed Doped Yttrium Iron

Garnet Thin Films

Chapter 2 describes the synthesis and magnetic loss in doped yttrium iron garnet films prepared by sol-gel chemistry.

This chapter was reproduced from Patel, S.K.; Karaba, C.T.; Tolbert, S.H. "Delineating Magnetization Dynamics in Solution-Processed Doped Yttrium Iron Garnet Thin Films" *J. Appl. Phys.* 2023, *133*, 014102, with the permission of AIP Publishing.

A reprint of the supporting information is given in Appendix A.

Delineating Magnetization Dynamics in Solution-Processed Doped Yttrium Iron Garnet Thin Films

Shreya K. Patel, C. Ty Karaba, Sarah H. Tolbert

ABSTRACT.

In this work, thin films of ruthenium-doped and cerium-doped yttrium iron garnet were deposited on silicon using sol-gel chemistry. Doped YIG could be produced in phase pure form up to a precursor stoichiometry of $Y_3Ru_{0.1}Fe_{4.9}O_{12}$ and $Ce_{0.7}Y_{2.3}Fe_5O_{12}$. Both dopants significantly increase the coercivity and anisotropy field of the materials, either due to domain wall pinning or increased spin orbit coupling from the dopant. To delineate these two effects, the dynamic magnetic properties were studied using stripline ferromagnetic resonance (FMR). The FMR linewidth was separated into intrinsic loss and inhomogeneous line broadening. Inhomogeneous line broadening was found to dominate the magnetic losses in all the films, likely due to magnon scattering off grain boundaries, but the Gilbert damping remained fairly low. Comparing the two dopants, it was found that the Gilbert damping increased more in Ce:YIG films than in the Ru:YIG films. This finding was corroborated by changes in the anisotropy field of the films, indicating a larger contribution from spin orbit coupling from cerium than from ruthenium. Surprisingly, while magnetic loss globally increased with higher substitution, adding a small amount of dopant actually reduced the inhomogeneous line broadening in both sets of films. This was corroborated by crystallite size. The damping in Ru:YIG also decreased with a small amount of dopant, which has been predicted by Kittel for doped garnets. Thus, it follows that there is an ideal doping regime where sol-gel YIG can be doped at low levels without increasing magnetic loss.

5

INTRODUCTION.

Yttrium iron garnet (YIG) is a widely used ferrimagnetic material. Since its discovery, it has become extremely popular in spintronic devices, such as in filters[1,2] and antenna devices[3-5], due to its ultralow damping and magnetic softness.[6,7] YIG has also been integrated in many telecommunication devices, such as isolators[8–10] and phase shifters [11–13], since it has the unique combination of low optical loss (little absorption in the visible and IR) and a high Faraday effect.

It has been shown that YIG can be doped with many different transition metal and rare earth metals, which can dramatically change its magnetic properties, such as magnetostriction and Faraday effect.[14–19] In spintronic devices, it is desirable to have materials that exhibit high magnetostriction and low magnetic damping. While YIG exhibits extremely low damping, it has not been considered for such spintronic applications because it has little magnetostriction. Doping YIG with heavier elements, however, has been shown to increase its magnetostriction, and so doped YIG has the potential to enable new spintronic devices.[16,17,20] In addition, doped YIG, particularly with bismuth and cerium, has become extremely popular in telecommunication devices, since doping can increase the Faraday effect of the material, increasing its magneto optical figure of merit (the Faraday effect of the material divided by its optical loss).[14,18,21–23] An increased magneto optical figure of merit allows for the miniaturization of telecommunication devices. Thus, studies of doped YIG systems are crucial to enable future devices.

While these results are promising, it has also been shown that doping YIG can increase its magnetic loss, which is detrimental to spintronic and telecommunication applications respectively.[18,24] Thus, device optimization relies on the ability to study and understand the magnetic loss over a wide range of doping parameters, including dopant ion, where the dopant substitutes, and dopant concentration. Magnetic losses can be characterized by looking at the

6

linewidth of ferromagnetic resonance (FMR). For device design, it is particularly helpful to investigate the FMR linewidth across a range of frequencies. This can be accomplished using stripline FMR, which allows the FMR linewidth to be studied over a broad range of frequencies.[25,26]

In this work, we study the effect of doping on FMR at different sites in its crystal structure. The structure of YIG is well known.[27–29] Within the cubic crystal structure of YIG, there are three sublattice sites – dodecahedral ("*c*" sites), octahedral ("*a*" sites), and tetrahedral ("*d*" sites). Yttrium preferentially occupies the dodecahedral site. The five Fe^{3+} ions in a given formula unit of YIG are then split between two other antiferromagnetically coupled sites – two Fe^{3+} ions sit on octahedral *a* sites and the remaining three sit at tetrahedral *d* sites. As a result, YIG is a ferrimagnet with a net magnetization of one Fe^{3+} ion (5 μ_B) per formula unit. In addition to the antiferromagnetic coupling between the octahedral and tetrahedral sites, there is a weaker magnetic coupling between the dodecahedral moment (if present) and the octahedral sites, such that the tetrahedral moments couple antiferromagnetically to both the dodecahedral and tetrahedral moments.

In this work, we first investigate doping a heavier transition metal in the *octahedral and tetrahedral* iron sites of the YIG crystal structure. We chose ruthenium for this, as it has been shown to substitute at both the Fe^{3+} *a* and *d* sites in bulk crystals.[16,30] Additionally, while it has been shown that the FMR linewidth of ruthenium-doped YIG (Ru:YIG) does increase with doping, it remains at relatively low levels compared to other magnetic materials in the bulk single crystal form.[30] However, Ru:YIG has not been investigated in the thin-film form, which is far more practical for device integration.

In addition to studying the effects of doping a transition metal at the *octahedral* site, we also chose to study the effects of doping at the *dodecahedral* site to investigate the impact its coupling can have on the total magnetic properties of the doped film. We chose cerium-doped YIG (Ce:YIG), for this purpose. Ce:YIG is a well-known material for its large magneto-optical figure of merit and increased magnetostriction.[17,18,31] The choice of Ru:YIG and Ce:YIG help us isolate different effects on the magnetic properties. Ru^{3+} has the same number of valence electrons as Fe^{3+} (both d^5) but greater spin-orbit coupling, while Ce^{3+} has one valence electron in its $4f$ orbital, in contrast to Y^{3+}, which has a full $4p$ orbital. This extra electron in Ce^{3+}, as compared to Y^{3+}, has been shown to have interesting effects on the magnetic properties of YIG, such as changes in saturation magnetization, but its effect on magnetic loss across a range of dopant stoichiometries are not well understood.[18,22,23,32,33]

While YIG films are often deposited by high energy methods such as sputtering, PLD, or LPE, here, we synthesize films using sol-gel chemistry, since it is much more scalable and easier to use to study a wide range of dopants. In sol-gel chemistry, metal salts are dissolved in solution to for a 'sol', and then undergo condensation reactions to form metal-oxygen bonds, resulting in a metal oxide polymer known as a 'gel'. This technique is inexpensive, easily scalable, and allows for exploration of a wide range of dopant stoichiometries by simply changing precursor stoichiometry. There have been many successful studies that use both wet chemical synthesis and solid state chemistry to make YIG powders and nanoparticles.[32,34–40] Some of these investigations even study magnetic loss using FMR.[41,42] While the work on nanoparticles of YIG is interesting, thin films are more easily integrated into devices. It has been shown that thin films of YIG can be easily deposited on a range of substrates, including silicon, quartz, glass, and lattice matched substrates (for example, gadolinium gallium garnet, or GGG) using sol-gel methods.[43–48] Some

studies have also investigated the dynamic magnetic properties of YIG films using ferromagnetic resonance and electron spin resonance.[43,49] There has also been previously published work on doping sol-gel YIG films, with elements such as erbium, bismuth, and cerium.[14,16,20,31,33,35,50,51] While each of these works characterized the static magnetic properties in depth, many magnetic properties, including high-frequency magnetic behavior, have not been previously investigated. Furthermore, sol-gel derived ruthenium-doped films have not been previously studied.

MATERIALS AND METHODS.

$Y(NO_3)_3 \cdot 6H_2O$, (99.9%, ACROS Organics), $Fe(NO_3)_3 \cdot 9H_2O$ (99+%, ACROS Organics), $RuCl_3 \cdot xH_2O$, (35%-40% Ru, ACROS Organics), $Ce(NO_3)_3 \cdot 6H_2O$ (99.5%, Alfa Aesar), and ethanolamine (98+%, Alfa Aesar) were used for the synthesis with no further purification.

For undoped sol-gel YIG, a modified procedure from the literature was used.[43] A 3:5 mole ratio of $Y(NO_3)_3 \cdot 6H_2O$ to $Fe(NO_3)_3 \cdot 9H_2O$ was used. In a typical synthesis, $Fe(NO_3)_3 \cdot 9H_2O$ (1.01 g) and $Y(NO_3)_3 \cdot 6H_2O$, (0.58 g) were dissolved in 1.5 mL of methoxyethanol with 40 μL of ethanolamine. The solution was allowed to magnetically stir for several hours, or overnight. For doped YIG, the dopant stoichiometry was varied. For Ru:YIG, the dopant ratio ranged from 0.025-0.1:1 mol (5 – 21 mg of $RuCl_3 \cdot xH_2O$) of Ru:Fe, and for Ce:YIG the dopant mole ratio of Ce:Y ranged from 0.2-0.8:1 mol [43.4-174 mg of $Ce(NO_3)_3 \cdot 6H_2O$].

Solutions were filtered with a PTFE syringe filter (Cole-Parmer, 0.2 μm) before spin coating onto 2 x 2 cm^2 (100) Si substrates. Silicon substrates were washed with ethanol and plasma etched before deposition. Films were spincoated at 3000 rpm for 30 seconds. Immediately after spincoating, films were calcined on a 400 °C hot plate in air for about a minute, then immediately cooled down to room temperature. Though not discussed in this work, this method was also able

to be used for other substrates like platinized silicon, (Pt (100 nm) -Ti (5 nm) - SiO_2 (thermally oxidized, thickness about 1 μm) -Si (100)), thermally oxidized SiO_2 (thickness about 1 μm) on Si(100)), and GGG, with the exception of not plasma etching the GGG before deposition. Rapid thermal annealing (RTA) (MPTC RTP 600xp Rapid Thermal Annealer) was used to crystallize the films under oxygen at 900 °C with a 30 second ramp and a 5 minute hold.

For stripline FMR measurements, it was found that the signal-to-noise ratio was poor for films deposited in the way described above. Therefore, thicker, multilayered films (approximately 200 nm) were made specifically for the stripline FMR measurements. This was done by spin coating the sol on silicon, calcining on a 400 °C hot plate, then repeating this process two more times for three total layers. The film was then crystallized by the same RTA process with the RTP as described above. Characterization of these thicker films can be found in the supporting information (figure S1 in the supplementary material).

X-ray diffraction patterns were collected either through grazing incidence wide angle X-ray scattering experiments (GIWAXS) with a 2D detector at an X-ray wavelength of λ =0.98 Å (thinner films) or using conventional $\theta - \theta$ powder diffraction performed on a PANalytical X'Pert Pro diffractometer at Cu Kα (λ =1.54 Å) radiation (thick films). The 2D diffraction patterns were reduced to 1D patterns using the WAXtools macro[52] in the Nika 2D package[53] for IgorPro 6.37 (WaveMetrics, Lake Oswego, OR, USA). Diffraction patterns were compared to JCPDS reference cards #00-043-0507 (for YIG) and #00-001-0800 (for ceria) using X'Pert Highscore Plus 2.0.1. Static magnetic properties were measured at room temperature using a Quantum Design MPMS3 superconducting quantum interference device (SQuID) magnetometer.

Dynamic magnetic properties were measured using a stripline ferromagnetic resonance (FMR) set up as described elsewhere.[25,54] Briefly, a short-circuited stripline is connected to a

vector network analyzer (VNA). The sample is directly placed under the stripline as the VNA is used to tune frequency and a conventional electromagnet is used to tune the magnetic field applied parallel to the sample. The reflection coefficient (S_{11}) was measured as a function of both the biasing magnetic field and the frequency. As mentioned above, thicker films were needed to obtain reasonable absorption in the stripline measurement. While not discussed in this work, the authors have also used electron spin resonance (ESR) with an X-band cavity to study dynamic magnetic properties. While ESR is tuned to a cavity resonance and thus cannot provide data across a range of frequencies as the stripline set up used in this work, the cavity in ESR would allow for the detection of small absorbances in thinner films.

RESULTS AND DISCUSSION.

Grazing-incidence wide angle X-ray scattering (GIWAXS) was used to ensure the desired crystal structure of YIG was formed using the sol-gel method for both Ru:YIG and Ce:YIG [Fig. 1(a)]. Across the range of dopant stoichiometries investigated, Ru:YIG maintained the YIG crystal structure up to a dopant concentration of $Y_3Ru_{0.1}Fe_{4.9}O_{12}$ (figure 1(a)). For Ce:YIG, the doped films were able to maintain their crystal structure with similar phase purity until a precursor stoichiometry of $Ce_{0.75}Y_{2.25}Fe_5O_{12}$ [Fig. 1(b)]. Further cerium substitution resulted in the formation of ceria (CeO_2).

While it could not be seen at the resolution of the GIWAXS, the thin films in this study are likely under slight tensile stress due to the annealing process. Silicon has a much lower thermal expansion coefficient than YIG, and so will contract less than the YIG layer upon cooling the after RTA treatment. Since the YIG layer is clamped in the in-plane direction, the films are thus expected to show in-plane tensile stresses.

The static magnetic properties of the doped YIG films were investigated using superconducting quantum interference device (SQuID) magnetometry (Fig. 2). The saturation magnetization of all the sol-gel films studied in this work are relatively close to the literature values for those of YIG.[16–18,30] However, the saturation magnetization of the cerium doped films was found to be slightly higher, between 140 and 150 emu/cc. As mentioned previously, the Ce^{3+} cation has one valence electron in its $4f$ orbital compared to Y^{3+}, which has a full $4p$ orbital. This extra electron at the c site couples to YIG's ferrimagnetic sublattices, increasing its overall saturation
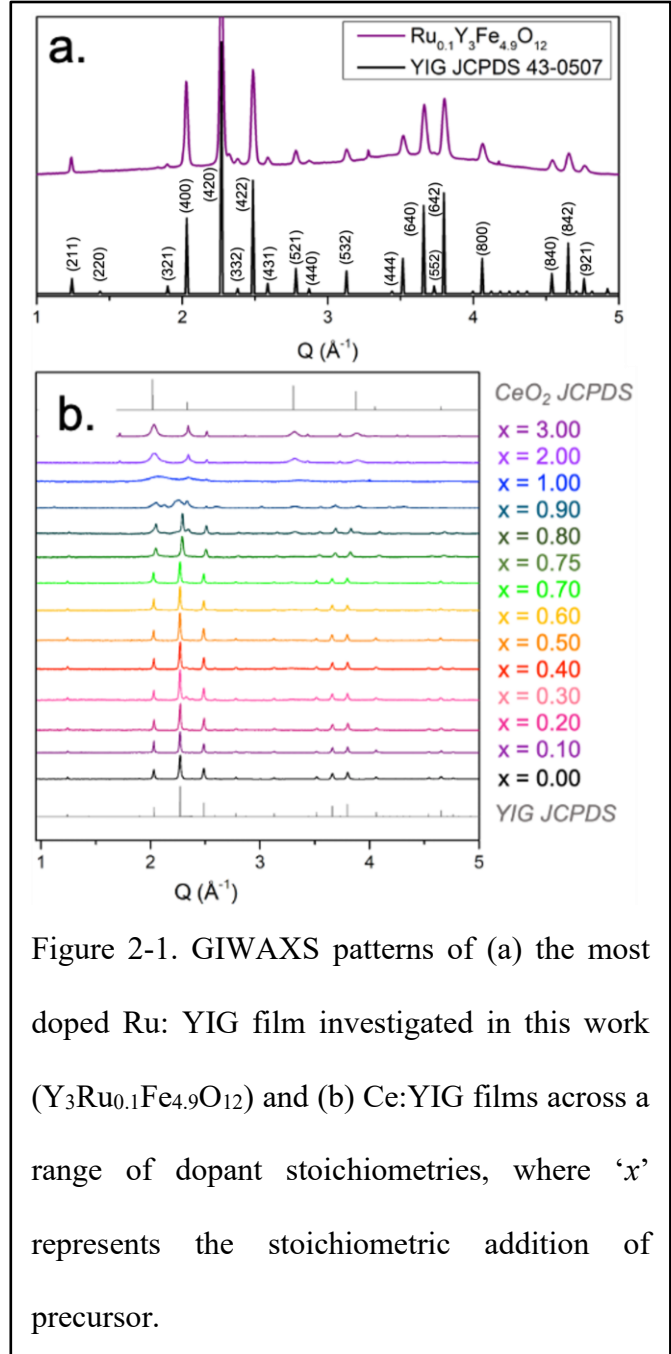
Figure 2-1. GIWAXS patterns of (a) the most doped Ru: YIG film investigated in this work ($Y_3Ru_{0.1}Fe_{4.9}O_{12}$) and (b) Ce:YIG films across a range of dopant stoichiometries, where 'x' represents the stoichiometric addition of precursor.

magnetization. This increase in saturation magnetization is documented in the literature, and has been observed experimentally in Ce:YIG films deposited by PLD as well.[18,22,32]

Here, we paid special attention to the coercivity, which can be indicative of general anisotropy trends [Figs. 3(a) and 3(b)]. The coercivity of the undoped films was found to be between 20-30 Oe, which is in good agreement with literature values for sol-gel YIG films.[32,34,37] While the coercivities in this work were found to be consistent with other *sol-gel films*, it is important to distinguish that the coercivities of *single-crystal films* are often reported to be significantly lower, around 1-5 Oe.[6,55] As will be discussed in detail below, the spin coating deposition process results in more defects (such as grain boundaries and pores) than many high-energy methods of YIG fabrication, including LPE, PLD, and sputtering. Grain boundaries, cracks, and pores can cause domain wall pinning, increasing the overall coercivity of the film. Additionally, as mentioned previously, the sol-gel films described in this work have residual

Figure 2-2. MH loops for Ru:YIG (a) and for Ce:YIG (b). In all plots, '*x*' represents stoichiometric concentration of dopant in the chemical formula of YIG, so for Ru:YIG, $x = Y_3Ru_xFe_{5-x}O_{12}$ and for Ce:YIG, $x = Ce_xY_{3-x}Fe_5O_{12}$.
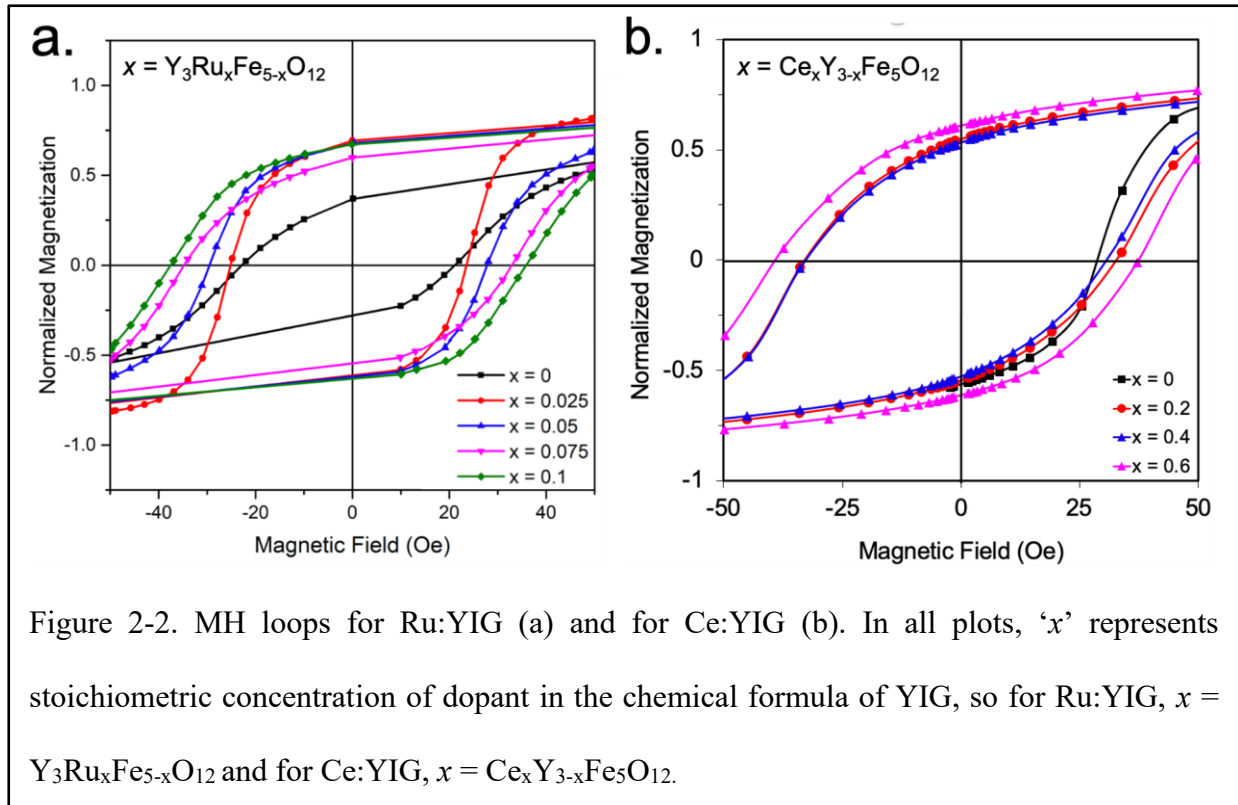
tensile stresses from the difference in thermal expansion between YIG and silicon during the annealing process. These stresses add to the films' overall magnetoelastic anisotropy, which contributes to the overall coercivity of the undoped films. Though the coercivities of sol-gel films are a bit higher than epitaxial films, the films are still very magnetically soft.

Having confirmed that the undoped films had comparable coercivities to those reported in literature, the coercivities of the doped films were also investigated through SQuID magnetometry (Figs. 2 and 3). The coercivity in the Ru:YIG films were found to increase significantly upon doping, corresponding to a 39% increase [Fig. 3(a)]. Similarly, the coercivity of the Ce:YIG films increased as a function of dopant concentration but showed only a 33% increase across a much broader range of doping concentrations [Fig. 3(b)]. Note that there is some variation in the coercivity of the undoped YIG due to variations in the sol-gel process, and this likely accounts for slightly higher values obtained for Ce:YIG compared to those of Ru:YIG. There are two potential causes for the general trend of increasing coercivity as a function of dopant concentration. First, the substitution of an atomically heavier element (such as ruthenium for iron and cerium for yttrium) has greater spin-orbit coupling, which adds to the doped film's total magnetocrystalline anisotropy. This increase in magnetocrystalline anisotropy should result in increased coercivity in the doped film compared to the undoped film.[24] Second, as mentioned previously, point defects and magnetic inhomogeneities can contribute to the films' coercivity due to domain wall pinning. While the GIWAXS shows that the crystal structure is maintained as being phase pure within the detection limit, it is possible that a small amount of the dopant can also sit at grain boundaries, and act as pinning sites.

In order to delineate whether the coercivity was increasing due to increased magnetic anisotropy or from defects caused by the introduction of dopants, the anisotropy field of both sets of films were investigated using the commonly-used approach-to-saturation method [Figs. 3(c) and 3(d)]. [56] Globally, for both Ru:YIG and Ce:YIG films, the anisotropy fields followed the same trend seen in the coercivity, showing an increasing anisotropy field with increasing dopant concentration. This confirms that the increase in coercivity is most likely a result of increased magnetocrystalline anisotropy due to spin orbit coupling introduced by the atomically heavier dopant, rather than the increase in coercivity being caused by domain wall pinning at defects introduced by the dopant. Interestingly, the anisotropy fields for the Ce:YIG were slightly higher than Ru:YIG (Fig. 3), which is to be expected since the Ce:YIG films also showed larger values for coercivity.

To understand why magnetic anisotropy would be higher in the Ce:YIG films than in the Ru:YIG films, the dynamic magnetic properties of the doped YIG films were investigated using stripline FMR. [25,26,57] In this experiment, the sample is placed directly under the stripline passing the applied frequency, and a conventional electromagnet is used to tune the magnetic field applied parallel to the sample. The normalized reflection coefficient (S_{11}, shown by the intensity

Figure 2-3. Trends in coercivity (figure 3a and 3b) and anisotropy field (figure c and d) for Ru:YIG (figures 3a and 3c) and Ce:YIG (figures 3b and 3d).
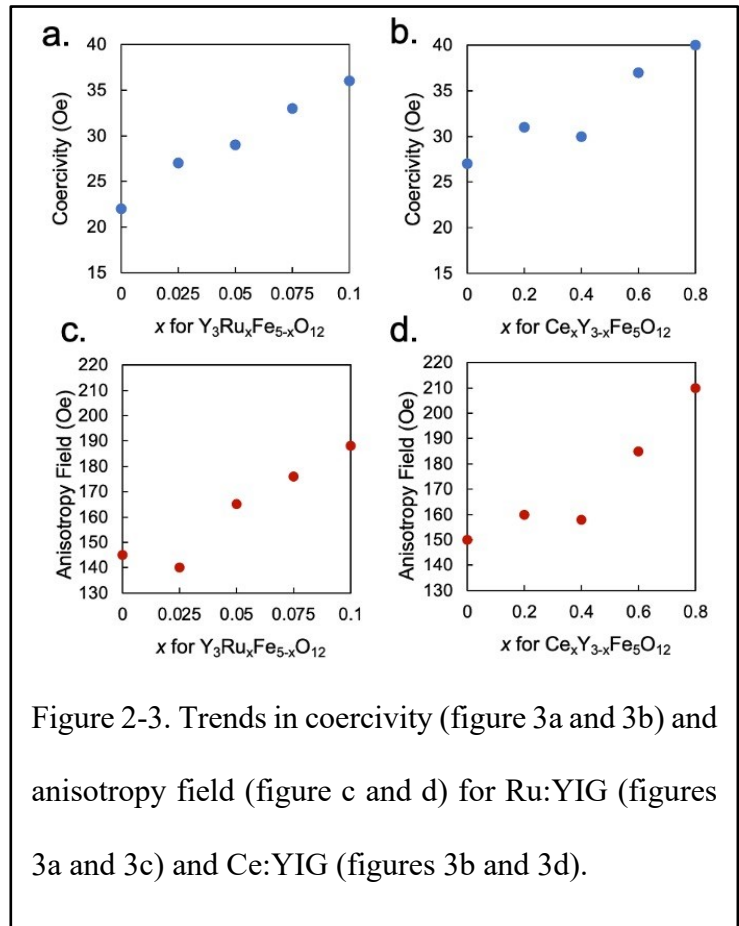
of the color bar below each FMR figure) was measured as a function of both the applied frequency and magnetic field. It is important to note that thicker films were used for this experiment in order to obtain stronger absorption in the measurement (see experimental for details). Characterization for the thicker films can be found in the supporting information. Thicker films in this study were needed to obtain reasonable absorption for stripline FMR measurements, and as seen from the 2D plots for Ru:YIG (Fig. 4) and Ce:YIG (Fig. 5), the films studied in this way showed strong S_{11} absorption, with a liner shift in the resonance frequency as a function of the applied magnetic field, as expected.

Figure 2-4. 2D plots of S_{11} absorption for Ru:YIG films collected from 500 MHz to 5 GHz and from a magnetic field of 0 Oe up to 1200 Oe for varying dopant concentrations: (a) undoped YIG, (b) $x = 0.025$, (c) $x = 0.05$, (d) $x = 0.1$ for $x = Y_3Ru_xFe_{5-x}O_{12}$. The color bar shows normalized absorption.
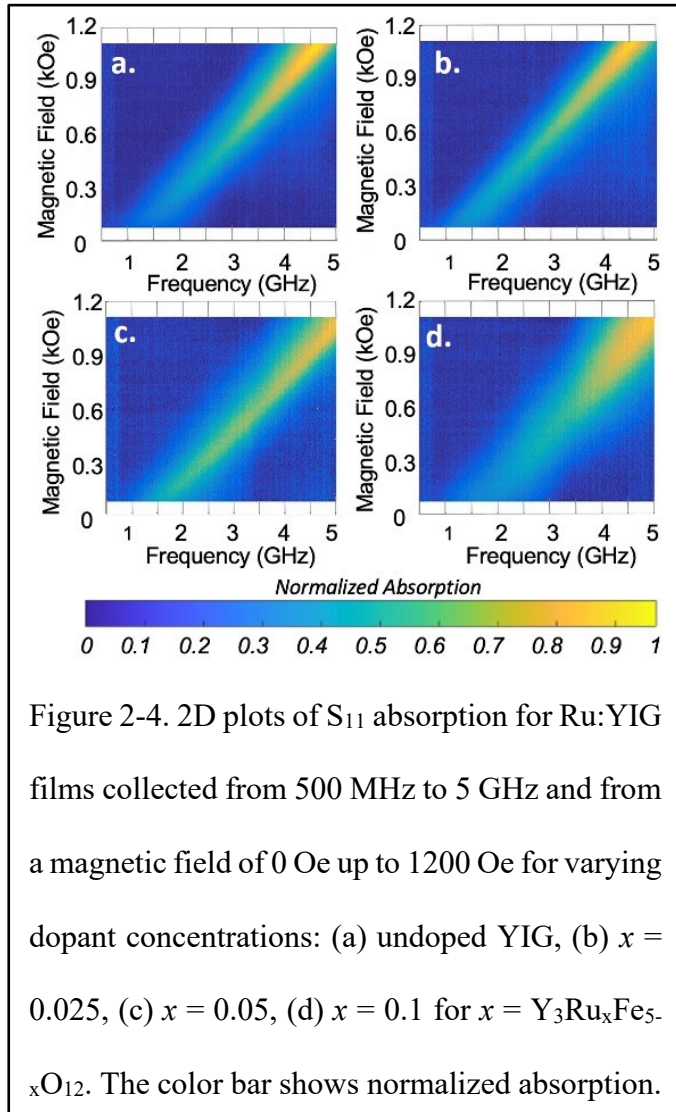
The width of S_{11} absorption correlates with magnetic loss, and thus this is the key parameter to quantify. We first looked at the total magnetic loss of undoped films. The linewidth was obtained by plotting S_{11} absorption as a function of the applied magnetic field, and then fitting this peak to find the full width at half maximum, giving us the linewidth in units of magnetic field (Oe). The experimentally obtained linewidth for the average between two sets of undoped films at 4 GHz was found to be about 260 Oe. This is much higher than what has been observed for epitaxial films of YIG on

Figure 2-5. 2D plots of S_{11} absorption for Ce:YIG films collected from 100 MHz to 6 GHz and from a magnetic field of 0 Oe up to 2000 for varying dopant concentrations: (a) undoped YIG, (b) $x = 0.2$, (c) $x = 0.4$ (d) $x = 0.6$ for $Ce_xY_{3-x}Fe_5O_{12}$. The color bar shows normalized absorption.
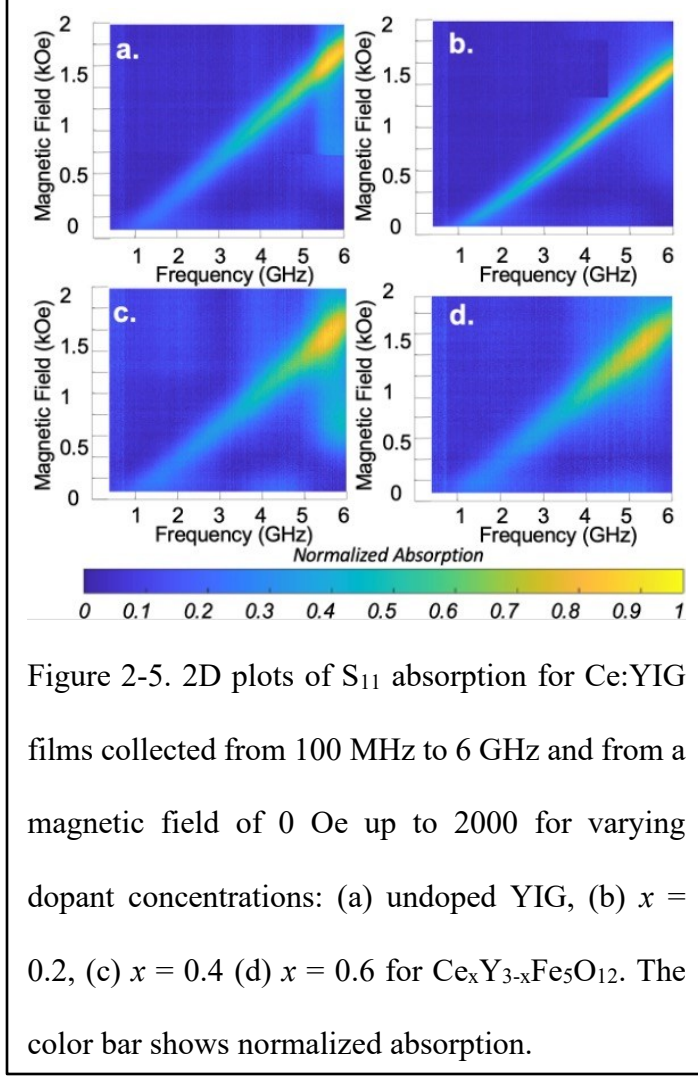
lattice matched substrate (GGG) made from LPE or PLD (from 2-10 Oe at the same frequency).[6,18,58] In order to understand the sources of magnetic losses in the sol-gel films utilized in this work, we examined the linewidth as a function of frequency for both Ce:YIG and Ru:YIG [Figs. 6(a) and 6(b)]. According to Eq. (1), the linewidth can be separated into a frequency-dependent component (i.e. Gilbert damping, which is generally dominated by eddy current losses in metals) and a frequency independent inhomogeneous line broadening, [59]

$$\Delta H_{FWHM} = \Delta H_0 + \alpha\left(4\pi/\sqrt{3}\gamma\right)f \qquad (1)$$

Here, ΔH_{FWHM} is the total FMR linewidth, found by taking the full width half maximum of the absorption peak, ΔH_0 is the inhomogeneous line broadening, α is the Gilbert damping of the material, γ is the gyromagnetic ratio, and f is the resonant frequency. The frequency dependent losses come from the materials' intrinsic loss, represented by the materials' Gilbert damping. Inhomogeneous line broadening, ΔH_0, is the extrinsic line broadening, caused by magnon

scattering off of defect sites, such as pores, cracks, and impurities.[60–62] From Eq. (1), the losses

from inhomogeneous line broadening and the frequency dependent losses can therefore be

separated by plotting the full width half maximum linewidth (ΔH_{FWHM}) and as a function of the

applied frequency, where the slope of the line is proportional to the frequency-dependent losses

and the *y*-intercept is the inhomogeneous line broadening.

Such linewidth vs. frequency plots for undoped films (black symbols) are shown in Fig.

6(a) (for Ru:YIG) and Fig. 6(b) (for Ce:YIG). Single crystal YIG is known to have very little

intrinsic loss, having one of the lowest Gilbert damping factors known, so it can be expected that

the intrinsic, frequency dependent losses should be quite low[23,63]. Based on the relatively small

slope (and thus, damping) of frequency-dependent FMR linewidths in the undoped films, we can

conclude that the films studied here indeed have low intrinsic losses. We can calculate the Gilbert

damping (α) by first using the Kittel equation [Eq. (2)] to solve for the gyromagnetic ratio (γ) of

the undoped YIG films,

$$f = (\gamma/2\pi)\sqrt{H_r(H_r + 4\pi M_s)} \qquad (2)$$

Where f is again the frequency, H_r is the resonant magnetic field, and M_s is the saturation

magnetization of the film, obtained from the SQuID data discussed above.[64] Once the

gyromagnetic ratio has been determined from the Kittel equation (equation 2), equation (1) can be

used to solve for Gilbert damping. Since experimentally obtained values for resonant magnetic

field were used to calculate the gyromagnetic ratio, the original Kittel equation does not need to

be modified to include frequency shifts due to additional magnetocrystalline anisotropy. Values

for Gilbert damping and inhomogeneous line broadening can all be found in Table I and plots of

Gilbert damping as a function of dopant concentration can be found in Fig. 6(c) (for Ru:YIG) and Fig. 6(d) (for Ce:YIG). For undoped films, about 90% of the total FMR linewidth was found to be the result of inhomogeneous line broadening, confirming that the inhomogeneous line broadening is the main source of losses in the films in this work. The films discussed in this work

Figure 2-6. Plot of FMR linewidth as a function of frequency for (a) Ru:YIG and (b) Ce:YIG and calculated Gilbert damping for (c) Ru:YIG and (d) Ce:YIG.
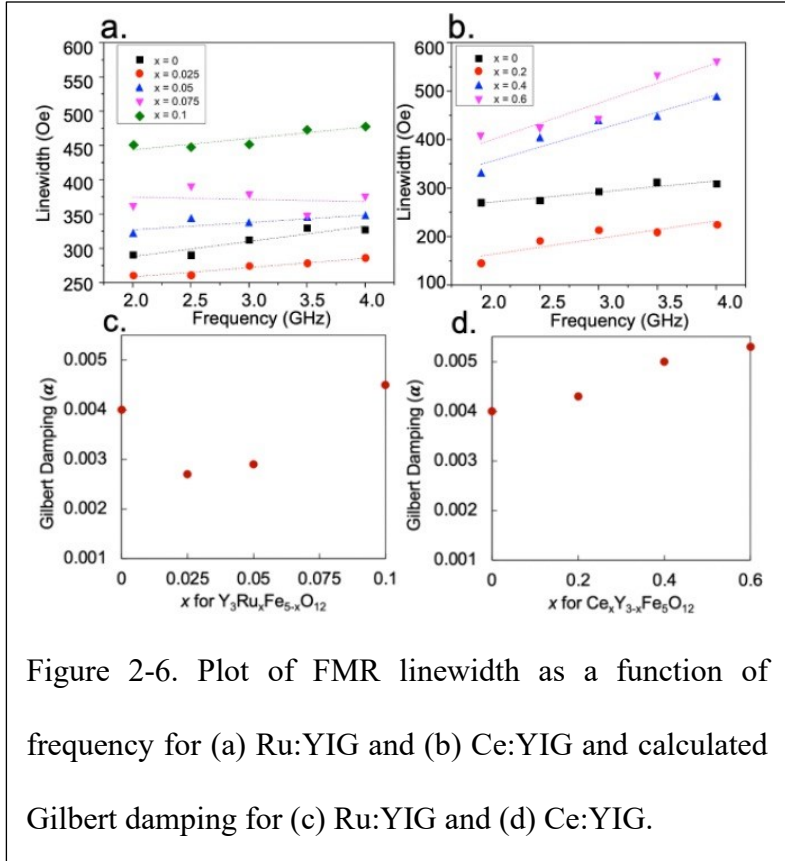
are polycrystalline, and so they contain many grain boundaries. Additionally, as mentioned previously, the films discussed in this work are expected to have defects such as micropores and cracks due to the sol-gel deposition process. It should also be noted that the films used for stripline measurements were multilayered films (see experimental and Fig. S1 in the supplementary material for more details and characterization), which can contribute to cracks and defects that broaden the linewidth further. These grain boundaries, micropores, and cracks can be seen in the cross-sectional SEM image in Fig. S1(c) in the supplementary material, and all should result in magnon scattering off these sites, damping the magnetic excitation and causing increased inhomogeneous line broadening.[59,60,65]

Though solution processing was utilized here because it is scalable and allows us to easily tune the dopant concentration, the high inhomogeneous line broadening seen here is a significant

disadvantage. This broadening can be reduced with methods that allow for the growth of single crystal, epitaxial films, such as those formed by sputtering on GGG, PLD, LPE, and polymer assisted deposition (PAD).[6,48,58] Despite the high inhomogeneous line broadening caused by the sol-gel process, the Gilbert damping of undoped YIG was found to be quite low (3.0×10^{-3}) and the films provide an ideal way to examine changes in Gilbert damping as a function of doping level.

Dopant	Inhomogeneous line broadening (ΔH_0)	Gilbert damping (α)
Undoped*	262 Oe	3.5×10^{-3}
$Y_3Ru_{0.025}Fe_{4.975}O_{12}$	256 Oe	2.2×10^{-3}
$Y_3Ru_{0.05}Fe_{4.95}O_{12}$	325 Oe	2.4×10^{-3}
$Y_3Ru_{0.1}Fe_{4.9}O_{12}$	445 Oe	4.0×10^{-3}
$Ce_{0.2}Y_{2.8}Fe_5O_{12}$	164 Oe	3.9×10^{-3}
$Ce_{0.4}Y_{2.6}Fe_5O_{12}$	321 Oe	4.3×10^{-3}
$Ce_{0.6}Y_{2.4}Fe_5O_{12}$	354 Oe	4.8×10^{-3}

Table 2-1. Values for inhomogeneous line broadening and Gilbert damping for films studied in this work. (*averaged over data from multiple undoped films).

We now shift to looking at the losses in both sets of doped films. Similar to the undoped films, the doped films were found to also have relatively high inhomogeneous line broadening, as can be seen by looking at the *y*-intercepts of the frequency vs linewidth plots for Ru:YIG [Fig. 6(a)] or Ce:YIG [Fig. 6(b)]; the values are also quantified in Table I. In both sets of doped films, as dopant concentration increased, the inhomogeneous line broadening generally increased as well. This is likely because the addition of dopants resulted in an increased number of point defects, which increased magnon scattering, as discussed earlier. However, since GIWAXS data show no signs of impurity phases, we expect impurity domains to make up a relatively small contribution of total inhomogeneous line broadening. Diffraction peak widths also do not change significantly,

suggesting that point defects are also not the major cause of magnetic loss. Thus, we expect that the increasing inhomogeneous line broadening as a function of increasing dopant stoichiometry is largely a result of the increased magnetic disorder in the sublattice. Since the films studied in this work are not fully substituted films, the spins are placed in different electronic environments, creating disorder that can inhomogenously broaden the absorption. This has been shown to broaden zero field linewidth in other sets of doped YIG films as well.[18] Surprisingly, inhomogeneous line broadening (and the total linewidth) was found to *decrease* upon addition of only small amounts of dopant [represented by the red data presented in Figs. 6(a) and 6(b)], and then to increase again with large dopant addition. This phenomenon will be discussed later in the text.

While inhomogeneous line broadening is the predominant source of losses in both Ru:YIG and Ce:YIG, the frequency dependent losses (i.e. the Gilbert damping) were also found to increase as a function of dopant concentration. Gilbert damping values are included in Table I and plotted as a function of dopant concentration in Fig. 6(c) (Ru:YIG) and Fig. 6(d) (Ce:YIG). This global increasing trend is to be expected, as Ce^{3+} and Ru^{3+} are atomically heavier than Y^{3+} and Fe^{3+} respectively. Heavier ion substitution increases the spin orbit coupling of the overall material, which adds additional magnetocrystalline anisotropy. This is confirmed by our earlier findings on the anisotropy field of the doped films. This increase in spin orbit coupling causes fast spin relaxation, which increases the frequency dependent losses.[24] Moreover, in comparing the two sets of dopants, it was found that the intrinsic losses in Ru:YIG films [Fig. 7(c)] seemed to increase less with subsequent dopant concentration than in Ce:YIG films (figure 7(d)). This is echoed by our findings that the anisotropy fields of Ru:YIG [Fig. 3(c)] are smaller than Ce:YIG [Fig. 3(d)]. The smaller increase with Ru-doping can be explained by two things. First, the relative

21

concentration of ruthenium in the films studied here is significantly less than the amount of cerium dopant in the Ce:YIG films. Second, the relative amounts spin-orbit coupling introduced by ruthenium is expected to be less than cerium, as cerium is much heavier than yttrium, while ruthenium is only slightly heavier than iron.

Interestingly, while the global trends for magnetic loss are increasing, it was found in both Ru:YIG and in Ce:YIG that adding in a small amount of dopant (for Ru:YIG, up to $Y_3Ru_{0.05}Fe_{4.95}O_{12}$ and for Ce:YIG, $Ce_{0.2}Y_{2.8}Fe_5O_{12}$) actually *decreases* the total FMR linewidth [Figs. 4(a) and 5(a)], but with higher dopant concentration [Figs. 4(b)-4(d) and 5(b)-(d)], the linewidth broadens again. This was surprising, as the magnetic loss was expected to *increase* according to Vegard's law with additional dopant ion concentration. The decrease in inhomogeneous loss can be explained by using the Scherrer width of the (420) peak from the diffraction patterns presented in Fig. 1 to calculate a crystalline domain size. As shown in Fig. 7, in both Ru:YIG and Ce:YIG, adding a small amount of dopant produces an increased domain size, which is then followed by a decrease in domain size with further doping. The increase likely
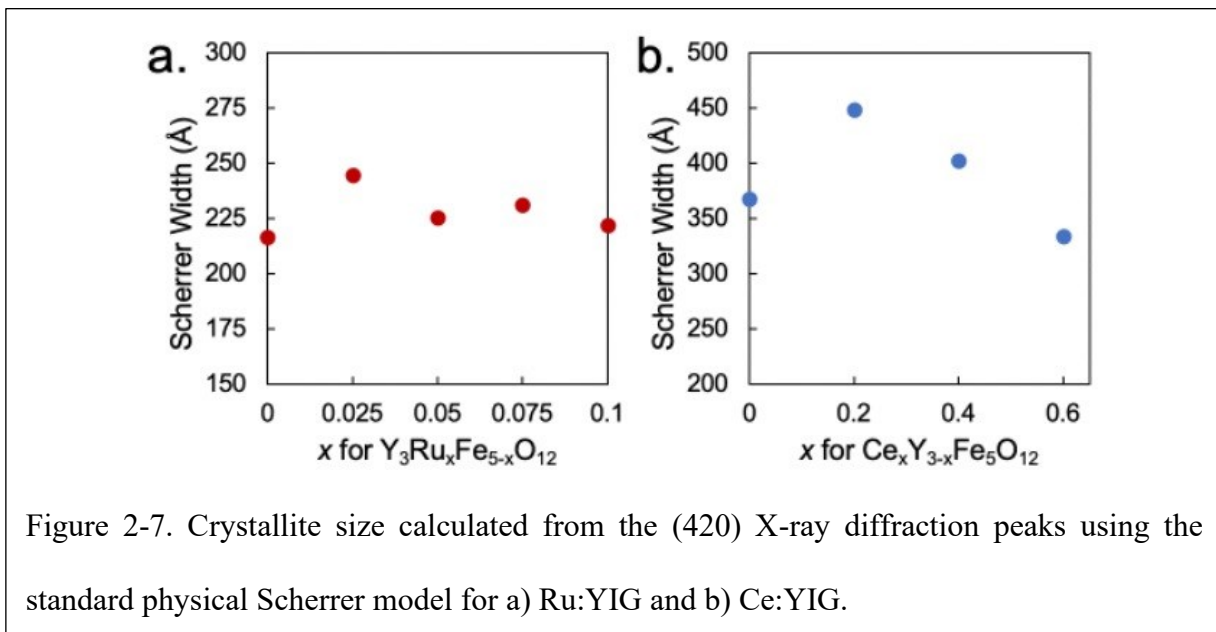
Figure 2-7. Crystallite size calculated from the (420) X-ray diffraction peaks using the standard physical Scherrer model for a) Ru:YIG and b) Ce:YIG.

results from improved nucleation. Past this initial dopant concentration, however, crystallite size is found to decrease, likely due to increased lattice distortion with higher heteroatom content. The increase in crystallite size upon addition of a small amount of dopant in both Ru:YIG and Ce:YIG is likely the cause of reduced inhomogeneous line broadening due to reduced magnon scattering off of grain boundaries.[60,61] This is followed by increased inhomogeneous line broadening as the grain size decreases at higher dopant concentration again due to magnon scattering off of the now increased number of grain boundaries.

Interestingly, the Ru:YIG samples also showed a decrease in *intrinsic* broadening at small dopant concentrations. It has been proposed by Kittel that if the damping on one sublattice (i.e. the dopant sublattice) is much larger than on the other, undoped sublattice, that the Landau Lifshitz model can be manipulated to describe the homogeneous linewidth of doped garnets as being:

$$\Delta H/H \cong \gamma_A/\alpha_B M_A \, , \qquad\qquad (3)$$

where $\Delta H/H$ is the homogenous linewidth, γ_A is the gyromagnetic ratio of the undoped magnetic sublattice, α_B is the damping of the dopant sublattice, and M_A is the saturation magnetization of the iron sublattice.[66,67] This means that based on the Kittel model, if magnetic damping at the dopant site greatly outweighs the damping of the other sublattice, magnetic loss is actually expected to *decrease* at low dopant concentration. Therefore, it can be assumed that at low dopant concentrations in Ru:YIG, the magnetic damping on the dopant site is high enough relative to the undoped sublattice to follow Kittel's model for substituted garnets. At higher dopant concentrations, such as the range investigated for Ce:YIG, the effective damping at both sites to be comparable enough to deviate from the Kittel model. This would result in magnetic loss

increasing as a function of dopant concentration as would be expected for substitution of heavier elements with high spin orbit coupling.

This work thus demonstrates that there is an ideal doping regime in YIG films deposited with sol-gel methods, where dopant concentration can be maximized while not contributing to the intrinsic magnetic loss of the material. At low enough dopant concentrations, the crystallite size can be slightly enlarged, reducing inhomogeneous line broadening from magnon scattering off of grain boundaries. Additionally, as modeled by Kittel, YIG can be doped in a way where damping also decreases. Thus, YIG can be doped such that the magnetic loss *decreases* while increasing spin-orbit coupling, a crucial parameter to macroscopic material properties such as magnetostriction. It can therefore be extrapolated that an optimal doping regime can be reached, where dopant concentration is maximized while not adding additional magnetic loss. Therefore, it is important to carefully evaluate losses over a broad range of dopant concentration in designing new low loss magnetic materials for spintronic applications.

CONCLUSIONS.

In conclusion, we have successfully used sol-gel methods to synthesize YIG films doped with both cerium and ruthenium. We have found that the films retain the YIG crystal structure up to a dopant stoichiometry of $Y_3Ru_{0.1}Fe_{4.9}O_{12}$ and $Ce_{0.75}Y_{2.25}Fe_5O_{12}$. Static magnetic properties are in good agreement with the literature for both Ru:YIG and Ce:YIG. Stripline FMR was then used to look at magnetic loss as dopant concentration increased. It was found that while the total magnetic loss was high compared to epitaxial and single crystal YIG, the losses were mostly attributed to inhomogeneous line broadening, and not Gilbert damping. This shows that these dopants may be useful for tuning other magnetic properties like magnetostriction and Faraday

rotation if the inhomogeneous losses are lowered. Moreover, it was found at low enough dopant concentrations, magnetic loss actually *decreases* with the addition of dopant (as predicted by Kittel). Thus, there exists a critical dopant concentration where YIG can be doped with sol gel methods, without increasing intrinsic magnetic losses.

CHAPTER 3.

Strain Transfer in porous multiferroic composites of CoFe$_2$O$_4$ and PbZr$_x$Ti$_{1-x}$O$_3$

Chapter 3 describes strain transfer in mesoporous multiferroic nanocomposites of cobalt ferrite and lead zirconate titanate, where high-angular resolution X-ray diffraction was used to measure strain in the ferroelectric and strain transfer to the magnetic material.

This chapter was reproduced from Buditama, A.N.; Fitzell, K.; Chien, D.; **Karaba, C. T**; Patel, S.K.; Kang, H.; Chang, J.P.; Tolbert, S.H. "Strain Transfer in porous multiferroic composites of CoFe$_2$O$_4$ and PbZr$_x$Ti$_{1-x}$O$_3$". *J. Appl. Phys.* **2023**, *133*, 014102, with the permission of AIP Publishing.

Strain Transfer in Porous Multiferroic Composites of CoFe₂O₄ and PbZrₓTi₁₋ₓO₃

Abraham N. Buditama,[1] Kevin Fitzell,[2] Diana Chien,[2] C. Ty Karaba,[1] Shreya K. Patel,[1] Hye Yeon Kang,[1] Jane P. Chang,[2,3,4*] and Sarah H. Tolbert[1,3,4,*]

ABSTRACT.

This manuscript examines the mechanism of strain-coupling in a multiferroic composite of mesoporous cobalt ferrite (CFO), conformally filled with lead zirconate titanate (PZT). We find that when the composites are electrically poled, remanent strain from the piezoelectric PZT layer can be transferred to the magnetostrictive CFO layer. X-ray diffraction shows that this strain transfer is greatest in the most porous samples, in agreement with magnetometry measurements, which show the greatest change in sample saturation magnetization in the most porous samples. Strain analysis shows that porosity both accommodates greater lattice strain and mitigates the effects of substrate clamping in thin film strain-coupled composites.

MANUSCRIPT.

Multiferroics are materials that simultaneously exhibit more than one ferroic order parameter such as ferromagnetism or ferroelectricity; they are of interest because of their potential applications in a wide range of nanoscale devices.[132–70] In particular, magnetoelectric multiferroic materials couple a magnetic and an electric polarization, but single-phase materials that show this property at room temperature are rare.[68,69,71–74] Composite materials, however, offer another route to magnetoelectric behavior. Such materials generally use strain-coupling and consist of layers of piezoelectric and magnetostrictive materials. As an electric field is applied to the composite, the

piezoelectric is strained, and this strain is transferred to the magnetostrictive material, which in turn affects the magnetization. This coupling allows the magnetization to be controlled by applied electric fields, and vice versa.[75–83] Because this technique requires intimate coupling between the two phases, numerous synthetic methods and architectures of strain-coupled multiferroics have been investigated in the literature, including sequentially deposited two-dimensional stacks, spontaneously phase-separated nanopillar arrays, and other three-dimensional arrangements.[77,78,87–94,79–86]

We have recently shown that porosity is an important control parameter in the synthesis of multiferroic composites.[83] In our previous work, a mesoporous, magnetostrictive cobalt ferrite ($CoFe_2O_4$ or CFO) film was filled using atomic layer deposition (ALD) with piezoelectric lead zirconate titanate ($PbZr_xTi_{1-x}O_3$ or PZT). The result was an interconnected, three-dimensional network containing both CFO and PZT. The final porosity in such a composite can be controlled by the initial pore size, which is determined by the polymer template used in the synthesis of the initial mesoporous CFO, and the thickness of the deposited PZT layer. Our results showed that the final composite porosity was correlated to a change in magnetic saturation that could be achieved upon electrical poling. It was hypothesized that this correlation was due to a link between porosity and mechanical flexibility of the composite, but no direct evidence for that hypothesis was obtained. Here, we examine the mechanism of magnetoelectricity in these thin film composites by depositing a range of thicknesses of PZT in the mesoporous CFO framework and measuring the resultant voltage-dependent strain in the CFO framework.

The mesoporous CFO framework was synthesized using block copolymer–templating of sol-gel films, a technique that has been used to produce a wide range of metal oxide materials of varying nanoarchitectures.[95–104] The CFO sol was templated with an amphiphilic diblock

copolymer that forms micelles in solution. As the solution is deposited, the micelles self-assemble into periodic structures within the film. Upon pyrolysis, the polymer is removed, leaving a stable porous network of CFO.

This porous film is then conformally coated with PZT using ALD, which grants uniformity over the entire structure because this technique obtains layer-by-layer growth through a self-limiting surface reaction. Alternating pulses of gaseous precursors completely saturate all available surface sites, allowing conformal deposition over the entire porous network. ALD also allows for fine control over the thickness deposited, and thus over the final porosity of the composite material. This method thus provides new functionality compared to composites in the literature, which thus far have been dense structures that lack porosity. Here we aim to use high-resolution X-ray diffraction on films as a function of *ex situ* poling field to explore the mechanisms of strain coupling in this porous composite.

Synthetic details for both CFO and PZT have been discussed previously.[83,95,105] Briefly, poly((ethylene-*co*-propylene)-*block*-poly-(ethylene oxide) with a mass ratio of PEP(3900)-*b*-PEO(4000) was used to template a sol based on nitrate salts of Co and Fe. Films were dip-coated onto silicon wafers in a humidity-controlled chamber set to 10–20% relative humidity. The withdrawal rate was usually 2 mm/s but can be varied, depending on desired thickness. To form rigid inorganic/organic structures, the films were calcined in air at 80°C for 6 hours, at 130°C for 8 hours, and at 180°C for 6 hours for a total heating time of 24 h including temperature ramps. Once calcined, films were annealed at 550 °C with a 10 °C/min ramp for 5 minutes.

PZT was deposited via ALD using $Pb(TMHD)_2$, $Ti(O-i-Pr)_2(TMHD)_2$, and $Zr(TMHD)_4$ as precursors. PZT was deposited at no more than 180 °C in an amorphous form and then crystalized

into tetragonal PZT by rapid thermal annealing at 700 °C under oxygen for one minute. Here, the PZT layer thicknesses range from 3 nm to 10 nm.

The morphology and thickness of the nanocomposites was confirmed using a JEOL JSM-6700F field-emission scanning electron microscopy (FE-SEM). Ellipsometric porosimetry (EP) was performed on a Semilab PS-1100 in the spectral range of 1.24 eV to 4.5 eV. A UV-vis CCD detector adapted to a grating spectrograph analyzes the signals reflected by the sample from a 75 W Hamamatsu Xe lamp. Toluene was used as the adsorbent and the EP analysis was performed using the associated SEA software. Angular-dependent X-ray diffraction (XRD) was collected at the Stanford Synchrotron Radiation Laboratory (SSRL) using beamline 7-2 at wavelengths $\lambda =$ 0.9919 Å and 1.0332 Å. Magnetic measurements were carried out on a Quantum Design MPMS 5T SQUID magnetometer with RSO detection.

Because our previous work indicated the importance of residual porosity in multiferroic composites, we first characterized the porosity of the composites using ellipsometric porosimetry (EP). EP adsorption/desorption curves for samples with various PZT layers (Figure 1a) show that as thicker PZT layers are deposited, less porosity is observed. The samples with 0 nm and 3 nm of PZT show a distinct type IV isotherm, which signifies an interconnected porous network.
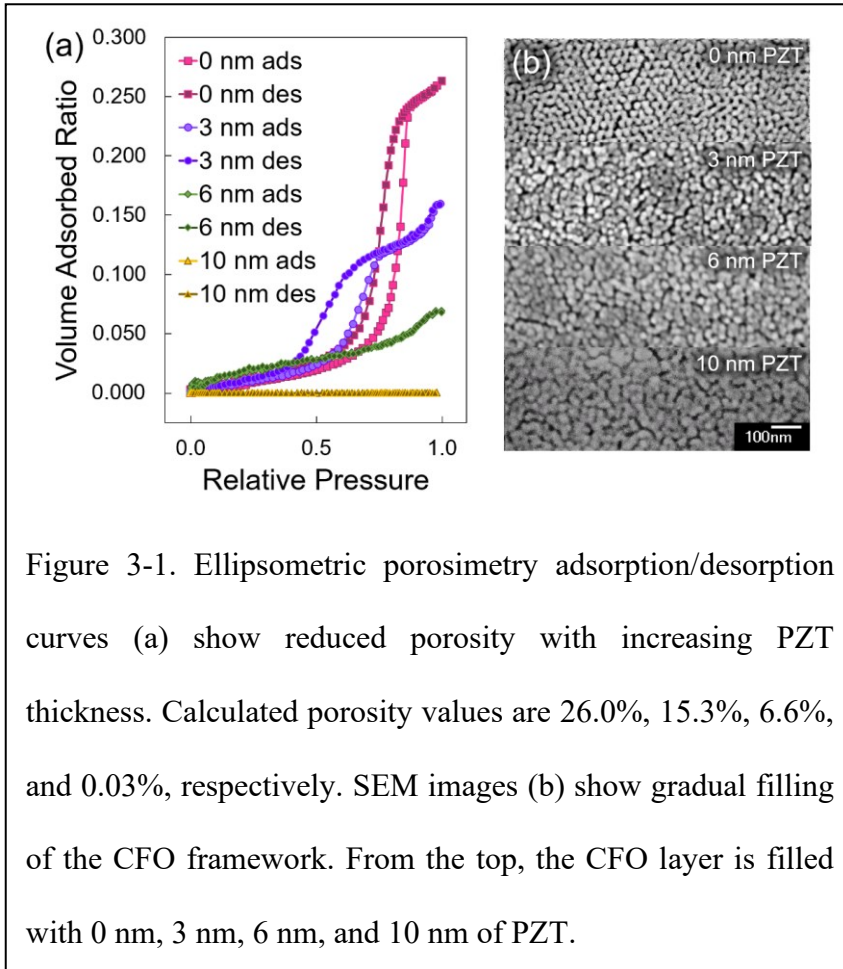
Figure 3-1. Ellipsometric porosimetry adsorption/desorption curves (a) show reduced porosity with increasing PZT thickness. Calculated porosity values are 26.0%, 15.3%, 6.6%, and 0.03%, respectively. SEM images (b) show gradual filling of the CFO framework. From the top, the CFO layer is filled with 0 nm, 3 nm, 6 nm, and 10 nm of PZT.

The calculated porosity values are 26.0% for the 0 nm PZT sample, 15.3% for 3 nm, 6.6% for 6 nm, and 0.03% for 10 nm. The PZT in these as deposited films are amorphous, but previous work[83] has shown that the PZT can be crystallized to the ferroelectric tetragonal phase. We find that redistribution of the PZT in the pores can block the small necks in the structure, impeding toluene access to the pores. As a result, SEM was used to characterize the samples after crystallization. SEM images of the samples with crystallized PZT layers (Figure 1b), from top to bottom, show reduced porosity as thicker PZT layers are deposited. The unfilled CFO framework exhibits ordered porosity, which is distorted by grain growth upon annealing of the PZT layer. For this reason, the 10 nm sample still appears to be somewhat porous by SEM, even though access into the porous interior is stopped by pore necks that had been completely stoppered by PZT, as seen from the EP adsorption/desorption curves.

To determine the magnetoelectric coupling of these thin film composites, they were electrically poled *ex situ* with the electric field applied
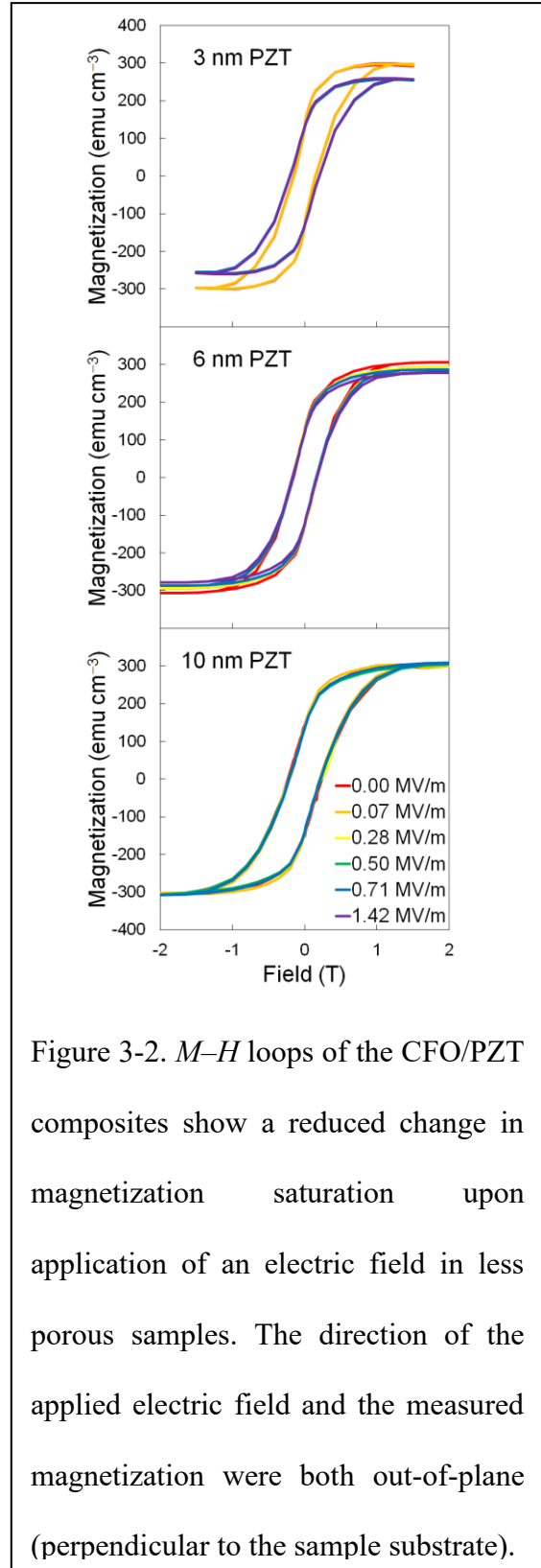
Figure 3-2. *M–H* loops of the CFO/PZT composites show a reduced change in magnetization saturation upon application of an electric field in less porous samples. The direction of the applied electric field and the measured magnetization were both out-of-plane (perpendicular to the sample substrate).

perpendicular to the sample surface (henceforth referred to as out-of-plane). The films were covered with a 13 μm polyvinylidene chloride spacer and physically sandwiched between two Al electrodes 1.28 cm in diameter. The nanocomposite was electrically poled for 10 min with applied electric fields ranging from 0 MV m^{-1} to 1.42 MV m^{-1}. As such, the strains and polarizations explored in this paper are remanent ones. While it is true that much of the strain and polarization will be lost upon removal of the applied field, the remanent polarization stabilizes within milliseconds and can be assumed to be constant throughout the measurement.[106,107]

Magnetization measurements show a decrease in out-of-plane saturation magnetization upon electrical poling, which is correlated with porosity of the composite (Figure 2). The sample with the thinnest PZT layer shows the largest change in saturation magnetization, and the sample with the thickest PZT shows hardly any change. Because polarization in ultrathin PZT is known to decrease with thickness,[108,109] this trend is likely due to the mechanical properties of the porous composite, rather than any favorable change in the PZT itself. The films with the thinnest PZT are also the ones with the highest porosity, and therefore the greatest mechanical flexibility, as pore flexion accommodates significant strain changes in the material.[95,96,110]

The role of porosity in magnetoelectric coupling is corroborated by strain analysis of the CFO layer. Synchrotron high-resolution XRD was used to probe the differences in both out-of-plane and in-plane (parallel to the substrate) lattice spacings. The CFO{311} and PZT{200} peaks were relatively well resolved and were treated as representative of overall strain changes in both materials. Because these films consist of polycrystalline CFO and PZT with no preferred orientation with respect to the substrate, any lattice plane can be used to report on the overall strain state of the material. As shown in Figure 3 and expected based on the magnetization data, the CFO{311} out-of-plane lattice spacing increased upon *ex situ* electrical poling, and the magnitude

33

of the change was directly correlated to the porosity of the composite. As the porosity decreased, the strain transferred upon electrical poling also decreased (Figure 3). CFO exhibits negative magnetostriction, and so out-of-plane tension directly corresponds to the reduced magnitude of change in out-of-plane magnetization saturation.
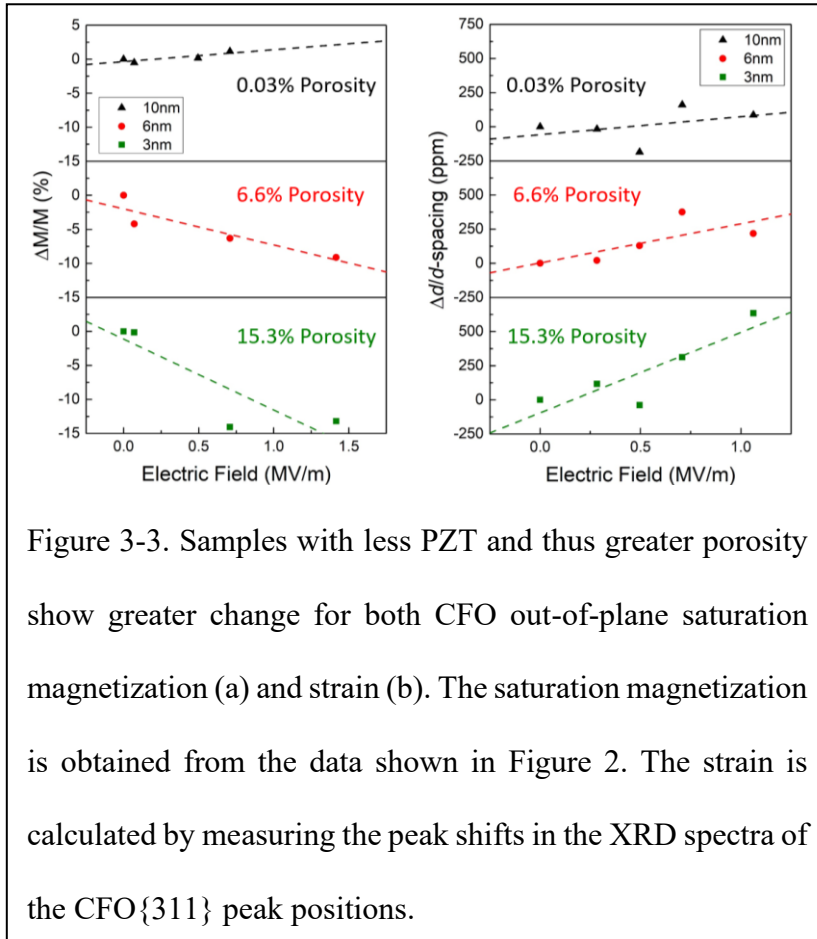
Figure 3-3. Samples with less PZT and thus greater porosity show greater change for both CFO out-of-plane saturation magnetization (a) and strain (b). The saturation magnetization is obtained from the data shown in Figure 2. The strain is calculated by measuring the peak shifts in the XRD spectra of the CFO{311} peak positions.

Even though CFO is not a piezoelectric, it is strain-coupled to one, and so we can calculate the strains when $1\,\mathrm{MV\,m^{-1}}$ has been applied and then removed from the sample. While this strain is not a real piezoelectric coefficient, it relates a remanent strain to an *ex situ* electric field, and so we give it the symbol d'_{33}.

Values of d'_{33} ranging from $d'_{33} = 590 \times 10^{-12}\,\mathrm{m\,V^{-1}}$ for the composite with the highest porosity (3 nm PZT), to $d'_{33} = 130 \times 10^{-12}\,\mathrm{m\,V^{-1}}$ for the composite with lowest porosity (10 nm PZT), which is comparable to true piezoelectric coefficients of PZT.[111–113] These values demonstrate more than a fourfold reduction in strain transferred when porosity is removed from the sample. Again, we emphasize that these calculated values are not true piezoelectric coefficients because they relate the remanent strain to an *ex situ* applied field instead of the instantaneous strain to an *in situ* field; the instantaneous piezoelectric coefficient should be higher indeed.

34

No significant change upon electrical poling was found in the in-plane saturation magnetization nor in the CFO in-plane strain. The CFO framework is covalently bound to the substrate and is unable to move in plane because of substrate clamping. Because its strain is unchanged, the CFO in-plane magnetization is also unchanged. However, the PZT layer is deposited onto the CFO framework itself, and as such is not constrained by the substrate. As the PZT deforms due to the out-of-plane electric field, strain can be expressed as out-of-plane tension or in-plane compression. This strain is transferred to the clamped CFO framework and can be expressed only as the aforementioned out-of-plane tension. Interestingly, analysis of PZT strain reveals contribution from both in-plane compression and out-of-plane tension. Similar d' coefficients calculated for PZT show comparable strains to the CFO, but with more noise, because the PZT layer is mere nanometers thin and thus diffracted intensity is weaker. The greatest PZT strains are in the most porous sample (3 nm PZT) and are shown in Figure 4. The data shows changes in both in-plane and out-of-plane lattice constants, and demonstrate that the PZT is not at all substrate clamped. The strains are calculated to be $d'_{31} = -670 \times 10^{-12}$ m V^{-1} in-plane and $d'_{33} = 130 \times 10^{-12}$ m V^{-1} out-of-plane. These values are comparable to that of the CFO, suggesting that much of the strain had indeed been transferred.

Figure 3-4. The magnitudes of the in-plane and out-of-plane PZT strains are comparable to those of the CFO. PZT strains are calculated by measuring the shifts in the XRD spectra of the PZT{200} peak positions.
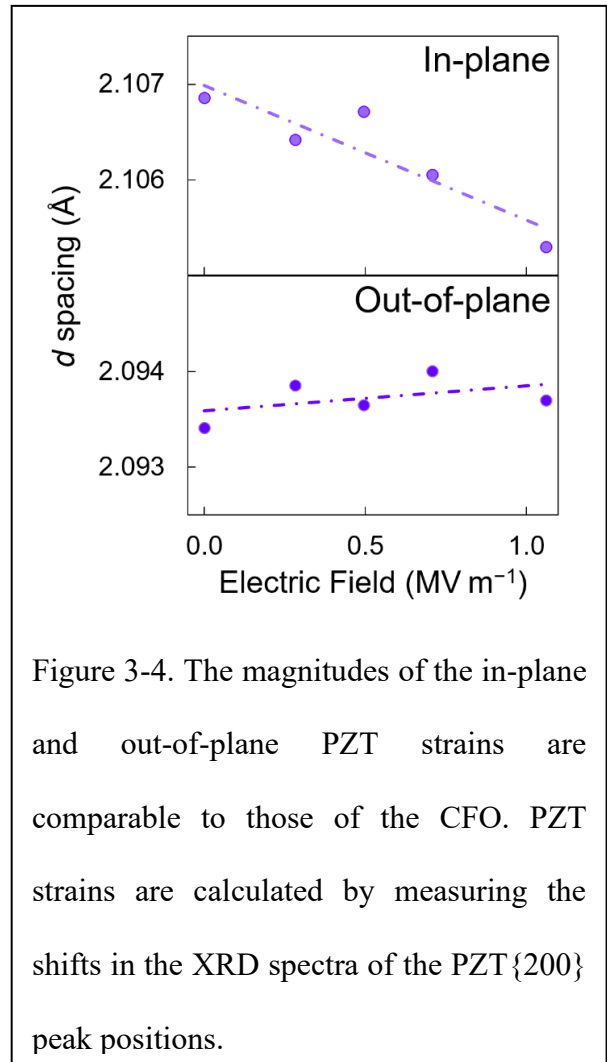
Thus, from strain analysis of this free PZT layer, we see that three-dimensional porosity has an advantage over traditional two-dimensional structures where multiple layers are clamped together and to the substrate. In a three-dimensional structure like this one, the pore-filled material can remain unclamped if sufficient residual porosity is retained.

Overall, these experiments have allowed us to explore the mechanism of strain-coupling in porous magnetoelectric CFO/PZT composites. These thin films are composed of a templated mesoporous CFO framework, which is subsequently filled by ALD PZT of varying thicknesses. As the samples are electrically poled out-of-plane, X-ray diffraction shows that the piezoelectric PZT layer may exhibit both out-of-plane tension and in-plane compression. This strain is transferred to the magnetostrictive CFO layer, which results in decreased out-of-plane saturation magnetization as measured by SQUID magnetometry. The strain transfer is greatest in samples with the greatest porosity, as pore flexion accommodates greater strains in the material. This porous architecture thus offers not only greater mechanical flexibility than traditional composite architectures, but also mitigates the effects of substrate clamping for the ALD layer. Perhaps more importantly, the observation of in-plane compression in what could have been a clamped PZT layer provides insight into the use of porosity in the design of future porous multiferroic composites.

ACKNOWLEDGEMENTS.

CHAPTER 4.

Increased Magnetoelectric Coupling in Porous Composites of CoFe2O4 and BiFeO3 with Residual Porosity

Chapter 3 describes mesoporous multiferroic nanocomposites of cobalt ferrite and bismuth ferrite, which demonstrates that porosity can allow for more efficient strain transfer and thus high magnetoelectric coupling.

This chapter was reprinted with permission from Patel, S.K.; Karaba, C.T.; Robertson, D.D.; Chang, J.; Fitzell, K.; Salamat, C.Z.; Chang, J.P.; Tolbert, S.H. "Increased Magnetoelectric Coupling in Porous Composites of $CoFe_2O_4$ and $BiFeO_3$ with Residual Porosity" *ACS Appl. Nano Mater.* **2023**, *6*, 4141-4150. Copyright 2023, American Chemical Society.

A reprint of the supporting information is given in Appendix B.

Increased Magnetoelectric Coupling in Porous Nanocomposites of CoFe$_2$O$_4$ and BiFeO$_3$ with Residual Porosity for Switchable Magnetic Devices

Shreya K. Patel,[1‡] C. Ty Karaba, [1‡] Daniel D. Robertson,[1] Jeffrey Chang,[2] Kevin Fitzell,[2]

Charlene Z. Salamat,[1] Jane P. Chang,[2,3,4] Sarah H. Tolbert[1,3,4,*]

ABSTRACT.

In this work, multiferroic thin film nanocomposites were synthesized by coating the inside of mesoporous, cobalt ferrite (CoFe$_2$O$_4$, or CFO) with varying thicknesses of piezoelectric bismuth ferrite (BiFeO3, or BFO) grown by atomic layer deposition (ALD). Since ALD allows for precise control of the BFO layer thickness, the amount of residual porosity inside the pores can be controlled. Upon electrical poling, the piezoelectric BFO strains to be under out-of-plane tension, and since BFO is covalently bound to CFO, this tensile stress is transferred from BFO to CFO. CFO is a negative magnetostrictive material, meaning its magnetization should decrease in the direction of tension. This decrease in magnetization was observed in out-of-plane magnetometry experiments. Interestingly, the magnetization changes were found to be largest in the samples with the most residual porosity, despite the fact that they contained the smallest volume of BFO. Indeed, while the fully-filled samples had a similar magnetoelectric coefficient to other dense nanostructured BFO-CFO composites reported in the literature, composites with the most residual porosity showed an exceptionally large converse magnetoelectric coefficient of 1.2×10^{-6} s·m^{-1}, an order of magnitude higher than dense composites. Strain transfer was confirmed using high-resolution X-ray diffraction. Samples with more residual porosity showed larger strain changes, corroborating the magnetization data. This suggests that magnetoelectric coupling can be optimized by engineering residual porosity into multiferroic composites. Such systems have

profound effects for a broad range of switchable magnetic devices, particularly in the microwave and spintronic space.

INTRODUCTION.

Conventional electromagnets use *current* to control magnetism, but for the development of nanoscale devices, it is crucial to be able to control magnetization with *voltage* to mitigate Ohmic losses.[114] Multiferroics, materials that exhibit multiple forms of ferroic ordering (including ferroelectricity, ferromagnetism, and ferroelasticity), can enable voltage-control of magnetism for such devices.[68,71] Because there are only a few known room temperature multiferroic materials, strain-mediated multiferroic composites have been developed to address the demand for voltage control of magnetism.[72,73] Such composites couple a piezoelectric material, which strains in response to an electric field, to a magnetostrictive magnetic material, which changes magnetization as its magnetic domains rotate in response to strain. In the composite, when the piezoelectric is electrically poled, the magnetostrictive material will also be strained, which changes its magnetization. The field of strain-mediated magnetoelectric composites has flourished in the past few decades, with a wide range of bulk[115] and thin film[1,116–119] systems showing large magnetization changes. Indeed, these materials have already been successfully integrated into real devices, especially in the microwave space.[94,120,121] For example, the size of traditional antenna devices is dictated by its signal wavelength, which makes downsizing very difficult. However, multiferroic antenna devices offer a unique design solution allowing conventional antenna devices to be downsized by orders of magnitude.[3,4,122] These devices utilize strain mediated composites to read/transmit signals. Out-of-plane strain in the magnetostrictive material creates an acoustic wave in response to the incoming electromagnetic wave. This magnetostrictive material is coupled to a

piezoelectric, which can convert the acoustic wave into a voltage that is usable as an electric signal. Thus, the multiferroic antenna is able to convert an electromagnetic signal into a readable voltage, without the same size constraints as traditional antenna devices.

While this class of composite materials has already had a large impact in the field, the efficacy of strain-mediated multiferroics can be greatly enhanced with nanoscale architecture. Increased interfacial surface area between the magnetostrictive material and the piezoelectric materials can result in greater magnetoelectric coupling. Additionally, nanostructured architecture offers an additional advantage over bulk or bilayer films, since they can reduce the effect of substrate clamping, or the prevention of in-plane strain due to covalent binding of a thin film to the substrate. Thus, many nanoscale architectures have been employed in magnetoelectric multiferroic coupling, such as in co-deposited systems with spontaneous phase separation[88,123,124], multilayer thin films[125–127], solution-based systems of nanoparticles in a matrix[128–130], polymer assisted deposition[131,132], and core-shell nanoparticle systems[90,133,134].

Although previous work has shown many methods of maximizing the magnetostrictive-piezoelectric interface, the strain in dense nanostructured materials is still limited by clamping at the interfaces.[123,135] In other words, if there is no room for the materials to flex within the composite, that limits the maximum strain that can be achieved. In this work, we employ a unique strategy in strain-mediated multiferroic systems – engineering *residual porosity* into the composites. This poses a unique advantage over, say, epitaxial multiferroic composites. In epitaxial composites, there is maximum contact between the ferroelectric and the magnetostrictive materials. This results in very high strain transfer between the two materials and has thus resulted in a wide range of systems that exhibit large magnetoelectric coupling.[84,136–139] However, one of the primary limitations in epitaxial films is that they suffer from substrate clamping – the thin

composite film is still bound by the lattice constant of the substrate that the films are grown on. Porosity helps alleviate substrate clamping because porous structures are more mechanically flexible than their dense counterparts, which will make them easier to strain in magnetoelectric composites.[140–142] This theory was reinforced by previously performed finite element modeling on similar multiferroic composites with residual porosity.[143] We found that there are two competing effects in the overall strain response from the porous composite – strain from the mass fraction of piezoelectric in the composite, and the increase in mechanical flexibility in the composite from the porosity. It was found that, in piezoelectric layers of the same thickness as those used in this work, that the increase in strain from increased mechanical flexibility outweighed the effect from larger mass fractions of the piezoelectric. Thus, the porosity makes the composite more mechanically flexible than epitaxial films, which makes them easier to strain.

Recently, we were able to demonstrate that residual porosity could be engineered into multiferroic composites.[83,143,144] We developed the nanocomposite architecture by filling a mesoporous, magnetostrictive template with a piezoelectric material. Here, we specifically chose cobalt ferrite ($CoFe_2O_4$, or CFO) as our magnetic material for its large magnetostriction value.[145] To make porous CFO, block copolymer templating of a sol gel synthesis with Co and Fe precursors was used.[95] In sol gel chemistry, metal precursors are dissolved in a 'sol', and then undergo condensation reactions to form a metal-oxide polymer matrix known as a gel. Amphiphilic block copolymers are added to the sol, which self-assemble into micelles. The gel can then be solution processed to make thin films on a variety of substrates. Here, the templated gel was spin-coated onto platinized silicon substrates (Pt (100 nm)/Ti (5 nm)/SiO_2 (~ 1 μm)/Si). Upon annealing, the CFO is crystallized into polycrystalline thin films and the polymer micelles are pyrolyzed, leaving

pores behind in the structure. This technique is robust and has been used to make a wide range of porous metal oxide materials.[97,146,147]

With the CFO framework in place, we then use atomic layer deposition (ALD) to coat the inside of the pores. ALD is a deposition method where metal precursors are volatilized and then react with available surface sites. Since ALD is a gas phase deposition, precursors can easily pass through the pores and bind to the surface sites inside the CFO framework. ALD is also known as a conformal technique, meaning that it is highly capable of homogeneously coating extremely high aspect ratio structures; this should allow for uniform deposition of BFO throughout our porous CFO structures. Importantly, because the number of surface sites are finite, the reaction is self-limiting. Therefore, ALD provides precise control of film thickness and stoichiometry, on the near-angstrom level. The residual porosity can thus be carefully controlled through the ALD layer thickness. Once deposited, the amorphous ALD films were crystallized using rapid thermal annealing (RTA) under oxygen for 1 minute at 700 °C.

In our previous work, we were able to synthesize CFO using block copolymer templating, as described above, that was fill with ALD-grown lead zirconate titanate ($PbZr0_{0.48}Ti_{0.52}O_3$, or PZT).[83,105] Here, we hypothesized that upon out-of-plane electrical poling, that the PZT would strain to be under out-of-plane tension and in-plane compression. Since the CFO is covalently bound to PZT, and thus is strain-coupled to it, we expected it to also be under out-of-plane tension and in-plane compression. Since CFO is a negative magnetostrictive material, its magnetization should decrease in the direction of tension. Thus, in these composites, we were able to measure the out-of-plane tensile strain change with high-resolution X-ray diffraction and observe the corresponding decrease in magnetization with magnetometry experiments in poled samples. The PZT layer thickness was varied, leaving composites with a range of residual porosity. That was

the first system where we found that increasing residual porosity in these samples could lead to larger changes in magnetization. Magnetization changes correlated well to the strain changes, as probed by high-resolution X-ray diffraction, with samples that showed larger residual porosity also showing increased strain change upon application of an external electric field.[143,144] Additionally, finite element modeling performed on this system confirms that the driving reason for increased strain is because the porous composite is less stiff, which effectively competes with the loss of piezoelectric mass fraction. The non-monotonic strain response was modeled to account for these two competing effects and was found to match the experimental strain values obtained from high-resolution diffraction in the CFO-PZT composites. While the dependence on porosity was clear from that work, the absolute magnetization change was fairly small, since the piezoelectricity in PZT is very sensitive to thickness.

In this work, we build upon those previous results and show both that this phenomenon can be generalized to multiple piezoelectric materials and that the performance can be optimized by selecting materials with ideal properties. As described above, magnetization and strain changes in the CFO/PZT composites were the largest in the thinnest PZT coated samples. However, the piezoelectricity of PZT becomes unstable below a certain thickness, greatly reducing its d_{33}, or piezoelectric coefficient (longitudinal strain change for a given electric field).[148–150] Bismuth ferrite ($BiFeO_3$, or BFO), however, maintains higher d_{33} values than PZT in the ultrathin (< 5 nm) regime.[105,151,152] Thus, while PZT has a higher d_{33} than BFO in the bulk, BFO is expected to have a higher d_{33} in ultrathin films, meaning the magnetization changes are also expected to be larger. In this work, we thus focus on CFO/BFO composites, and show that the trend of increasing multiferroic coupling with increasing porosity is robust across materials systems. We also show dramatically increased performance in this more optimized materials system.

EXPERIMENTAL SECTION.

Synthesis of CFO-BFO Nanocomposite. Synthesis of porous CFO[95,144,153] and ALD deposition of BFO[151,152] have been discussed previously. A schematic of the synthesis can be found in Fig. 1(a). For the porous CFO template, a sol gel synthesis containing stoichiometric amounts of Co and Fe precursors (in this work, $Fe(NO_3)_3 \cdot 9H_2O$(0.31 g) and $Co(NO_3)_2$ $6H_2O$ (0.11 g)) were dissolved in 1 mL of 2-methoxyethanol, 1 mL of ethanol, and 20 μL of glacial acetic acid. Once dissolved, the sol was templated with poly((butadiene)(5500)-*block*-poly-(ethylene oxide)(7500)) (Polymer Source Inc, catalog number P2952_BdEO). In this work, a templating solution containing 40 mg of the block copolymer was added to 1 mL of ethanol, then was stirred, and heated on a 50 °C hot plate to dissolve the polymer for approximately an hour. Once homogenous, the templating solution was added to the sol.

Films were then dip-coated from this solution onto silicon with a platinum back electrode (Ti(5 nm)/Pt (100) deposited on thermally oxidized silicon) under 10-20% humidity. Films were calcined in air at 80 °C for 6 hours, at 130 °C for 8 hours, and at 180 °C for 6 hours. Once calcined, films were crystallized through annealing overnight at 550 °C with a 10 °C/min ramp and cool.

For ALD BFO, metal alkoxide precursors β-diketonate, tris(2,2,6,6-tetramethyl-3,5-heptanedionato) iron(III) (Fe(TMHD)$_3$), and Bi(TMHD)$_3$ were co-reacted and oxidized with radicals, forming amorphous films. It should be noted that further heating beyond the temperature required for crystallization (550 °C) can warp the pore network, so we limited the crystallization time to 1 minute using an RTA process to maintain the ordered pore structure. Therefore, once

deposited, ALD BFO was crystallized through rapid thermal annealing at 700 °C under oxygen for 1 minute in a tube furnace.

Instrumentation. Ellipsometric porosimetry (EP) was performed using a Semilab PS-1100 in the spectral range of 1.0 eV to 5.0 eV. Toluene was used as the adsorbent and the EP analysis was performed using SEA software. Imaging and energy-dispersive X-ray spectroscopy on the nanocomposites was confirmed using a JEOL JSM-6700F field-emission scanning electron microscopy (FE-SEM). XPS was performed on a Kratos Axis Ultra DLD spectrometer with a monochromatic Al Kα radiation source. A charge neutralizer filament was used to prevent the charging of the BFO/CFO films. Both spectra were calibrated using the adventitious Carbon 1s peak. Analysis was performed on CASA XPS Software using the CASA XPS Library. S/TEM imaging was performed using a FEI Titan scanning transmission electron microscope operated at an accelerating voltage of 300 kV. This instrument is equipped with Oxford X-MaxTEM 100 N TLE Windowless silicon drift detector (SDD) 100 mm 2 EDS and a Gatan Ultrascan 2 K × 2 K charge-coupled device (CCD) camera. To prepare samples, films were detached from the substrate with a razor blade, suspended in ethanol, and drop-cast onto copper grids for analysis. Grazing incidence wide angle scattering (GIWAXS) was collected at Stanford Synchrotron Radiation Laboratory (SSRL) using beamline 11-3. 2D patterns were reduced to 1D patterns using IgorPro 6.37. 1D patterns were then compared to JCPDS reference cards #00-001-1121 (for CFO) and #00-014-0181 (for BFO) using X'Pert Highscore Plus 2.0.1. Magnetic measurements were carried out on a Quantum Design MPMS3 superconducting quantum interference device (SQuID) magnetometer. Polarization – electric field characterization was carried out on a precision RT66C Ferroelectric Tester (Radiant Technologies). For magnetoelectric coupling testing, samples were poled in between two aluminum stubs, with a dielectric spacer (12.7 μm thick) on top to prevent

shorting (see Fig. S8). The stubs were wired to an Agilent power supply connected to an amplifier. High angular resolution X-ray diffraction (XRD) was collected at SSRL using beamline 7-2 at wavelengths $\lambda = 0.886$ Å.

RESULTS AND DISCUSSION.

First, we set out to characterize the unfilled CFO framework. An SEM image showing the
morphology of the unfilled CFO template is shown in Fig. 1(b). The porosity is relatively ordered,
with pore sizes ranging from 10-13 nm. We then turned to characterize the composite with
elemental mapping. Energy-dispersive X-ray spectroscopy (EDS) was used to observe the relative

Figure 4-1. Synthesis and characterization of multiferroic nanocomposites. (a) Schematic
illustrating the synthesis of multiferroic nanocomposites with residual porosity, (b) SEM
image of unfilled, porous CFO template with pores from 10-13 nm, (c) GIWAXS 1D patterns
for the porous CFO template alone (black), 12 nm filled BFO nanocomposite (grey). Asterisks
represent likely Pt back electrode peaks.

elemental ratio between the cobalt and iron in the composite films, which show the expected 1:2 atomic ratio for CFO [Fig. S1(a-b)]. The quantification of cobalt and iron is echoed by STEM-EDS of the 6 nm composite (Fig. S2). We also used grazing incidence wide angle scattering (GIWAXS) to confirm the crystal structure of the CFO template [Fig. 1(c)]. GIWAXS confirms the porous CFO template is crystalline and has the expected Spinel crystal structure in the composite. CFO template films for all the composites was intentionally kept the same film thickness in order to keep the strain from substrate clamping the same. We note that the CFO template itself and the composite films are under some strain from the difference in thermal expansion coefficient. More discussion of the initial macrostrain state of the CFO template (Fig. S3) and the composites (Fig. S4), as well as the microstrain state of the composites (Fig. S5) can be found in the supporting information.

The thickness of the BFO layer in the composites was varied across samples, filling the pores of CFO to approximately 3 nm, 6 nm, 9 nm, 12 nm filled. First, we set out to perform elemental analysis on the resulting composites. In both composites, we see the cobalt and iron L-edges in the appropriate 1:2 atomic ratio expected for CFO. In EDS, we observe a small peak at 2.4 keV that matches the bismuth M edge energy level in both the 3 and 6 nm sample [Fig. S1(a-b)]. The bismuth fraction can be quantified for the 6 nm film [Fig. S1(b)], but the error is too large for the 3 nm sample. The quantification of bismuth, cobalt, and iron is echoed by STEM-EDS of the 6 nm composite (Fig. S2). Since the volume of BFO is so small, we turned to XPS to more clearly observe the BFO layer [Fig. S1(c)]. In the 3 nm sample, we observe the bismuth 4f, 5p, and 5d energy levels [Fig. S1(c)]. We also observe cobalt and iron, as we would expect for CFO. In the 6 nm sample, however, we only see the bismuth and iron from BFO, and no cobalt [Fig. S1(d)]. This result nicely confirms the presence of thicker surface films in the 6 nm sample, as 6 nm should

be greater than the XPS penetration depth and the CFO component of the composite should not be observable in this sample.

Following the synthesis and characterization of the composites, we then set out to characterize their morphology. As can be seen from SEM images of the filled composites, the pore diameters were found to be about 10-13 nm in unfilled CFO [Fig. 1(b)] and then gradually decrease with increased BFO layer thickness [Fig. 2(a)]. The residual porosity was determined using ellipsometric porosimetry with toluene gas vapor as the adsorbent [Fig. 2(b)].[154] The isotherms for each sample show a hysteretic response, indicating that the nanocomposites have an interconnected pore network.[155] As can be seen in the isotherms in Fig. 2(b), as the BFO layer thickness is increased, the sample porosity decreases, down to nearly 0% porosity in the fully-filled nanocomposite. This monotonic trend is what we would expect with the BFO layer thickness from
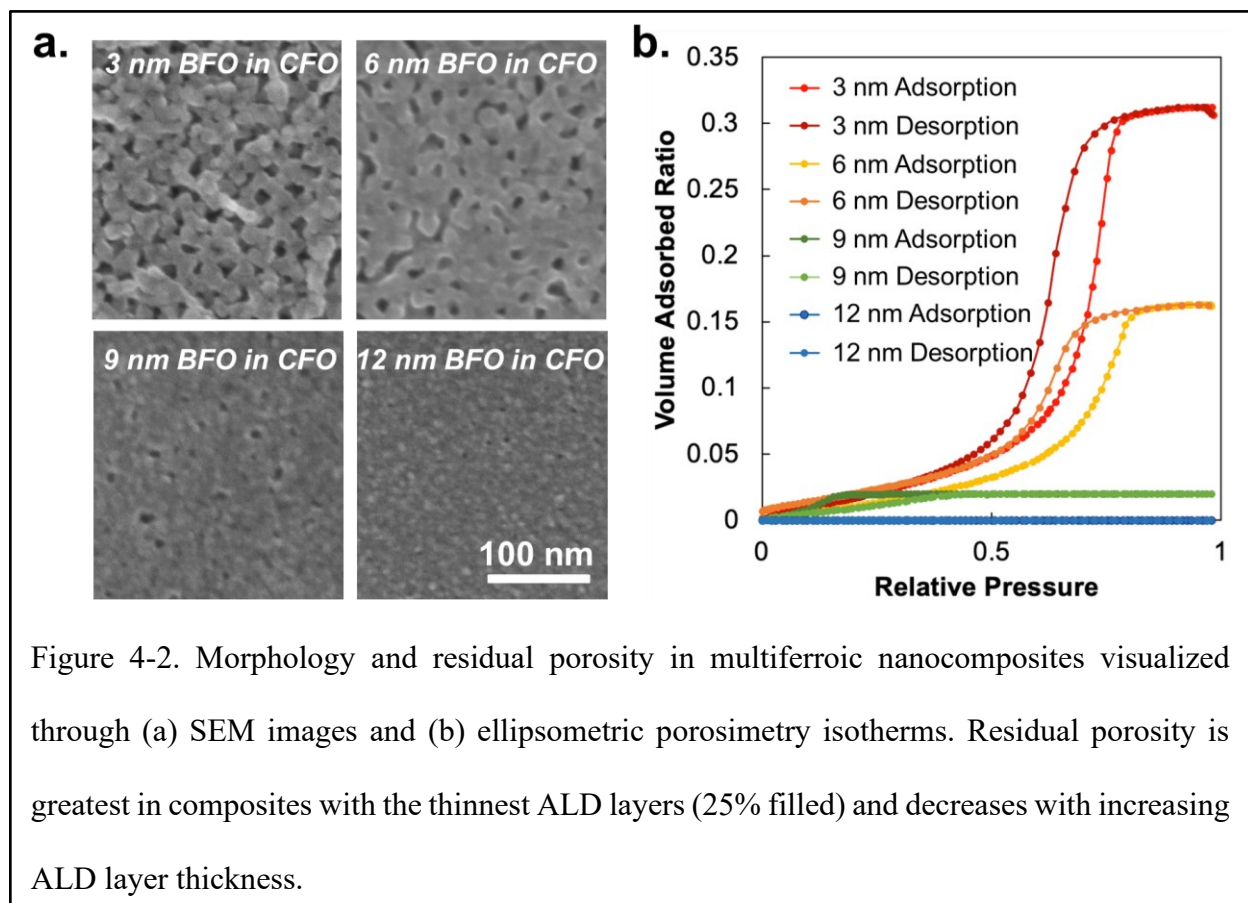
Figure 4-2. Morphology and residual porosity in multiferroic nanocomposites visualized through (a) SEM images and (b) ellipsometric porosimetry isotherms. Residual porosity is greatest in composites with the thinnest ALD layers (25% filled) and decreases with increasing ALD layer thickness.

the ALD deposition. It is important to note here that although the isotherm shows near 0% gas adsorption, it is possible that there is still some residual porosity in these samples. ALD filling can fill the pore necks, 'blocking' toluene from entering the interior of the structure. Nevertheless, it is clear from SEM and ellipsometric porosimetry that the residual porosity is very low with the thickest ALD BFO layers.

In addition to observing the morphology of the composites, we wanted to characterize the CFO/BFO distribution with STEM (Fig. 3). Bright field and High-Angle Annular Dark Field (HAADF) images both show the film with well-defined residual porosity [Fig. 3(a-b)]. We then turned to elemental mapping to see where the BFO and CFO are. Elemental mapping is done in STEM-EDS mode, which has significantly reduced resolution relative to standard STEM imaging [Fig. 3(c)]. Because both phases contain Fe, we can use the relative mapping of cobalt to see where the CFO lies, and the mapping of bismuth to see where the BFO is. As seen from the elemental mapping, the bismuth is found homogeneously distributed throughout the
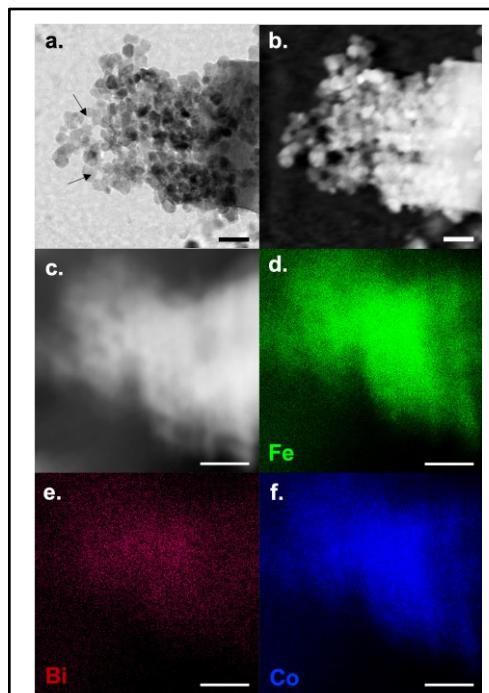
Figure 4-3. Scanning Transmission Electron Microscopy (STEM) of composite film (6 nm). Bright field images (a) and High-angle annular dark field (HAADF) (b) STEM images of the composite, showing well-defined residual porosity (c) STEM-EDS image with elemental mapping of Fe (d), Bi (e), and Co (f). Bi is spread over the entire area of the film. All scale bars are 50 nm.

network, demonstrating that BFO does, in fact, infiltrate the inside of the pores to form a uniform

coating inside the pore structure [Fig. 3(c-f)]. To see the spatial variation in Co and Bi, we plotted a quantitative elemental line scan over regions containing clear pores to visualize the BFO/CFO distribution (Fig. S6). Though the resolution is poor due to both the multilevel sample and ferroelectric nature of the sample (making them very susceptible to charging and thus drifting in electron microscopy), there is a distinct anticorrelation between the cobalt and bismuth in the line scan, with a periodicity that approximately matches the distance of one pore (10-13 nm) apart. When a Pearson correlation coefficient is calculated form the data in Fig. S6, the Bi and Co are found to be anticorrelated with a correlation coefficient of -0.4. This data thus strongly supports the picture of a CFO framework coated homogeneously by BFO.

Having characterized the material interfaces with TEM, we turned to observing the magnetic and piezoelectric properties of CFO and PZT, respectively. Since ferrimagnetism and piezoelectricity are ferroic properties, both exhibit hysteresis. First, we used superconducting quantum interference device (SQuID) magnetometry to look at the hysteretic magnetization-magnetic field (MH) loops in unfilled porous cobalt ferrite [Fig. S7(a)]. Unfilled cobalt ferrite thin films exhibit a saturation magnetization of about 340 emu/cc and coercivity of approximately 800 Oe, which is close to the literature values in thin films.[83,69,95,144,156] The piezoelectric properties of the ALD BFO were also investigated using polarization – electric field (PE) curves [Fig. S7(b)]. Since the BFO layers in this work are very thin, analogous thickness, planar films of the same thickness would easily short. We thus looked at the piezoelectric properties of ALD deposited BFO in thicker films of approximately 100 nm thickness. It is important to note that while the coercivity of the thick BFO was found to be approximately 70 kV/cm, that piezoelectric coercivity is dependent on material thickness, and so the coercivity of the thicker ALD film is not

representative of the coercivity of the thin BFO coatings in the nanocomposites studied in this work.[157–161]

With confirmation of the magnetic and piezoelectric hysteretic behaviors of CFO and BFO separately, we set out to study the magnetoelectric coupling in the porous nanocomposites. We electrically poled samples *ex situ* out-of-plane from the sample and collected hysteresis loops with the films both in the plane of the magnetic field and out of the plane of the magnetic field (more details on electrical poling of the porous composites, including a schematic of electrical poling and magnetic measurements, can be found in the supporting information, Fig. S8). In the plane of the applied magnetic field, we saw no change in magnetization (Fig. S9). This observation is in agreement with previous results on porous CFO-PZT nanocomposites, and is likely due to substrate clamping.[83,143,144]

Although the nanocomposites are clamped in-plane because they are covalently bound to the substrate, the films are free to strain out-of-plane, which correlates to the large out-of-plane magnetization changes observed (Fig. 4). Since BFO tenses in the along the direction of the electric field, upon out-of-plane electric poling, BFO is under out-of-plane tension. This strain is expected to be transferred to the CFO, since it is covalently bound to BFO. Therefore, CFO should also be in out-of-plane tension. CFO is a negative magnetostrictive material, meaning that its magnetization will decrease in the direction of tension.[116,145] Another way to think about this is in terms of the magnetic anisotropy in the system. CFO has high magnetocrystalline anisotropy and high magnetostriction. The high magnetocrystalline anisotropy means that at saturation, spins are generally aligned with the easy axis that is closest to the magnetic field direction, but generally do not align fully with the magnetic field in a sample made of randomly oriented grains. The observed magnetization in the out-of-plane direction is the out-of-plane component of the magnetization for

each domain. When the sample is electrically poled out-of-plane, the magnetostriction term adds to the magnetocrystalline anisotropy. Because the magnetostriction is negative, the strain term will favor in-plane spin alignment, and it will pull the easy axes away from the out-of-plane direction. Thus, after electric poling, at magnetic saturation in the out-of-plane direction, spins will still lie in the easy direction closest to out-of-plane. This means that the out-of-plane component of the magnetization will be reduced, and thus the saturation magnetization will be reduced. Thus, as the
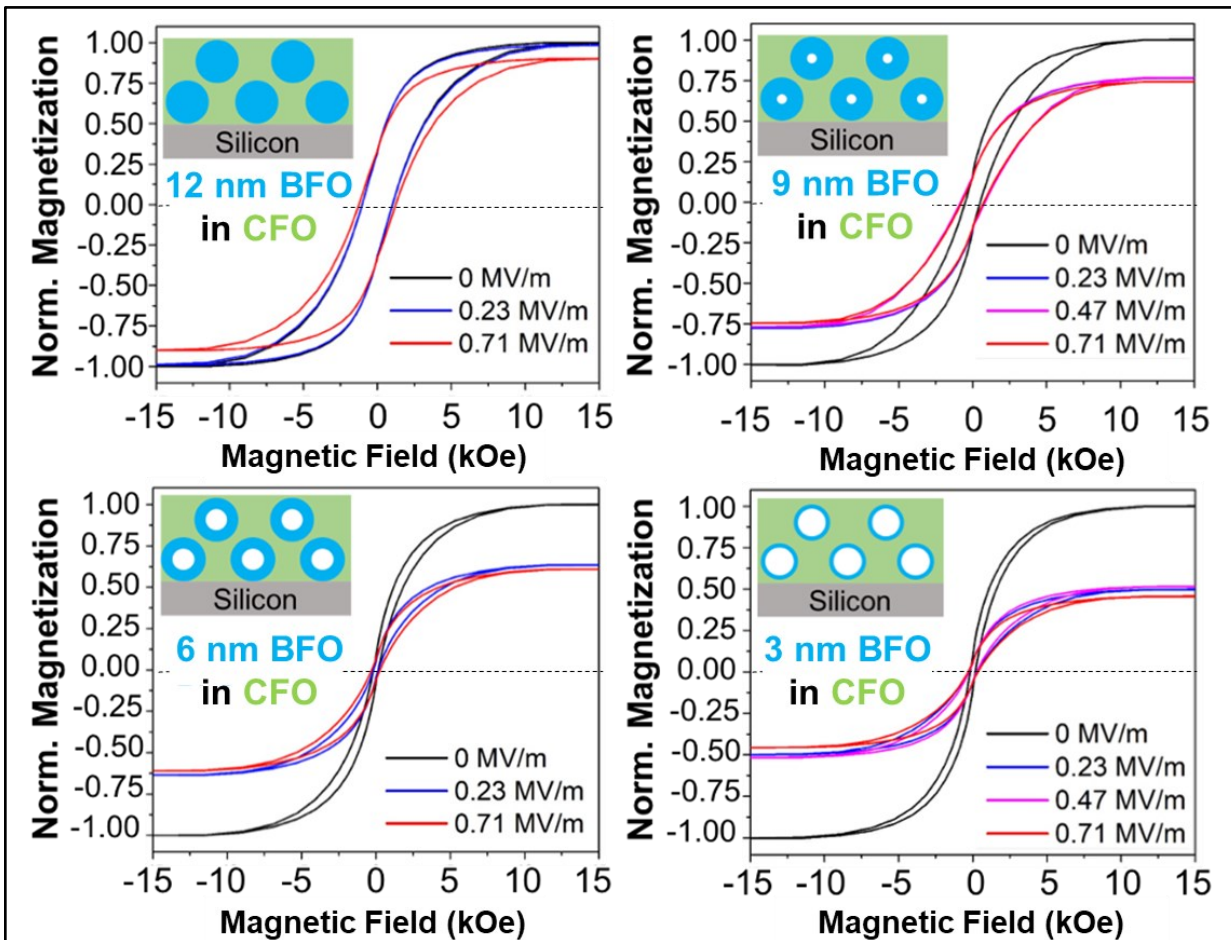
Figure 4-4. Residual porosity dependence in MH loops collected out of the plane of the magnetic field. As the BFO layers get thinner (and the residual porosity gets larger), the saturation magnetization changes get larger, reaching a large 60% decrease in magnetization in the composite with 3 nm of BFO.

multiferroic samples are electrically poled, their magnetization is expected to decrease in the out-of-plane direction, which is exactly what we observe in the samples studied in this work (Fig. 4).

In contrast to using strain to change magnetism, it has been shown that the saturation

Figure 4-5. Out-of-plane trends in (a) coercivity, (b) remnant magnetization, and (c) ME coefficient as a function of BFO layer thickness.
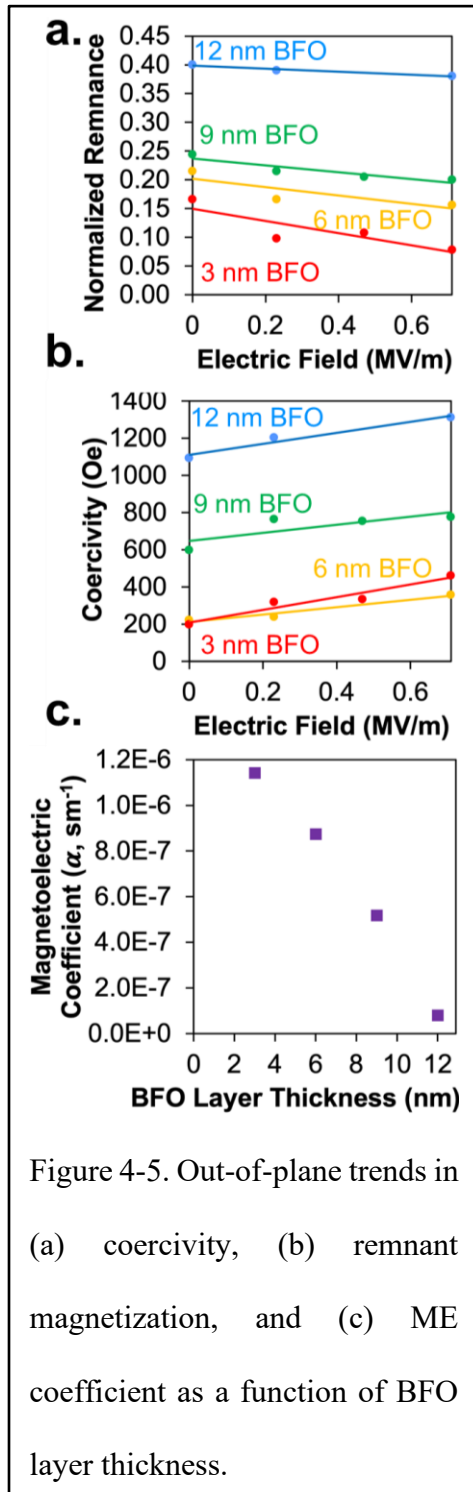
magnetization of CFO can change due to magneto-ionic effects.[162,163] This can either be due to redox at the magnetic ion (for example, Fe^{3+} has a magnetization of 5 μ_B, while Fe^{2+} has a magnetization of 4 μ_B) or due to the migration of O^{2-} anions.[164,165] As a control experiment, we poled bare, unfilled CFO at the same electric fields used in this work (Fig. S10). We observed no significant changes in the magnetization, ruling out ionic contributions to the magnetization change.

We calculated the magnetoelectric coupling in a range of samples with varying BFO layer thicknesses (3 nm, 6 nm, 9 nm, 12 nm) and thus, residual porosities (Fig. 5). Interestingly, the residual porosity of the sample was found to play a major role in the electric field induced changes. The fully-filled samples (12 nm thick BFO) were found to have around a 10% decrease in magnetization after poling to the highest fields used in this work, but as the amount of residual porosity increased, the magnetization change increased up to a 60% drop in magnetization in the samples with 3 nm BFO.

In addition to the large change in saturation magnetization, modest changes in coercivity and remnant magnetization were found upon

56

electrical poling [Fig. 5(a-b)]. We had hypothesized that upon out-of-plane electrical poling, that the BFO would strain so that it is under out-of-plane tension and in-plane compression, and since CFO is strain-coupled to BFO, that the CFO would also be under out-of-plane tension and in-plane compression. Since CFO is a negative magnetostrictive material, its easy axis should rotate to align more with the direction of compression. If this is true, then it should result in the out-of-plane coercivity getting larger, and the in-plane coercivity getting smaller. As mentioned previously, since the composite is substrate-clamped in-plane, we do not see significant changes in in-plane coercivity or saturation magnetization. However, we do see the coercivity getting larger in the out-of-plane direction, as expected [Fig. 5(a)]. Since the hard axis should rotate toward the out-of-plane direction upon electrical poling, we also expect the MH loop to be less square in the out-of-plane direction, which is observed in the plots of remnant magnetization [Fig. 5(b)].

We can use the change in saturation magnetization to calculate the converse magnetoelectric coefficient, defined as $\alpha = \mu_0 dM/dE$, where α is the magnetoelectric coefficient, μ_0 is the permeability of free space, dM is the change in saturation magnetization between the unpoled and poled states, and dE is the applied electric field used to get the largest magnetization change [Fig. 5(c)]. The magnetoelectric coefficients were calculated from the lowest electric field at which samples exhibited a saturated magnetization change (0.23 MV/m in all samples except the fully-filled sample, which required a higher field of 0.71 MV/m to saturate). The magnetoelectric coefficient of the fully-filled sample seemed to be on par with other reported BFO-CFO nanocomposites, which tend to be on the order of 10^{-7} s·m^{-1}.[166–168] However, for the sample with the most residual porosity, we calculate a large, out-of-plane magnetoelectric coefficient of 1.14×10^{-6} s·m^{-1}, an order of magnitude larger than dense multiferroic nanocomposites (both previously reported in the literature[143,144,153,166–168] and seen in the fully-

filled sample described in this work). The magnetoelectric coefficients described here are likely an underestimate, since samples were poled *ex situ*, and so the saturation magnetization changes were observed at the remnant (not saturation) polarization state of the piezoelectric. Thus, the actual magnetoelectric coefficient is expected to be even larger with *in situ* electrical poling, where BFO is at its saturation strain state. We note that, since we observe minimal magnetization changes in-plane due to substrate clamping, the in-plane magnetoelectric coefficients is near zero (Fig. S11). This anisotropy, with a large out-of-plane and small in-plane magnetoelectric coefficient, could be very useful in spintronic and microwave devices.[114,169]

We used high-resolution diffraction to corroborate that these large magnetoelectric changes indeed stem from strain changes. Changes in crystal structure, such as those measured by X-ray diffraction, can be mapped onto the macroscopic strains in the material. Samples were again poled *ex situ* in the out-of-plane direction at increasing electric fields, and the *d*-spacing was measured at each electric field (Fig. 6). If the magnetization change
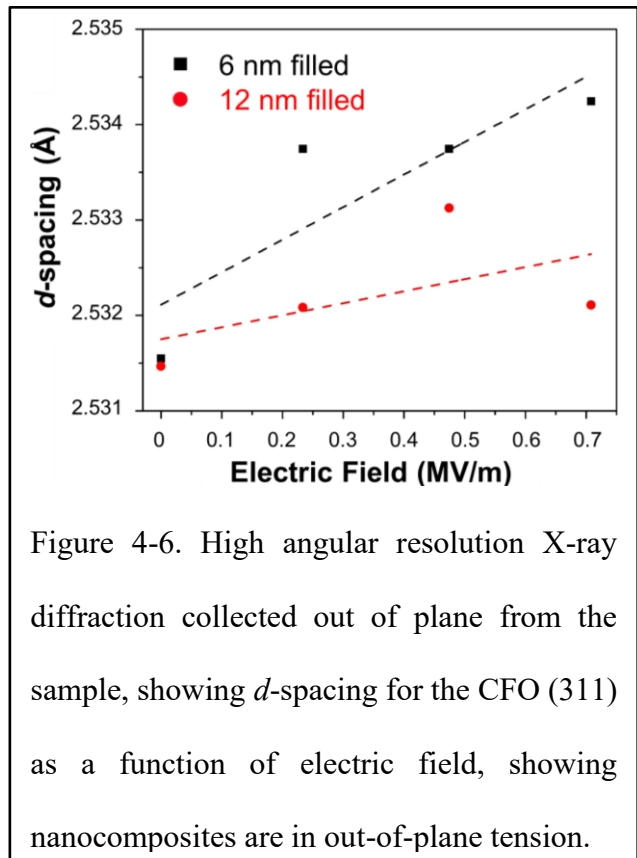
Figure 4-6. High angular resolution X-ray diffraction collected out of plane from the sample, showing *d*-spacing for the CFO (311) as a function of electric field, showing nanocomposites are in out-of-plane tension.

described above is truly induced by a strain-mediated mechanism, we expect that upon out-of-plane electrical poling, BFO should be in out-of-plane tension and in-plane compression. Since CFO is covalently bound to BFO, we also expect CFO to also be in increased out-of-plane tension. Given the thinness of the BFO ALD layer, it was difficult to resolve changes in *d*-spacing in any

of the BFO peaks, so strain changes in the piezoelectric could not be directly measured. However, since CFO is covalently bound to BFO, and thus strain-coupled, we can use the far more intense CFO(311) peaks to track strain changes in the composite. Thus, the measured lattice spacing changes in CFO was used to calculate a proxy (d'_{33}) for the d_{33}, or the longitudinal strain change expected for BFO as a function of the effective applied voltage. The calculated d'_{33} was found to be 2×10^{-9} m/V, which is just under the reported literature values for BFO of the same thicknesses.[151,170] It should be noted that this d'_{33} value is expected to be lower than actuality for two reasons. First, it was calculated assuming 100% strain transfer from the BFO to the CFO, which is not likely to be the case. Second, the value calculated in this work made use of samples that were poled *ex situ,* and thus have relaxed to their remnant polarization, rather than the saturation polarization. Nevertheless, the approximated d'_{33} from high-resolution diffraction demonstrates that strain transfer between the BFO and CFO is likely the origin of the magnetic changes observed here.

Importantly, the out-of-plane d-spacing for the sample with more residual porosity (6 nm filled, black in Fig. 6) was found to increase more than in the fully-filled sample (12 nm filled, red in Fig. 6). The d'_{33} was found to be 2×10^{-9} m/V in the 6 nm sample, whereas the d'_{33} in the 12 nm sample was found to be only 7×10^{-10} m/V. This large difference in d'_{33} is thought to be the result of the increased mechanical flexibility in the more porous nanocomposite, making the overall material easier for the material to strain.".[110]

CONCLUSIONS.

Overall, porous nanocomposites with residual porosity can have extremely large magnetization changes in comparison to their dense counterparts. This was realized in multiferroic nanocomposites with tunable residual porosity formed by ALD filling into a mesoporous

59

framework. The crystal structure of the piezoelectric and magnetostrictive phases of BFO and CFO were confirmed with GIWAXS, and their piezoelectricity and ferrimagnetism was confirmed with PE and MH loops, respectively. Since the resulting composite is more mechanically flexible and alleviates substrate clamping by providing room for CFO and BFO to flex, the magnetization changes are much larger than in dense composites. SQuID magnetometry measurements show large electric-field induced magnetization changes from a 12% change in magnetization in the fully-filled samples to an almost 60% change in the samples with the most residual porosity. The residual porosity was further found to increase the magnetoelectric coupling by more than an order of magnitude, with the converse magnetoelectric coupling coefficient found to be 8.1×10^{-8} s·m^{-1} in the fully-filled samples, increasing to 1.2×10^{-6} s·m^{-1} in the samples with the most residual porosity. Systems that can drive large magnetic changes, like the ones in this work, could have enormous potential for switchable magnetic systems, such as in the microwave and spintronic space.

ACKNOWLEDGMENT

APPENDIX A

Supporting Information for Chapter 2:

Delineating Magnetization Dynamics in Solution-Processed Doped Yttrium Iron

Garnet Thin Films

Shreya K. Patel, C. Ty Karaba, Sarah H. Tolbert

Thick film characterization: For stripline FMR measurements, thicker films were used in order to obtain reasonable absorption. The synthesis of these films is discussed in the experimental section of the main text.

From diffraction, we see that thicker films still form the correct crystal structure (figure S1(a)). It should be noted, however, that since diffraction patterns for the thick films were collected on a conventional powder diffractometer, rather than using a synchrotron source, the signal-to-noise ratio is lower for the diffraction in figure S1(a) than in figure 1 of the main text, even though the films are thicker. The saturation magnetization of the thick films is similar to the thinner films shown in figure 2 (approximately 140 emu/cc), but the coercivity is slightly larger in the thick films. A value of ~ 50 Oe was obtained for the thick films, as opposed to ~25 Oe obtained in the thinner films (figure S1(b)). This is likely because thicker sol-gel films often exhibit more defects (cracks, pores, etc.) than thinner films. This effect can be seen in cross-sectional SEM images of thick and thin films (figure S1(c)). These defect sites can become domain wall pinning sites, which would increase the coercive field. For the same reason, we expect that magnetic inhomogeneities could also result in higher FMR linewidth in thicker films than thinner films, due to an increase in inhomogeneous line broadening. This topic is already discussed in the main text on manuscript.

To better assess how similar the magnetic losses are in thick and thinner films, we turned to electron spin resonance (ESR) to look at the dynamic magnetic behavior in an undoped thinner film (figure S1(d)). ESR utilizes a cavity tuned to a single frequency (9.8 GHz in this case), and due to the cavity resonance, it can measure the small signal from the thinner films, providing a point of direct comparison between film thicknesses. The linewidth of the thinner film is 238 Oe peak-to-peak, which corresponds to a FWHM value of 280 Oe. This value is lower than the thick films film value of 350 Oe, obtained by extrapolating stripline data to 9.8 GHz using the inhomogeneous line broadening (ΔH_0) and Gilbert damping (α) (main text, table 1), but the values are similar, and the difference is likely due to the defect sites discussed above. Overall, the values between thick and thinner films are similar enough that it appears reasonable to obtain absorption from stripline FMR measurements for thick films across a range of frequencies.
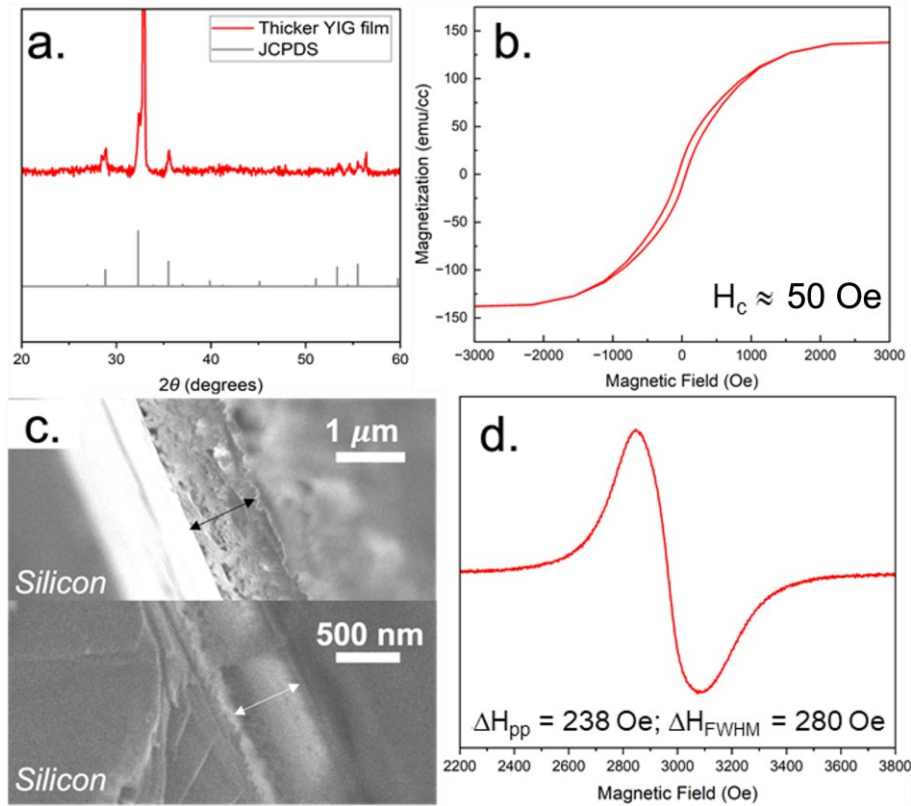
Figure A-S1. Characterization of thicker YIG films to compare to the thinner films discussed in the manuscript, including (a) X-ray diffraction (* indicates Si substrate peak), (b) an MH loop obtained trough SQuID magnetometry, and (c) SEM. An ESR spectrum of the thinner film (d) shows linewidth of the films at 9.8 GHz. Thus, while the coercivity and FMR linewidth of thicker films is slightly higher than those mentioned in the manuscript (likely due to an increase in defects in thicker films), they are overall comparable to the thinner films described in the manuscript.

Supporting Information for Chapter 4:

Increased Magnetoelectric Coupling in Porous Nanocomposites of CoFe$_2$O$_4$ and

BiFeO$_3$ with Residual Porosity for Switchable Magnetic Devices

Shreya K. Patel,[†] C. Ty Karaba,[†] Daniel D. Robertson, Jeffrey Chang, Kevin Fitzell,

Charlene Z. Salamat, Jane P. Chang, Sarah H. Tolbert

[†]These authors contributed equally to this work.
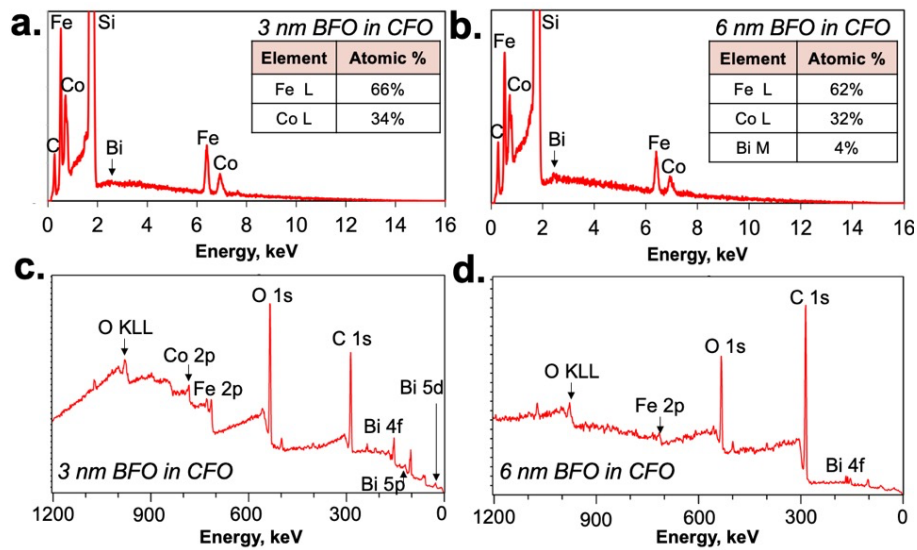
Figure B-S1. SEM-EDS [(a) + (b)] and XPS [(c) + (d)] measurements on the 3 nm-BFO [(a) + (c)] and the 6 nm-thick BFO composites [(b) + (d)]. SEM-EDS shows that cobalt and iron are in the atomic ratios expected for CFO, and that Bi is present in both samples. Given the relatively small volume of Bi and the intrinsic low intensity of the Bi peaks, we were not able to quantify the Bi:Co ratios in the 3 nm sample. XPS data from the composites confirm the presence of bismuth and iron

from BFO in both the 3 nm and 6 nm samples. Co is not observed in XPS data collected on samples with a 6 nm BFO layer due to the low penetration depth of XPS.
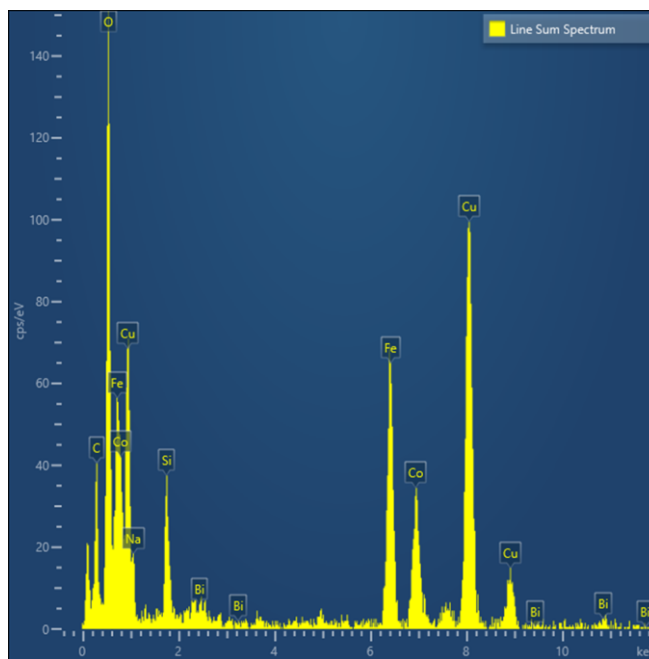
Figure B-S2. Representative STEM-EDS spectrum of the 6 nm BFO in CFO composite.

Discussion of Microstrain in the Nanoporous CFO and in the Composite

We begin with discussion of the initial *macro*strain (from uniform lattice distortion, which result in X-ray diffraction peak shifts) and *micro*strain (from inhomogeneous sources of strain, including dislocations, vacancies, and grain boundaries, which result in X-ray diffraction peak broadening) in the nanoporous CFO alone. We compared the in-plane and out-of-plane diffraction peaks from GIWAXS patterns (collected with rocking scans to obtain true out-of-plane data) with the JCPDS values and found that the films were under tensile strain in-plane, and compressive strain out-of-plane (Fig. S3). This strain state arises from the thermal expansion coefficient mismatch between the substrate (silicon) and the film (CFO). Silicon has a much lower thermal expansion coefficient (3.5×10^{-6} K^{-1}) than CFO (1.0×10^{-5} K^{-1}), and so it contracts less than the

CFO film upon cooling the after annealing.[303,304] The CFO film is clamped in the in-plane direction, so the films should be under in-plane tensile stress, and out-of-plane compressive stress.
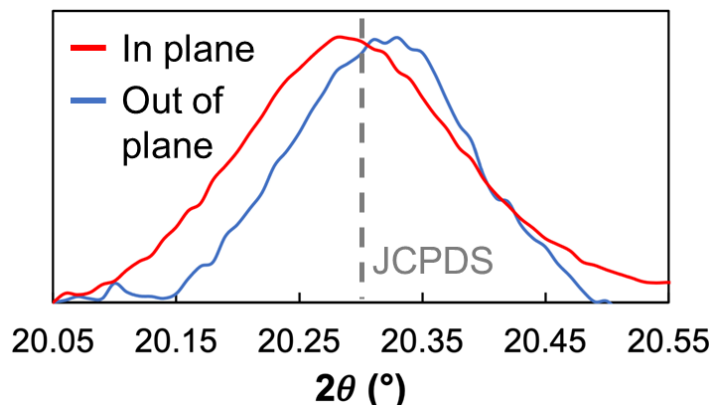
Figure B-S3. The CFO(311) X-ray diffraction peak for porous CFO at an X-ray energy = 0.98 Å, showing in-plane tension and out-of-plane compression from thermal strain.

We next consider both macro- and microstrain in the CFO-BFO composite structures. Globally, the CFO peaks in the composite films were found to all be under similar in-plane tension and out-of-plane compression (Fig. S4), likely due to the thermal strains discussed above.
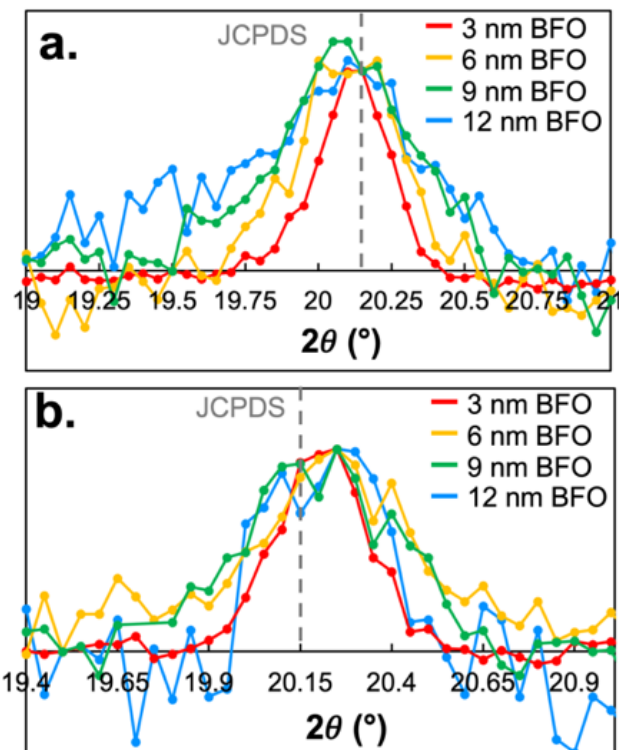
Figure B-S4. The CFO(311) X-ray diffraction (a) in-plane and (b) out-of-plane peak in the composites at an X-ray energy = 0.88 Å.

Interestingly, the CFO peaks were also found to exhibit a large degree of broadening with increased BFO layer thickness. We used Williamson-Hall plots for GIWAXS patterns to investigate if the broadening with increased BFO layer thickness and determine if it was due to a difference in grain size (i.e. differences in Scherrer width), or if it was due to an increase in microstrain (Fig. S5). The slope of the Williamson-Hall plot is proportional to the broadening from strain, while the y-intercept is inversely proportional to the broadening from grain size. All y-intercept values of the Williamson-Hall plots across the sets of samples were approximately the same, indicating that size effects did not dominate. We did, however, observe a monotonic increase in the slope of the Williamson-Hall plots with BFO layer thickness, leading us to believe that increased BFO layer thickness increases the overall microstrain of the nanoporous CFO. While the

diffraction intensity of the BFO peaks in the 3 nm, 6 nm, and 9 nm thick samples were too low in intensity to be seen with X-ray diffraction, we expect that since CFO is strain-coupled to BFO through covalent bonding, we believe that BFO is also under increasingly large microstrain as a function of BFO layer thickness. This is interesting, as we would expect the thinner BFO layers to be under the most microstrain since ultrathin films are known to usually be dominated by strain from large surface energy.[130,305–307] The additional strain is therefore believed to be the result of additional, growth-related crystallization strains as the BFO layer gets thicker, which is larger than the interfacial strain.
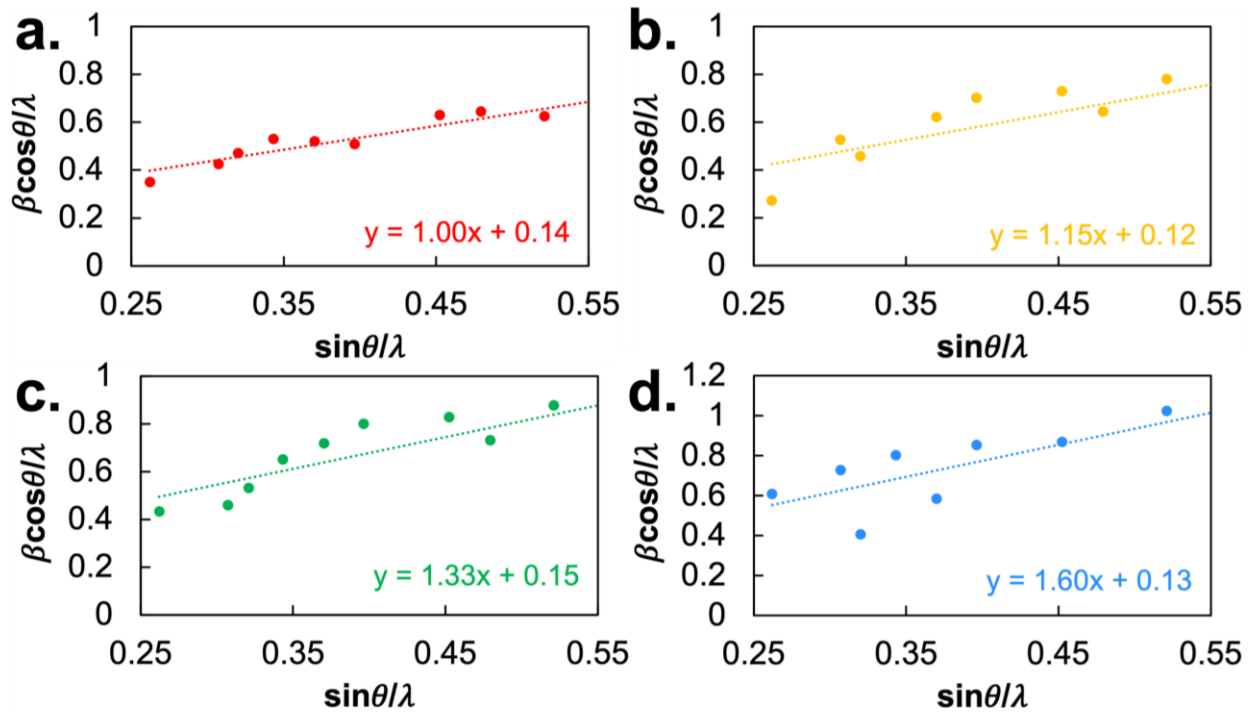
Figure B-S5. Williamson-Hall plots for CFO in the GIWAXS patterns of composites.

We should note that these observations of changes in the initial microstrain state do not contradict the larger conclusions of this manuscript. Both magnetoelectric and strain measurements show out-of-plane tensile strain, which may be facilitated by the initial out-of-plane

compressive strain state. The microstrain is inhomogeneous, and so will not contribute to magnetic alignment.
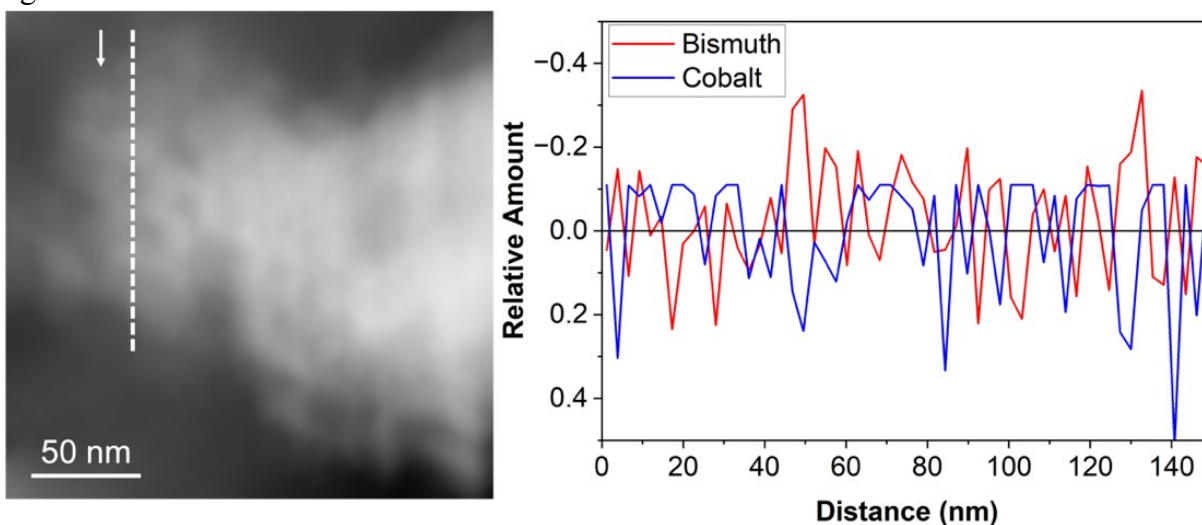
Figure B-S6. Quantitative STEM-EDS line scan mapping of Bi and Co for the 6 nm BFO in CFO composite. The position of the line is shown on the left, with the elemental data presented on the right. Clear anti-correlation of the Bi and Co intensities is observed.
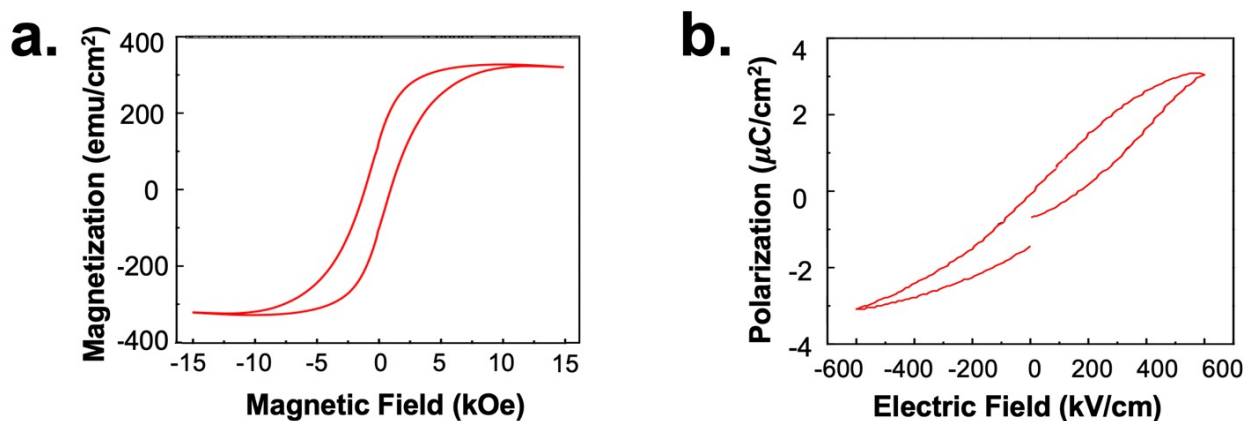
Figure B-S7. Hysteretic loops for CFO and BFO components of the nanocomposites, including (a) MH loop for porous CFO and (b) PE loop for thick film of ALD BFO (b), demonstrating acceptable magnetic and piezoelectric properties.
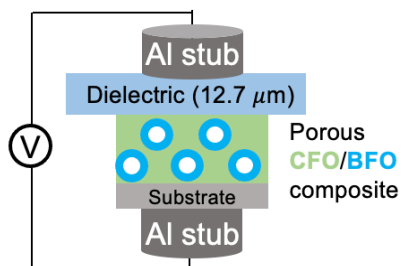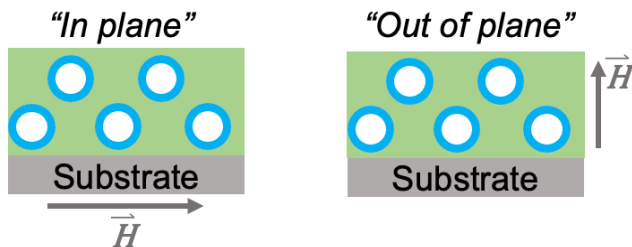
Figure B-S8. Schematic of (a) *ex situ* electrical poling and (b) "in plane" versus "out of plane" magnetic measurements.
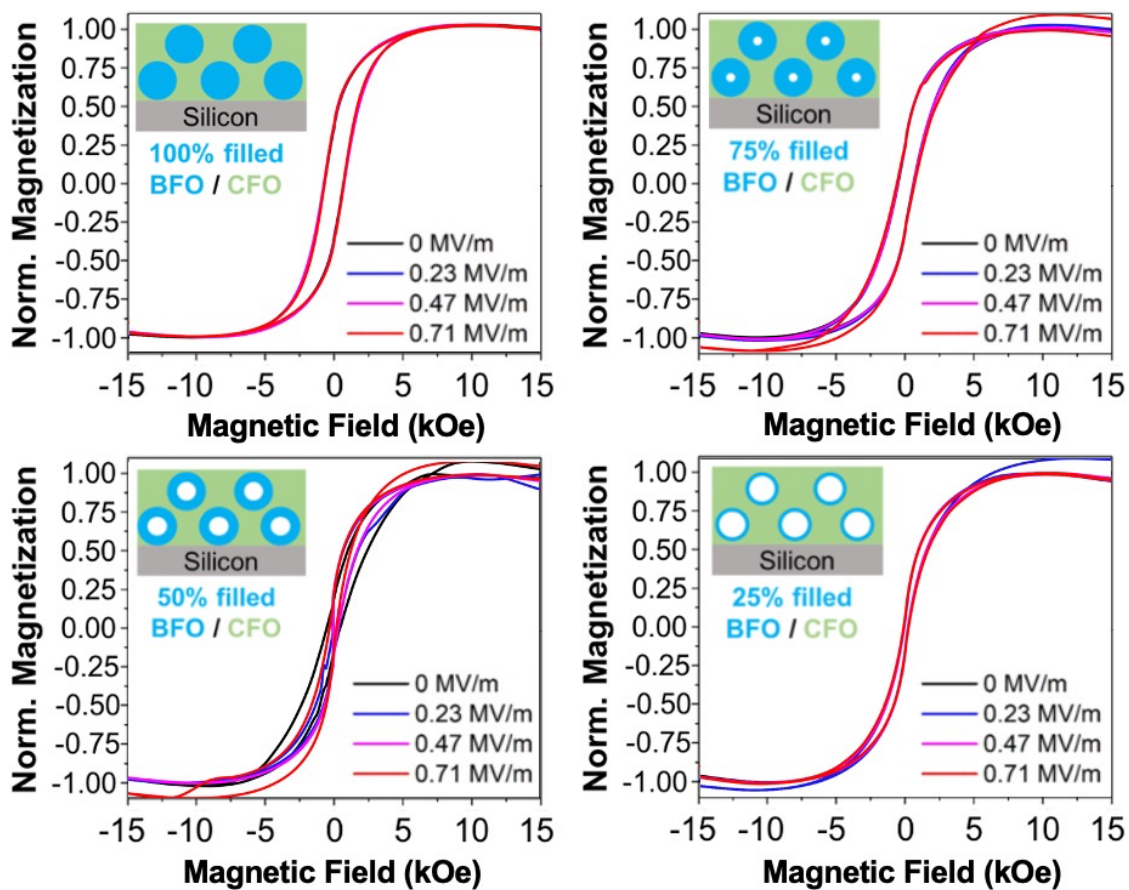
Figure B-S9. In plane SQuID magnetometry measurements for the 25%, 50%, 75%, and 100% filled nanocomposites, electrically poled from 0 to 0.71 MV/m. Magnetization in plane does not change, likely due to substrate clamping.
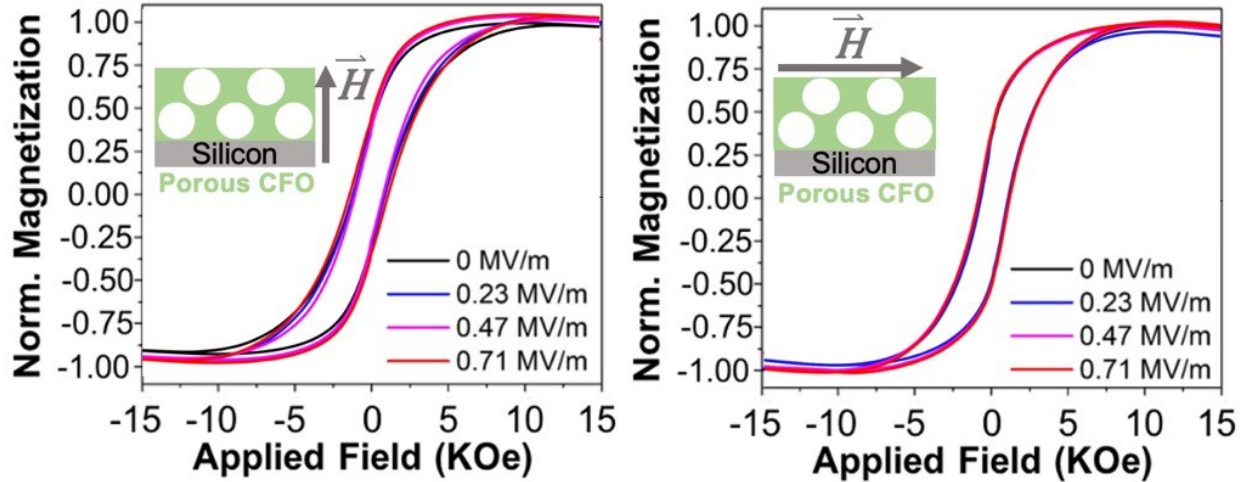
Figure B-S10. SQuID magnetometry on bare, porous CFO poled in situ from 0 to 0.71 MV/m. Measurements were taken out of plane from the magnetic field (left) and in the plane of the magnetic field (right). No large changes in magnetization was observed.
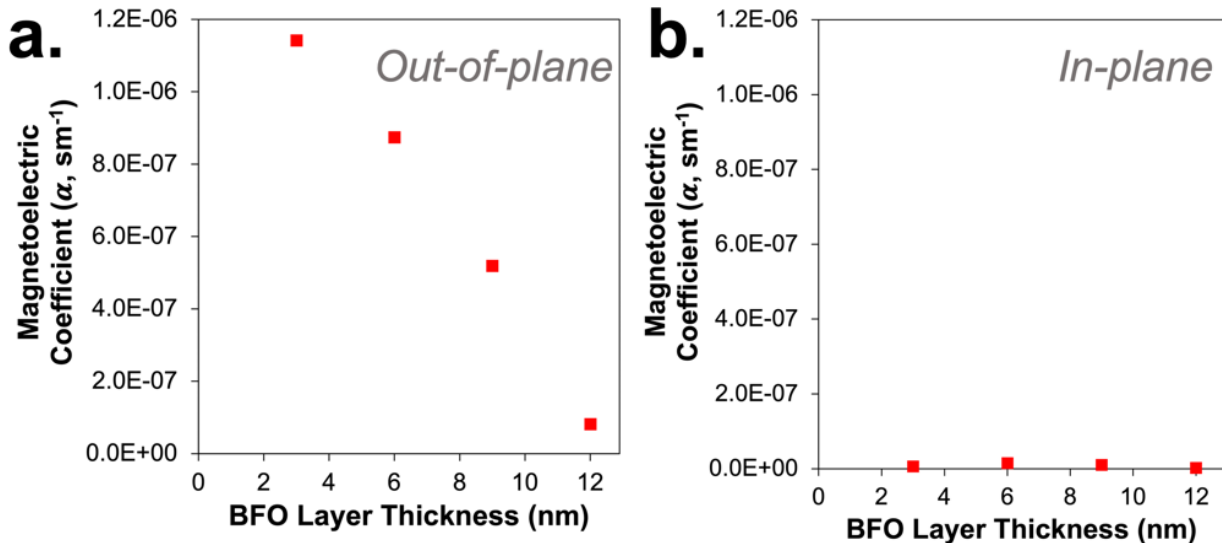
Figure B-S11. Comparison of out-of-plane magnetoelectric coefficient (a) vs. the in-plane magnetoelectric coefficient (b).

REFERENCES

1) Zhou, H. M.; Zhu, F. J.; Li, C.; Xiao, Y. Ferrite-Piezoelectric Layered Composite Materials for Magnetoelectric Tunable Dual-Band Bandpass Filter. *Appl. Mech. Mater.* **2013**, *303–306*, 1793–1797.

2) Tatarenko, A. S.; Gheevarughese, V.; Srinivasan, G. Magnetoelectric Microwave Bandpass Filter. *Electron. Lett.* **2006**, *42*, 540–541.

3) Yao, Z.; Wang, Y. E.; Keller, S.; Carman, G. P. Bulk Acoustic Wave-Mediated Multiferroic Antennas: Architecture and Performance Bound. *IEEE Trans. Antennas Propag.* **2015**.

4) Wang, X. G.; Sukhov, A.; Chotorlishvili, L.; Jia, C. L.; Guo, G. H.; Berakdar, J. Electrically Driven Magnetic Antenna Based on Multiferroic Composites. *J. Phys. Condens. Matter* **2017**.

5) Petrov, R. V.; Tatarenko, A. S.; Pandey, S.; Srinivasan, G.; Mantese, J. V.; Azadegan, R. Miniature Antenna Based on Magnetoelectric Composites. *Electron. Lett.* **2008**, *44*, 506–508.

6) Hauser, C.; Richter, T.; Homonnay, N.; Eisenschmidt, C.; Qaid, M.; Deniz, H.; Hesse, D.; Sawicki, M.; Ebbinghaus, S. G.; Schmidt, G. Yttrium Iron Garnet Thin Films with Very Low Damping Obtained by Recrystallization of Amorphous Material. *Sci. Rep.* **2016**, *6*, 1–8.

7) Yahya, N. B.; Koziol, K. K. K.; Bin Mansor, M. K. Synthesis and Characterization of Single Crystals Y3Fe5O12 and Bi3Fe5O12 Prepared via Sol Gel Technique. *Defect Diffus. Forum* **2008**, *283–286*, 406–412.

8) Stadler, B. J. H.; Mizumoto, T. Integrated Magneto-Optical Materials and Isolators: A Review. *IEEE Photonics J.* **2014**, *6*.

9) Ghosh, S.; Keyvaninia, S.; Shoji, Y.; Van Roy, W.; Mizumoto, T.; Roelkens, G.; Baets, R. G. Compact Mach-Zehnder Interferometer Ce:YIG/SOI Optical Isolators. *IEEE Photonics Technol. Lett.* **2012**, *24*, 1653–1656.

10) Firby, C. J.; Elezzabi, A. Y. Design of Integrated YIG-Based Isolators and High-Speed Modulators. *Ultrafast Phenom. Nanophotonics* **2016**, *9746*, 108–115.

11) How, H.; Shi, P.; Vittoria, C.; Kempel, L. C.; Trott, K. D. Single-Crystal YIG Phase Shifter Using Composite Stripline Structure at X Band. *J. Appl. Phys.* **2000**, *87*, 4966.

12) Wang, X. guang; Chotorlishvili, L.; Guo, G. hua; Berakdar, J. Electric Field Controlled Spin Waveguide Phase Shifter in YIG. *J. Appl. Phys.* **2018**, *124*, 073903.

13) Yang, X.; Gao, Y.; Wu, J.; Zhou, Z.; Beguhn, S.; Nan, T.; Sun, N. X. Voltage Tunable Multiferroic Phase Shifter with YIG/PMN-PT Heterostructure. *IEEE Microw. Wirel. Components Lett.* **2014**, *24*, 191–193.

14) Baños-López, E.; Cortés-Escobedo, C. A.; Sánchez-De Jesús, F.; Barba-Pingarrón, A.; Bolarín-Miró, A. M. Crystal Structure and Magnetic Properties of Cerium-Doped YIG: Effect of Doping Concentration and Annealing Temperature. *J. Alloys Compd.* **2018**, *730*, 127–134.

15) Hansen, P.; Witter, K.; Tolksdorf, W. Magnetic and Magneto-Optic Properties of Lead- and Bismuth-Substituted Yttrium Iron Garnet Films. *Phys. Rev. B* **1983**, *27*, 6608–6625.

16) Krishnan, R.; Cagan, V.; Rivoire, M.; Graham, C. D.; Rhyne, J. J. Magnetostriction in Ruthenium-Doped YIG Crystals. In *AIP Conference Proceedings*; AIP, 2012; Vol. 5, pp 704–706.

17) Comstock, R. L.; Raymond, J. J. Magnetostriction of Ytterbium and Cerium in YIG. *J. Appl. Phys.* **1967**, *38*, 3737–3739.

18) Kehlberger, A.; Richter, K.; Onbasli, M. C.; Jakob, G.; Kim, D. H.; Goto, T.; Ross, C. A.; Götz, G.; Reiss, G.; Kuschel, T.; Kläui, M. Enhanced Magneto-Optic Kerr Effect and Magnetic Properties of $CeY_2Fe_5O_{12}$ Epitaxial Thin Films. *Phys. Rev. Appl.* **2015**, *4*, 014008.

19) Enke, K.; Fleishhauer, J.; Gunsser, W.; Hanser, P.; Nomura, S.; Tolksdorf, W.; Winkler, G.; Wolfmeier, U.; Hellwege, K.-H.; Hellwege, A. M. *Magnetic and Other Properties of Oxides and Related Compounds: Part A: Garnets and Perovskites*; Springer-Verlag: New York, 1978.

20) Smith, A. B.; Jones, R. V. Magnetostriction Constants from Ferromagnetic Resonance. *J. Appl. Phys.* **1963**, *34*, 1283–1284.

21) Lage, E.; Beran, L.; Quindeau, A. U.; Ohnoutek, L.; Kucera, M.; Antos, R.; Sani, S. R.; Dionne, G. F.; Veis, M.; Ross, C. A. Temperature-Dependent Faraday Rotation and Magnetization Reorientation in Cerium-Substituted Yttrium Iron Garnet Thin Films. *APL Mater.* **2017**, *5*, 036104.

22) Kuila, M.; Deshpande, U.; Choudhary, R. J.; Rajput, P.; Phase, D. M.; Raghavendra Reddy, V. Study of Magneto-Optical Activity in Cerium Substituted Yttrium Iron Garnet (Ce:YIG) Epitaxial Thin Films. *J. Appl. Phys.* **2021**, *129*, 93903.

23) Onbasli, M. C.; Beran, L.; Zahradník, M.; Kucera, M.; Antoš, R.; Mistrík, J.; Dionne, G. F.; Veis, M.; Ross, C. A. Optical and Magneto-Optical Behavior of Cerium Yttrium Iron Garnet Thin Films at Wavelengths of 200-1770 Nm. *Sci. Rep.* **2016**, *6*, 1–10.

24) Dionne, G. F. The Magnetoelastic Ion: Friend and Foe to Microwaves. *IEEE Trans. Magn.* **2011**, *47*, 272–278.

25)   Acosta, A.; Fitzell, K.; Schneider, J. D.; Dong, C.; Yao, Z.; Sheil, R.; Wang, Y. E.; Carman, G. P.; Sun, N. X.; Chang, J. P. Underlayer Effect on the Soft Magnetic, High Frequency, and Magnetostrictive Properties of FeGa Thin Films. *J. Appl. Phys.* **2020**, *128*, 013903.

26)   Gu, W.; Xu, Q.; Wang, Y. E. Two Dimensional (2D) Complex Permeability Characterization of Thin Film Ferromagnetic Material. In *2016 IEEE Conference on Antenna Measurements & Applications (CAMA 2016)*; Syracuse, 2016; pp 224–228.

27)   Bonnet, M.; Delapalme, A.; Fuess, H.; Thomas, M.; IUCr. Refinement of the Structure of Yttrium Iron Garnet (YIG): A Case of Severe Extinction and Absorption. *Acta Crystallogr.* **1975**, *31*, 2233–2240.

28)   Geller, S. Magnetic Behavior of Substituted Ferrimagnetic Garnets. *J. Appl. Phys.* **2004**, *37*, 1408.

29)   K.H. Hellwege; A.M. Hellwege. *Landolt-Börnstein - Group III Crystal and Solid State Physics*; Spinger-Werlag: Berlin/Heidelberg, 1978; Vol. 18a.

30)   Hansen, P. Ferromagnetic Resonance in Ruthenium-doped Yttrium–Iron Garnet. *Phys. status solidi* **1971**, *47*, 565–572.

31)   Öztürk, Y.; Avgin, I.; Erol, M.; Çelik, E. Cerium-Doped Yttrium Iron Garnet Thin Films Prepared by Sol-Gel Process: Synthesis, Characterization, and Magnetic Properties. In *Advances in Nanoscale Magnetism*; 2009; pp 113–129.

32)   Shirsath, S. E.; Gaikwad, A. S.; Kadam, A. B.; Borade, R. B.; Patange, S. M.; Kadam, S. B.; Vats, G.; Kadam, R. H. Polycrystalline to Preferred-(100) Single Crystal Texture Phase Transformation of Yttrium Iron Garnet Nanoparticles. *Nanoscale Adv.* **2018**.

33)   Casals, B.; Espínola, M.; Cichelero, R.; Geprägs, S.; Opel, M.; Gross, R.; Herranz, G.; Fontcuberta, J. Untangling the Contributions of Cerium and Iron to the Magnetism of Ce-Doped Yttrium Iron Garnet. *Appl. Phys. Lett.* **2016**, *108*.

34)   Niyaifar, M.; Mohammadpour, H.; Khalafi, N. Effects of Structural Distortion on Magnetic Properties of $Ce_xY_{3-x}Fe_5O_{12}$. *J. Alloys Compd.* **2016**, *688*, 357–362.

35)   Gharibshahi, M. Physical Properties of Cerium Doped-Yttrium Iron Garnet Ultrathin Films for Photovoltaic Application. *Ceram. Int.* **2019**, *45*, 24437–24445.

36)   Sharma, V.; Saha, J.; Patnaik, S.; Kuanr, B. K. Synthesis and Characterization of Yttrium Iron Garnet (YIG) Nanoparticles - Microwave Material. *AIP Adv.* **2016**, *7*, 056405.

37)   Peña-Garcia, R.; Delgado, A.; Guerra, Y.; Farias, B. V. M.; Martinez, D.; Skovroinski, E.; Galembeck, A.; Padrón-Hernández, E. Magnetic and Structural Properties of Zn-Doped Yttrium Iron Garnet Nanoparticles. *Phys. Status Solidi Appl. Mater. Sci.* **2016**, *213*, 2485–2491.

38) Kuchi, R.; Kim, S. Il; Lee, K. M.; Lee, Y.; Park, S. Y.; Jeong, J. R. Annealing Effect on Ferromagnetic Resonance and Magnetic Properties of YIG Nanocrystals Prepared by Citrate Precursor Sol-Gel Method. *Nanosci. Nanotechnol. Lett.* **2015**.

39) Nguyet, D. T. T.; Duong, N. P.; Satoh, T.; Anh, L. N.; Hien, T. D. Temperature-Dependent Magnetic Properties of Yttrium Iron Garnet Nanoparticles Prepared by Citrate Sol–Gel. *J. Alloys Compd.* **2012**, *541*, 18–22.

40) Musa, M. A.; Azis, R. S.; Osman, N. H.; Hassan, J.; Zangina, T. Structural and Magnetic Properties of Yttrium Iron Garnet (YIG) and Yttrium Aluminum Iron Garnet (YAlG) Nanoferrite via Sol-Gel Synthesis. *Results Phys.* **2017**, *7*, 1135–1142.

41) Leal, L. R. F.; Guerra, Y.; Padrón-Hernández, E.; Rodrigues, A. R.; Santos, F. E. P.; Peña-Garcia, R. Structural and Magnetic Properties of Yttrium Iron Garnet Nanoparticles Doped with Copper Obtained by Sol Gel Method. *Mater. Lett.* **2019**, *236*, 547–549.

42) Borade, R. B.; Shirsath, S. E.; Vats, G.; Gaikwad, A. S.; Patange, S. M.; Kadam, S. B.; Kadam, R. H.; Kadam, A. B. Polycrystalline to Preferred-(100) Single Crystal Texture Phase Transformation of Yttrium Iron Garnet Nanoparticles. *Nanoscale Adv.* **2019**, *1*, 403–413.

43) Peña-Garcia, R.; Delgado, A.; Guerra, Y.; Padrón- Hernández, E. Yig Films With Low Magnetic Damping Obtained By Solgel On Silicon (100). *Mater. Lett.* **2015**, *161*, 384–386.

44) Liu, F.; Ye, S. YIG Thin Film for RF Integrated Inductor. *J. Wuhan Univ. Technol. Mater. Sci. Ed.* **2017**.

45) Tsuchiya, T.; Sei, T.; Kanda, H. Sol-Gel Preparation of YIG (Y3Fe5O12) Thin Film Showing Opto-Magnetic Effect. *J. Non. Cryst. Solids* **1992**.

46) Shaiboub, R. E.; Ibrahim, N. B. Characterization of Erbium Substituted Yttrium Iron Garnet Films Prepared by Sol-Gel Method. *J. Nanosci.* **2014**.

47) Delgado, A.; Guerra, Y.; Padrón-Hernández, E.; Peña-Garcia, R. Combining the Sol Gel Method and Spin Coating to Obtain YIG Films with Low FMR Linewidth on Silicon (100) Substrate. *Mater. Res. Express* **2018**.

48) Lucas, I.; Jiménez-Cavero, P.; Vila-Fungueiriño, J. M.; Magén, C.; Sangiao, S.; De Teresa, J. M.; Morellón, L.; Rivadulla, F. Chemical Solution Synthesis and Ferromagnetic Resonance of Epitaxial Thin Films of Yttrium Iron Garnet. *Phys. Rev. Mater.* **2017**, *1*, 074407.

49) Guo, X.; Chen, Y.; Wang, G.; Zhang, Y.; Ge, J.; Tang, X.; Ponchel, F.; Rémiens, D.; Dong, X. Growth and Characterization of Yttrium Iron Garnet Films on Si Substrates by Chemical Solution Deposition (CSD) Technique. *J. Alloys Compd.* **2016**, *671*, 234–237.

50) Singh, B. K.; Mishra, S. K. Microstructure and Surface Morphology of YIG and 2 Wt% Ce-Doped YIG Thin Films Synthesized via Sol-Gel Method. *Mater. Today Proc.* **2020**, *44*, 886–889.

51) Chen, F.; Wang, X.; Nie, Y.; Li, Q.; Ouyang, J.; Feng, Z.; Chen, Y.; Harris, V. G. Ferromagnetic Resonance Induced Large Microwave Magnetodielectric Effect in Cerium Doped $Y_3Fe_5O_{12}$ Ferrites. *Sci. Rep.* **2016**, *6*, 1–8.

52) Oosterhout, S. D.; Savikhin, V.; Zhang, J.; Zhang, Y.; Burgers, M. A.; Marder, S. R.; Bazan, G. C.; Toney, M. F. Mixing Behavior in Small Molecule:Fullerene Organic Photovoltaics. *Chem. Mater.* **2017**, *29*, 3062–3069.

53) Ilavsky, J. Nika: Software for Two-Dimensional Data Reduction. *J. Appl. Crystallogr.* **2012**, *45*, 324–328.

54) Xu, Q.; Gu, W.; Wang, Y. E. Two Dimensional (2D) Complex Permeability Characterization of Thin Film Ferromagnetic Material. In *2016 IEEE Conference on Antenna Measurements and Applications, CAMA 2016*; Institute of Electrical and Electronics Engineers Inc., 2017.

55) Onbasli, M. C.; Kehlberger, A.; Kim, D. H.; Jakob, G.; Kläui, M.; Chumak, A. V.; Hillebrands, B.; Ross, C. A. Pulsed Laser Deposition of Epitaxial Yttrium Iron Garnet Films with Low Gilbert Damping and Bulk-like Magnetization. *APL Mater.* **2014**, *2*, 106102.

56) Hauser, H.; Jiles, D. C.; Melikhov, Y.; Li, L.; Grössinger, R. An Approach to Modeling the Dependence of Magnetization on Magnetic Field in the High Field Regime. *J. Magn. Magn. Mater.* **2006**, *300*, 273–283.

57) Yaln, O.; Lo, C.-K.; Montiel, H.; Alvarez, G.; Sharma, M.; Pathak, S.; Sharma, M.; Widuch, S.; Stamps, R. L.; Skrzypek, D.; Celinski, Z.; Vázquez-Victorio, G.; Acevedo-Salas, U.; Valenzuela, R.; Yoshikiyo, M.; Namai, A.; Ohkoshi, S.; Fu, S.-F.; Wang, X.-Z. *Ferromagnetic Resonance*; Yaln, O., Ed.; InTech, 2013.

58) Dubs, C.; Surzhenko, O.; Linke, R.; Danilewsky, A.; Brückner, U.; Dellith, J. Sub-Micrometer Yttrium Iron Garnet LPE Films with Low Ferromagnetic Resonance Losses. *J. Phys. D. Appl. Phys.* **2017**, *50*, 204005.

59) Beaujour, J. M.; Ravelosona, D.; Tudosa, I.; Fullerton, E. E.; Kent, A. D. Ferromagnetic Resonance Linewidth in Ultrathin Films with Perpendicular Magnetic Anisotropy. *Phys. Rev. B - Condens. Matter Mater. Phys.* **2009**, *80*, 180415.

60) Hurben, M. J.; Patton, C. E. Theory of Two Magnon Scattering Microwave Relaxation and Ferromagnetic Resonance Linewidth in Magnetic Thin Films. *J. Appl. Phys.* **1998**, *83*, 4344–4365.

61) Kalarickal, S. S.; Mo, N.; Krivosik, P.; Patton, C. E. Ferromagnetic Resonance Linewidth Mechanisms in Polycrystalline Ferrites: Role of Grain-to-Grain and Grain-Boundary Two-Magnon Scattering Processes. *Phys. Rev. B - Condens. Matter Mater. Phys.* **2009**, *79*, 094427.

62) Man, H.; Shi, Z.; Xu, G.; Xu, Y.; Chen, X.; Sullivan, S.; Zhou, J.; Xia, K.; Shi, J.; Dai, P. Direct Observation of Magnon-Phonon Coupling in Yttrium Iron Garnet. *Phys. Rev. B* **2017**.

63) Fetisov, Y. K.; Srinivasan, G. Ferrite/Piezoelectric Microwave Phase Shifter: Studies on Electric Field Tunability. *Electron. Lett.* **2005**, *41*, 1066–1067.

64) Kittel, C. On the Theory of Ferromagnetic Resonance Absorption. *Phys. Rev.* **1948**, *73*, 155.

65) Man, H.; Shi, Z.; Xu, G.; Xu, Y.; Chen, X.; Sullivan, S.; Zhou, J.; Xia, K.; Shi, J.; Dai, P. Direct Observation of Magnon-Phonon Coupling in Yttrium Iron Garnet. *Phys. Rev. B* **2017**, *96*, 100406.

66) Kittel, C. Theory of Ferromagnetic Resonance in Rare Earth Garnets. *Phys. Rev.* **1959**, *115*, 1587.

67) Rosenberg, E. R.; Litzius, K.; Shaw, J. M.; Riley, G. A.; Beach, G. S. D.; Nembach, H. T.; Ross, C. A. Magnetic Properties and Growth-Induced Anisotropy in Yttrium Thulium Iron Garnet Thin Films. *Adv. Electron. Mater.* **2021**, *7*, 2100452.

68) Spaldin, N. A.; Fiebig, M. The Renaissance of Magnetoelectric Multiferroics. *Science.* **2005**, *309*, 391–392.

69) Nan, C.-W.; Bichurin, M. I.; Dong, S.; Viehland, D.; Srinivasan, G. Multiferroic Magnetoelectric Composites: Historical Perspective, Status, and Future Directions. *J. Appl. Phys.* **2008**, *103*, 031101.

70) Vaz, C. A. F.; Hoffman, J.; Ahn, C. H.; Ramesh, R. Magnetoelectric Coupling Effects in Multiferroic Complex Oxide Composite Structures. *Adv. Mater.* **2010**, *22*, 2900–2918.

71) Spaldin, N. A.; Ramesh, R. Advances in Magnetoelectric Multiferroics. *Nat. Mater.* **2019**, *18*, 203–212.

72) Sun, N. X.; Srinivasan, G. Voltage Control of Magnetism in Multiferroic Heterostructures and Devices. *SPIN* **2012**, *2*, 1240004.

73) Wang, Y.; Hu, J.; Lin, Y.; Nan, C. W. Multiferroic Magnetoelectric Composite Nanostructures. *NPG Asia Materials*. 2010.

74) Viehland, D.; Li, J. F.; Yang, Y.; Costanzo, T.; Yourdkhani, A.; Caruntu, G.; Zhou, P.; Zhang, T.; Li, T.; Gupta, A.; Popov, M.; Srinivasan, G. Tutorial: Product Properties in Multiferroic Nanocomposites. *J. Appl. Phys.* **2018**, *124*, 061101.

75) Zhou, J. P.; He, H. C.; Shi, Z.; Liu, G.; Nan, C. W. Dielectric, Magnetic, and Magnetoelectric Properties of Laminated $PbZr_{0.52}Ti_{0.48}O_3$-$CoFe_2O_4$ Composite Ceramics. *J. Appl. Phys.* **2006**, *100*, 0–6.

76) Chen, W.; Zhu, W.; Chen, X.; Wang, Z. Enhanced Ferroelectric and Dielectric Properties of $CoFe_2O_4$-$Pb(Zr_{0.53}Ti_{0.47})O_3$ Multiferroic Composite Thick Films. *J. Am. Ceram. Soc.* **2010**, *93*, 796–799.

77) Wan, J. G.; Wang, X. W.; Wu, Y. J.; Zeng, M.; Wang, Y.; Jiang, H.; Zhou, W. Q.; Wang, G. H.; Liu, J.-M. Magnetoelectric CoFe[Sub 2]O[Sub 4]–Pb(Zr,Ti)O[Sub 3] Composite Thin Films Derived by a Sol-Gel Process. *Appl. Phys. Lett.* **2005**, *86*, 122501.

78) Sim, C. H.; Pan, A. Z. Z.; Wang, J. Thickness and Coupling Effects in Bilayered Multiferroic $CoFe_2O_4$/$Pb(Zr_{0.52}Ti_{0.48})O_3$ Thin Films. *J. Appl. Phys.* **2008**, *103*, 124109.

79) Ding, L.-Y.; Wu, F.-X.; Chen, Y.-B.; Gu, Z.-B.; Zhang, S.-T. Controllable Microstructures and Multiferroic Properties of $Pb(Zr_{0.53}Ti_{0.47})O_3$–$CoFe_2O_4$ Composite Films. *Appl. Surf. Sci.* **2011**, *257*, 3840–3842.

80) Xie, S.; Ma, F.; Liu, Y.; Li, J. Multiferroic CoFe2O4-Pb(Zr(0.52)Ti(0.48))O3 Core-Shell Nanofibers and Their Magnetoelectric Coupling. *Nanoscale* **2011**, *3*, 3152–3158.

81) Tahmasebi, K.; Barzegar, A.; Ding, J.; Herng, T. S.; Huang, A.; Shannigrahi, S. Magnetoelectric Effect in $Pb(Zr_{0.95}Ti_{0.05})O_5$ and $CoFe_2O_4$ Heteroepitaxial Thin Film Composite. *Mater. Des.* **2011**, *32*, 2370–2373.

82) Tahmasebi, K.; Barzegar, A.; Ding, J.; Herng, T. S.; Huang, L.; Huang, A.; Shannigrahi, S. Multiferroic Thin Film Composite of $Pb(Zr_{0.95}Ti_{0.05})O_3$/$CoFe_2O_4$ on Si and $SrTiO_3$ Substrates. *Thin Solid Films* **2013**, *537*, 76–79.

83) Chien, D.; Buditama, A. N.; Schelhas, L. T.; Kang, H. Y.; Robbennolt, S.; Chang, J. P.; Tolbert, S. H. Tuning Magnetoelectric Coupling Using Porosity in Multiferroic Nanocomposites of ALD-Grown $Pb(Zr,Ti)O_3$ and Templated Mesoporous $CoFe_2O_4$. *Appl. Phys. Lett.* **2016**, *109*, 112904.

84) Zheng, H.; Wang, J.; Lofland, S. E.; Ma, Z.; Mohaddes-Ardabili, L.; Zhao, T.; Salamanca-Riba, L.; Shinde, S. R.; Ogale, S. B.; Bai, F.; Viehland, D.; Jia, Y.; Schlom, D. G.; Wuttig, M.; Roytburd, A.; Ramesh, R. Multiferroic BaTiO3-CoFe2O4 Nanostructures. *Science.* **2004**, *303*, 661–663.

85) Ortega, N.; Bhattacharya, P.; Katiyar, R. S.; Dutta, P.; Manivannan, A.; Seehra, M. S.; Takeuchi, I.; Majumder, S. B. Multiferroic Properties of Pb(Zr,Ti)O[Sub 3]/CoFe[Sub 2]O[Sub 4] Composite Thin Films. *J. Appl. Phys.* **2006**, *100*, 126105.

86) Aimon, N. M.; Choi, H. K.; Sun, X. Y.; Kim, D. H.; Ross, C. A. Templated Self-Assembly of Functional Oxide Nanocomposites. *Adv. Mater.* **2014**, *26*, 3063–3067.

87) Gao, X.; Zhang, D.; Wang, X.; Jian, J.; He, Z.; Dou, H.; Wang, H. Vertically Aligned Nanocomposite (BaTiO 3) 0.8 :(La 0.7 Sr 0.3 MnO 3) 0.2 Thin Films with Anisotropic Multifunctionalities. *Nanoscale Adv.* **2020**, *2*, 3276–3283.

88) Kim, D. H.; Ning, S.; Ross, C. A. Self-Assembled Multiferroic Perovskite–Spinel Nanocomposite Thin Films: Epitaxial Growth, Templating and Integration on Silicon. *J. Mater. Chem. C* **2019**, *7*, 9128–9148.

89) Sharma, Y.; Agarwal, R.; Collins, L.; Zheng, Q.; Ievlev, A. V.; Hermann, R. P.; Cooper, V. R.; Santosh, K. C.; Ivanov, I. N.; Katiyar, R. S.; Kalinin, S. V.; Lee, H. N.; Hong, S.; Ward, T. Z. Self-Assembled Room Temperature Multiferroic $BiFeO_3$-$LiFe5O_8$ Nanocomposites. *Adv. Funct. Mater.* **2020**, *30*, 1906849.

90) Raidongia, K.; Nag, A.; Sundaresan, A.; Rao, C. N. R. Multiferroic and Magnetoelectric Properties of Core-Shell $CoFe_2O_4$@$BaTiO_3$ Nanocomposites. *Appl. Phys. Lett.* **2010**, *97*, 062904.

91) Ojha, S.; Nunes, W. C.; Aimon, N. M.; Ross, C. A. Magnetostatic Interactions in Self-Assembled $Co_xNi_{1-x}Fe_2O_4$/$BiFeO_3$ Multiferroic Nanocomposites. *ACS Nano* **2016**, *10*, 7657–7664.

92) Murakami, M.; Chang, K. S.; Aronova, M. A.; Lin, C. L.; Yu, M. H.; Simpers, J. H.; Wuttig, M.; Takeuchi, I.; Gao, C.; Hu, B.; Lofland, S. E.; Knauss, L. A.; Bendersky, L. A. Tunable Multiferroic Properties in Nanocomposite $PbTiO_3$–$CoFe_2O_4$ Epitaxial Thin Films. *Appl. Phys. Lett.* **2005**, *87*, 112901.

93) Li, J.; Levin, I.; Slutsker, J.; Provenzano, V.; Schenck, P. K.; Ramesh, R.; Ouyang, J.; Roytburd, A. L. Self-Assembled Multiferroic Nanostructures in the $CoFe_2O_4$-$PbTiO_3$ System. *Appl. Phys. Lett.* **2005**, *87*, 072909.

94) Xiao, Z.; Lo Conte, R.; Goiriena-Goikoetxea, M.; Chopdekar, R. V.; Lambert, C. H. A.; Li, X.; N'Diaye, A. T.; Shafer, P.; Tiwari, S.; Barra, A.; Chavez, A.; Mohanchandra, K. P.; Carman, G. P.; Wang, K. L.; Salahuddin, S.; Arenholz, E.; Bokor, J.; Candler, R. N. Tunable Magnetoelastic Effects in Voltage-Controlled Exchange-Coupled Composite Multiferroic Microstructures. *ACS Appl. Mater. Interfaces* **2020**, *12*, 6752–6760.

95) Quickel, T. E.; Le, V. H.; Brezesinski, T.; Tolbert, S. H. On the Correlation between Nanoscale Structure and Magnetic Properties in Ordered Mesoporous Cobalt Ferrite ($CoFe_2O_4$) Thin Films. *Nano Lett.* **2010**, *10*, 2982–2988.

96) Quickel, T. E.; Schelhas, L. T.; Farrell, R. A.; Petkov, N.; Le, V. H.; Tolbert, S. H. Mesoporous Bismuth Ferrite with Amplified Magnetoelectric Coupling and Electric Field-Induced Ferrimagnetism. *Nat. Commun.* **2015**, *6*, 6562.

97)   Ortel, E.; Reier, T.; Strasser, P.; Kraehnert, R. Mesoporous IrO_2 Films Templated by PEO-PB-PEO Block-Copolymers: Self-Assembly, Crystallization Behavior, and Electrocatalytic Performance. *Chem. Mater.* **2011**, *23*, 3201–3209.

98)   Fang, J.; Kang, C. B.; Huang, Y.; Tolbert, S. H.; Pilon, L. Thermal Conductivity of Ordered Mesoporous Nanocrystalline Silicon Thin Films Made from Magnesium Reduction of Polymer-Templated Silica. *J. Phys. Chem. C* **2012**, *116*, 12926–12933.

99)   Rauda, I. E.; Buonsanti, R.; Saldarriaga-Lopez, L. C.; Benjauthrit, K.; Schelhas, L. T.; Stefik, M.; Augustyn, V.; Ko, J.; Dunn, B.; Wiesner, U.; Milliron, D. J.; Tolbert, S. H. General Method for the Synthesis of Hierarchical Nanocrystal-Based Mesoporous Materials. *ACS Nano* **2012**, *6*, 6386–6399.

100)   Hsueh, H.-Y.; Yao, C.-T.; Ho, R.-M. Well-Ordered Nanohybrids and Nanoporous Materials from Gyroid Block Copolymer Templates. *Chem. Soc. Rev.* **2015**, *44*, 1974–2018.

101)   Brinker, C. J.; Lu, Y.; Sellinger, A.; Fan, H. Evaporation-Induced Self-Assembly: Nanostructures Made Easy. *Adv. Mater.* **1999**, *11*, 579–585.

102)   Brezesinski, T.; Groenewolt, M.; Gibaud, A.; Pinna, N.; Antonietti, M.; Smarsly, B. Evaporation-Induced Self-Assembly (EISA) at Its Limit: Ultrathin, Crystalline Patterns by Templating of Micellar Monolayers. *Adv. Mater.* **2006**, *18*, 2260–2263.

103)   Yang, P. Hierarchically Ordered Oxides. *Science.* **1998**, *282*, 2244–2246.

104)   Fattakhova-Rohlfing, D.; Brezesinski, T.; Rathouský, J.; Feldhoff, A.; Oekermann, T.; Wark, M.; Smarsly, B. M. Transparent Conducting Films of Indium Tin Oxide with 3D Mesopore Architecture. *Adv. Mater.* **2006**, *18*, 2980–2983.

105)   Choi, J. H.; Zhang, F.; Perng, Y.-C.; Chang, J. P. Tailoring the Composition of Lead Zirconate Titanate by Atomic Layer Deposition. *J. Vac. Sci. Technol. B, Nanotechnol. Microelectron. Mater. Process. Meas. Phenom.* **2013**, *31*, 012207.

106)   Benedetto, J. M.; Moore, R. A.; McLean, F. B. Effects of Operating Conditions on the Fast-Decay Component of the Retained Polarization in Lead Zirconate Titanate Thin Films. *J. Appl. Phys.* **1994**, *75*, 460.

107)   Jenkins, I. G.; Song, T. K.; Madhukar, S.; Prakash, A. S.; Aggarwal, S.; Ramesh, R. Dynamics of Polarization Loss in (Pb, La)(Zr, Ti)O_3 Thin Film Capacitors. *Appl. Phys. Lett.* **1998**, *72*, 3300–3302.

108)   Dunn, S. Determination of Cross Sectional Variation of Ferroelectric Properties for Thin Film (Ca. 500 Nm) PZT (30/70) via PFM. *Integr. Ferroelectr.* **2003**, *59*, 1505–1512.

109) Choi, T.; Kim, J.-S.; Park, B. H.; Shin, H.; Lee, J. Ferroelectricity in Ultrathin PbZrO$_3$/PbTiO$_3$ Artificial Superlattices by Scanning Probe Microscopy. *Ferroelectrics* **2006**, *336*, 271–277.

110) Kirsch, B. L.; Chen, X.; Richman, E. K.; Gupta, V.; Tolbert, S. H. Probing the Effects of Nanoscale Architecture on the Mechanical Properties of Hexagonal Silica/Polymer Composite Thin Films. *Adv. Funct. Mater.* **2005**, *15*, 1319–1327.

111) Jaffe, H.; Berlincourt, D. A. Piezoelectric Transducer Materials. *Proc. IEEE* **1965**, *53*, 1372–1386.

112) Hooker, M. W. Properties of PZT-Based Piezoelectric Ceramics Between −150 and 250°C. **1998**, No. September.

113) Guo, R.; Cross, L. E.; Park, S.-E.; Noheda, B.; Cox, D. E.; Shirane, G. Origin of the High Piezoelectric Response in PbZr[1-x]Ti[x]O[3]. *Phys. Rev. Lett.* **2000**, *84*, 5423–5426.

114) Roy, K. Area-Delay-Energy Tradeoffs of Strain-Mediated Multiferroic Devices. *IEEE Trans. Magn.* **2015**, *51*, 2500808.

115) Van Den Boomgaard, J.; Van Run, A. M. J. G.; Van Suchtelen, J. Magnetoelectricity in Piezoelectric—Magnetostrictive Composites. *Ferroelectrics* **1976**, *10*, 295–298.

116) Aubert, A.; Loyau, V.; Mazaleyrat, F.; LoBue, M. Enhancement of the Magnetoelectric Effect in Multiferroic CoFe2O4/PZT Bilayer by Induced Uniaxial Magnetic Anisotropy. *IEEE Trans. Magn.* **2017**, *53*, 8109405.

117) Murugavel, P.; Padhan, P.; Prellier, W. Enhanced Magnetoresistance in Ferromagnetic Pr$_{0.85}$Ca$_{0.15}$MnO$_3$/ferroelectric Ba$_{0.6}$Sr$_{0.4}$TiO$_3$ Superlattice Films. *Appl. Phys. Lett.* **2004**, *85*, 4992.

118) Singh, M. P.; Prellier, W.; Mechin, L.; Simon, C.; Raveau, B. Correlation between Structure and Properties in Multiferroic La$_{0.7}$Ca$_{0.3}$MnO$_3$/BaTiO$_3$ Superlattices. *J. Appl. Phys.* **2006**, *99*, 024105.

119) Ma, Y. G.; Cheng, W. N.; Ning, M.; Ong, C. K. Magnetoelectric Effect in Epitaxial Pb(Zr0.52Ti0.48)O3/La0.7Sr0.3MnO3 Composite Thin Film. *Appl. Phys. Lett.* **2007**, *90*, 152911.

120) Khojah, R.; Xiao, Z.; Panduranga, M. K.; Bogumil, M.; Wang, Y.; Goiriena-Goikoetxea, M.; Chopdekar, R. V; Bokor, J.; Carman, G. P.; Candler, R. N.; Di Carlo, D.; Khojah, R.; Bogumil, M.; Wang, Y.; Di Carlo, D.; Xiao, Z.; Candler, R. N.; Panduranga, M. K.; Carman, G. P.; Goiriena-Goikoetxea, M.; Bokor, J.; Chopdekar, R. V. Single-Domain Multiferroic Array-Addressable Terfenol-D (SMArT) Micromagnets for Programmable Single-Cell Capture and Release. *Adv. Mater.* **2021**, *33*, 2006651.

121) Hsiao, Y. C.; Khojah, R.; Li, X.; Kundu, A.; Chen, C.; Gopman, D. B.; Chavez, A. C.; Lee, T.; Xiao, Z.; Sepulveda, A. E.; Candler, R. N.; Carman, G. P.; Di Carlo, D.; Lynch, C. S. Capturing Magnetic Bead-Based Arrays Using Perpendicular Magnetic Anisotropy. *Appl. Phys. Lett.* **2019**, *115*, 082402.

122) Chu, Z.; Pourhosseiniasl, M.; Dong, S. Review of Multi-Layered Magnetoelectric Composite Materials and Devices Applications. *J. Phys. D. Appl. Phys.* **2018**, *51*, 243001.

123) Levin, I.; Li, J.; Slutsker, J.; Roytburd, A. L. Design of Self-Assembled Multiferroic Nanostructures in Epitaxial Films. *Adv. Mater.* **2006**, *18*, 2044–2047.

124) Murakami, M.; Chang, K. S.; Aronova, M. A.; Lin, C. L.; Yu, M. H.; Simpers, J. H.; Wuttig, M.; Takeuchi, I.; Gao, C.; Hu, B.; Lofland, S. E.; Knauss, L. A.; Bendersky, L. A. Tunable Multiferroic Properties in Nanocomposite $PbTiO_3$–$CoFe_2O_4$ Epitaxial Thin Films. *Appl. Phys. Lett.* **2005**, *87*, 112901.

125) Chang, K. S.; Aronova, M. A.; Lin, C. L.; Murakami, M.; Yu, M. H.; Hattrick-Simpers, J.; Famodu, O. O.; Lee, S. Y.; Ramesh, R.; Wuttig, M.; Takeuchi, I.; Gao, C.; Bendersky, L. A. Exploration of Artificial Multiferroic Thin-Film Heterostructures Using Composition Spreads. *Appl. Phys. Lett.* **2004**, *84*, 3091.

126) Ryu, S.; Park, J. H.; Jang, H. M. Magnetoelectric Coupling of [00l]-Oriented $Pb(Zr_{0.4}Ti_{0.6})O3$–Ni0.8Zn0.2Fe2O4 Multilayered Thin Films. *Appl. Phys. Lett.* **2007**, *91*, 142910.

127) He, H. C.; Wang, J.; Zhou, J. P.; Nan, C. W. Ferroelectric and Ferromagnetic Behavior of $Pb(Zr_{0.52}Ti_{0.48})O_3$–$Co_{0.9}Zn_{0.1}Fe_2O_4$ Multilayered Thin Films Prepared via Solution Processing. *Adv. Funct. Mater.* **2007**, *17*, 1333–1338.

128) Ryu, H.; Murugavel, P.; Lee, J. H.; Chae, S. C.; Noh, T. W.; Oh, Y. S.; Kim, H. J.; Kim, K. H.; Jang, J. H.; Kim, M.; Bae, C.; Park, J. G. Magnetoelectric Effects of Nanoparticulate $Pb(Zr_{0.52}Ti_{0.48})O_3$–$NiFe_2O_4$ Composite Films. *Appl. Phys. Lett.* **2006**, *89*, 102907.

129) Mayeen, A.; Kala, M. S.; Jayalakshmy, M. S.; Thomas, S.; Philip, J.; Rouxel, D.; Bhowmik, R. N.; Kalarikkal, N. Flexible and Self-Standing Nickel Ferrite–PVDF-TrFE Cast Films: Promising Candidates for High-End Magnetoelectric Applications. *Dalt. Trans.* **2019**, *48*, 16961–16973.

130) Choi, M. H.; Yang, S. C. $CoFe_2O_4$ Nanofiller Effect on β-Phase Formation of PVDF Matrix for Polymer-Based Magnetoelectric Composites. *Mater. Lett.* **2018**, *223*, 73–77.

131) Luo, H.; Yang, H.; Baily, S. A.; Ugurlu, O.; Jain, M.; Hawley, M. E.; McCleskey, T. M.; Burrell, A. K.; Bauer, E.; Civale, L.; Holesinger, T. G.; Jia, Q. Self-Assembled Epitaxial Nanocomposite $BaTiO_3$-$NiFe_2O_4$ Films Prepared by Polymer-Assisted Deposition. *J. Am. Chem. Soc.* **2007**, *129*, 14132–14133.

132) Yan, L. H.; Liang, W. Z.; Liu, S. H.; Huang, W.; Lin, Y. Multiferroic $BaTiO_3$-$CoFe_2O_4$ Nano Composite Thin Films Grown by Polymer-Assisted Deposition. *Integr. Ferroelectr.* **2011**, *131*, 82–88.

133) Mori, K.; Kondo, Y.; Yamashita, H. Synthesis and Characterization of FePd Magnetic Nanoparticles Modified with Chiral BINAP Ligand as a Recoverable Catalyst Vehicle for the Asymmetric Coupling Reaction. *Phys. Chem. Chem. Phys.* **2009**, *11*, 8949–8954.

134) Corral-Flores, V.; Bueno-Baques, D.; Carrillo-Flores, D.; Matutes-Aquino, J. A. Enhanced Magnetoelectric Effect in Core-Shell Particulate Composites. *J. Appl. Phys.* **2006**, *99*, 08J503.

135) Lindemann, S.; Irwin, J.; Kim, G. Y.; Wang, B.; Eom, K.; Wang, J.; Hu, J.; Chen, L. Q.; Choi, S. Y.; Eom, C. B.; Rzchowski, M. S. Low-Voltage Magnetoelectric Coupling in Membrane Heterostructures. *Sci. Adv.* **2021**, *7*, 2294.

136) Zheng, H.; Kreisel, J.; Chu, Y. H.; Ramesh, R.; Salamanca-Riba, L. Heteroepitaxially Enhanced Magnetic Anisotropy in $BaTiO_3$–$CoFe_2O_4$ Nanostructures. *Appl. Phys. Lett.* **2007**, *90*, 113113.

137) Gao, X.; Li, L.; Jian, J.; Wang, H.; Fan, M.; Huang, J.; Wang, X.; Wang, H. Vertically Aligned Nanocomposite $BaTiO_3$:$YMnO_3$ Thin Films with Room Temperature Multiferroic Properties toward Nanoscale Memory Devices. *ACS Appl. Nano Mater.* **2018**, *1*, 2509–2514.

138) Deng, C.; Zhang, Y.; Ma, J.; Lin, Y.; Nan, C. W. Magnetoelectric Effect in Multiferroic Heteroepitaxial $BaTiO_3$–$NiFe_2O_4$ Composite Thin Films. *Acta Mater.* **2008**, *56*, 405–412.

139) Zhang, S. T.; Zhang, Y.; Luo, Z. L.; Lu, M. H.; Gu, Z. Bin; Chen, Y. F. Multiferroic Properties of $Bi_{0.8}La_{0.2}FeO_3$/$CoFe_2O_4$ Multilayer Thin Films. *Appl. Surf. Sci.* **2009**, *255*, 5092–5095.

140) Brezesinski, T.; Wang, J.; Senter, R.; Brezesinski, K.; Dunn, B.; Tolbert, S. H. On the Correlation between Mechanical Flexibility, Nanoscale Structure, and Charge Storage in Periodic Mesoporous CeO2 Thin Films. *ACS Nano* **2010**, *4*, 967–977.

141) Sree, S. P.; Dendooven, J.; Smeets, D.; Deduytsche, D.; Aerts, A.; Vanstreels, K.; Baklanov, M. R.; Seo, J. W.; Temst, K.; Vantomme, A.; Detavernier, C.; Martens, J. A. Spacious and Mechanically Flexible Mesoporous Silica Thin Film Composed of an Open Network of Interlinked Nanoslabs. *J. Mater. Chem.* **2011**, *21*, 7692–7699.

142) Seth, S.; Jhulki, S. Porous Flexible Frameworks: Origins of Flexibility and Applications. *Mater. Horizons* **2021**, *8*, 700–727.

143) Huang, S.; Karaba, C. T.; Patel, S. K.; Neal, A.; Tolbert, S. H.; Marian, J. Simulating the Non-Monotonic Strain Response of Nanoporous Multiferroic Composites under Electric Field Control. *Appl. Phys. Lett.* **2022**, *120*, 213501.

144) Buditama, A. N.; Fitzell, K.; Chien, D.; Karaba, C. T.; Patel, S. K.; Kang, H. Y.; Chang, J. P.; Tolbert, S. H. Strain Transfer in Porous Multiferroic Composites of $CoFe_2O_4$ and $PbZr_xTi_{1-x}O_3$. *Appl. Phys. Lett.* **2022**, *120*, 192902.

145) Liang, X.; Dong, C.; Chen, H.; Wang, J.; Wei, Y.; Zaeimbashi, M.; He, Y.; Matyushov, A.; Sun, C.; Sun, N. A Review of Thin-Film Magnetoelastic Materials for Magnetoelectric Applications. *Sensors* **2020**, *20*, 1532.

146) Yang, P.; Zhao, D.; Margolese, D. I.; Chmelka, B. F.; Stucky, G. D. Block Copolymer Templating Syntheses of Mesoporous Metal Oxides with Large Ordering Lengths and Semicrystalline Framework. *Chem. Mater.* **1999**, *11*, 2813–2826.

147) Galo, G. J.; Crepaldi, E. L.; Grosso, D.; Sanchez, C. Block Copolymer-Templated Mesoporous Oxides. *Curr. Opin. Colloid Interface Sci.* **2003**, *8*, 109–126.

148) Kim, D. M.; Eom, C. B.; Nagarajan, V.; Ouyang, J.; Ramesh, R.; Vaithyanathan, V.; Schlom, D. G. Thickness Dependence of Structural and Piezoelectric Properties of Epitaxial $Pb(Zr_{0.52}Ti_{0.48})O_3$ Films on Si and $SrTiO_3$ Substrates. *Appl. Phys. Lett.* **2006**, *88*, 142904.

149) Araújo, E. B.; Lima, E. C.; Bdikin, I. K.; Kholkin, A. L. Thickness Dependence of Structure and Piezoelectric Properties at Nanoscale of Polycrystalline Lead Zirconate Titanate Thin Films. *J. Appl. Phys.* **2013**, *113*, 187206.

150) Daniel Chen, H.; Udayakumar, K. R.; Kewen, K. L. I.; Gaskey, C. J.; Eric Cross, L. Dielectric Breakdown Strength in Sol-Gel Derived PZT Thick Films. *Integr. Ferroelectr.* **2006**, *15*, 89–98.

151) Kim, Y.; Pham, C.; Chang, J. P. Potentials and Challenges of Integration for Complex Metal Oxides in CMOS Devices and Beyond. *J. Phys. D. Appl. Phys.* **2015**, *48*, 063001.

152) Pham, C. D.; Chang, J.; Zurbuchen, M. A.; Chang, J. P. Synthesis and Characterization of $BiFeO_3$ Thin Films for Multiferroic Applications by Radical Enhanced Atomic Layer Deposition. *Chem. Mater.* **2015**, *27*, 7282–7288.

153) Chien, D.; Buditama, A. N.; Schelhas, L. T.; Kang, H. Y.; Robbennolt, S.; Chang, J. P.; Tolbert, S. H. Tuning Magnetoelectric Coupling Using Porosity in Multiferroic Nanocomposites of ALD-Grown Pb(Zr,Ti)O3 and Templated Mesoporous CoFe2O4. *Appl. Phys. Lett.* **2016**, *109*, 112904.

154) Baklanov, M. R.; Mogilnikov, K. P.; Polovinkin, V. G.; Dultsev, F. N. Determination of Pore Size Distribution in Thin Films by Ellipsometric Porosimetry. *J. Vac. Sci. Technol. B Microelectron. Nanom. Struct. Process. Meas. Phenom.* **2000**, *18*, 1385.

155) S. J. Gregg; K. S. W. Sing. *Adsorption, Surface Area, and Porosity*, 2nd ed.; R. Haul, Ed.; Academic Press: London, New York, 1982; Vol. 86.

156) Suzuki, Y.; Van Dover, R. B.; Gyorgy, E. M.; Phillips, J. M.; Korenivski, V.; Werder, D. J.; Chen, C. H.; Felder, R. J.; Cava, R. J.; Krajewski, J. J.; Peck, W. F. Magnetic Properties of Epitaxial Ferrite Multilayer Films. *J. Appl. Phys.* **1998**, *79*, 5923.

157) Wang, Y. G.; Zhong, W. L.; Zhang, P. L. Size Effects on the Curie Temperature of Ferroelectric Particles. *Solid State Commun.* **1994**, *92*, 519–523.

158) Zhong, W. L.; Wang, Y. G.; Zhang, P. L. Size Effects on Phase Transitions in Ferroelectric Films. *Phys. Lett. A* **1994**, *189*, 121–126.

159) Wang, C. L.; Smith, S. R. P. Landau Theory of the Size-Driven Phase Transition in Ferroelectrics. *J. Phys. Condens. Matter* **1995**, *7*, 7163.

160) Alrub, A. M.; Ong, L. H. Thickness Dependence of Switching Time and Coercive Field in Ferroelectric Thin Films. *J. Appl. Phys.* **2011**, *109*, 084109.

161) Ishibashi, Y.; Orihara, H.; Tilley, D. R. Thickness Transitions of Ferroelectricity in Thin Films. *J. Phys. Soc. Japan* **2013**, *67*, 3292–3297.

162) Robbennolt, S.; Menéndez, E.; Quintana, A.; Gómez, A.; Auffret, S.; Baltz, V.; Pellicer, E.; Sort, J. Reversible, Electric-Field Induced Magneto-Ionic Control of Magnetism in Mesoporous Cobalt Ferrite Thin Films. *Sci. Rep.* **2019**, *9*, 1–14.

163) Robbennolt, S.; Yu, P.; Nicolenco, A.; Mercier Fernandez, P.; Coll, M.; Sort, J. Magneto-Ionic Control of Magnetism in Two-Oxide Nanocomposite Thin Films Comprising Mesoporous Cobalt Ferrite Conformally Nanocoated with HfO_2. *Nanoscale* **2020**, *12*, 5987–5994.

164) Nichterwitz, M.; Honnali, S.; Kutuzau, M.; Guo, S.; Zehner, J.; Nielsch, K.; Leistner, K. Advances in Magneto-Ionic Materials and Perspectives for Their Application. *APL Mater.* **2021**, *9*, 030903.

165) Bauer, U.; Yao, L.; Tan, A. J.; Agrawal, P.; Emori, S.; Tuller, H. L.; Van Dijken, S.; Beach, G. S. D. Magneto-Ionic Control of Interfacial Magnetism. *Nat. Mater.* **2015**, *14*, 174–181.

166) Tang, X.; Viswan, R.; Gao, M.; Leung, C. M.; Folger, C.; Luo, H.; Howe, B.; Li, J.; Viehland, D. Nanopillars with E-Field Accessible Multi-State ($N \geq 4$) Magnetization Having Giant Magnetization Changes in Self-Assembled $BiFeO_3$-$CoFe_2O_4$/$Pb(Mg_{1/3}Nb_{2/3})$-38at%$PbTiO_3$ Heterostructures. *Sci. Rep.* **2018**, *8*, 1–7.

167) Zavaliche, F.; Zheng, H.; Mohaddes-Ardabili, L.; Yang, S. Y.; Zhan, Q.; Shafer, P.; Reilly, E.; Chopdekar, R.; Jia, Y.; Wright, P.; Schlom, D. G.; Suzuki, Y.; Ramesh, R. Electric Field-Induced Magnetization Switching in Epitaxial Columnar Nanostructures. *Nano Lett.* **2005**, *5*, 1793–1796.

168) Tang, X.; Gao, M.; Leung, C. M.; Luo, H.; Li, J.; Viehland, D. Non-Volatility Using Materials with Only Volatile Properties: Vertically Integrated Magnetoelectric

Heterostructures and Their Potential for Multi-Level-Cell Devices. *Appl. Phys. Lett.* **2019**, *114*, 242903.

169) Xue, F.; Sato, N.; Bi, C.; Hu, J.; He, J.; Wang, S. X. Large Voltage Control of Magnetic Anisotropy in CoFeB/MgO/OX Structures at Room Temperature. *APL Mater.* **2019**, *7*, 101112.

170) Zhao, J. L.; Lu, H. X.; Sun, J. R.; Shen, B. G. Thickness Dependence of Piezoelectric Property of Ultrathin BiFeO$_3$ Films. *Phys. B Condens. Matter* **2012**, *407*, 2258–2261.